Novel Ion Traps for Enhanced Fluorescence Collections and Single Photon Sources Based on Barium Ions

Gang Shu

A dissertation submitted in partial fulfillment of
the requirements for the degree of

Doctor of Philosophy

University of Washington

2010

Program Authorized to Offer Degree: Physics

University of Washington
Graduate School

This is to certify that I have examined this copy of a doctoral dissertation by

Gang Shu

and have found that it is complete and satisfactory in all respects,
and that any and all revisions required by the final
examining committee have been made.

Chair of the Supervisory Committee:

Boris B Blinov

Reading Committee:

Boris B Blinov

David Bacon

David Cobden

Date:

Signature________________________________

Date____________________________________

University of Washington

Abstract

Novel Ion Traps for Enhanced Fluorescence Collections and Single Photon Sources Based on Barium Ions

Gang Shu

Chair of the Supervisory Committee:
Professor Boris B Blinov
Department of Physics

Efficient ion-photon interface is critical for ion-photon and ion-ion entanglement generation, which are the fundamental building blocks for loophole-free Bell inequality violation tests based on ion qubits, and for the quantum computer architecture based on ion-photon networks. As one approach to address the problem, the feasibility of integrating reflective optics into ion trap to increase free-space photon interception is studied. The development and operation of two novel ion traps are demonstrated: one integrates a spherical mirror with a linear quadrapole trap, and the other combines the optical surface with the RF electrode. The possibility of using aspherical optics to improve ion images is studied and partially implemented. A continuously excited single photon source based on $^{138}Ba^{+}$ ion is demonstrated and calibrated. Methods of scaling up current design are also discussed.

TABLE OF CONTENTS

LIST OF FIGURES

Figure Number Page

ABBREVIATIONS

AOM: Acoustic Optical Modulator

DAC: Digital to Analog Converter

DRIE: Deep reactive-ion etching

ECDL: External Cavity Diode Laser

EMCCD: Electron Multiplication Charge Coupled Device

EOM: Electric Optical Modulator

MEMS: Microelectromechanical Systems

NA: Numerical Aperture

PID: Proportional, Integral and Differential

PMT: Photon Multiplication Tube

R.M.S.: Root Mean Square

RF: Radio Frequency

RIE: Reactive ion etching

UHV: Ultra High Vacuum

UV: Ultraviolet

ACKNOWLEDGMENTS

I would like to thank my mother for her 29 years' nurture of me, especially those hard years after my father's passing away in 1989. She backs me up for every step to my current accomplishment. I am indebted to my wife, whose great sacrifice to the family enables me to concentrate on the work.

All this would not have been possible without my advisor Boris Blinov. To me, he is a learned teacher, a kind friend and an energetic colleague. It is him who guided me into the world of atomic experiments and through various difficulties in my research and life. The past five years with Boris is the most pleasant and inspiring time in my life.

Those days in the basement would be unbearable if Nathan Kurz, Matthew Dietrich and Adam Kleczewski were not around. Their help and collaboration is indispensible for all my projects. I'll miss Nathan's brew, Matt's bread and their unsuccessful effort to educate me into a beer person.

I am grateful to work with Nathan Pegram, Edan Shahar, Sanghoon (Hoony) Chong, Viki Mirgon, Joseph Pirtle, Ryan Bowler, Peter Greene, Frank Garcia, Tom Noel, Eric Magnuson, Aaron Avril, Chris Dostert, Anya Davis and Corey Adams. I would specially thank Ronald Musgrave and Bryan Venema for their expert in machining and electronics.

I owe my gratitude to my reading committee: Boris, Dave Bacon and David Cobden. I feel guilty to "force" them to read my writing full of typos. Thank you all for the corrections and comments!

Lastly, I offer my regards to all of those who supported me in any respect during the completion of my graduate study and thesis.

DEDICATION

To my mother Xiaowen and wife Yan

Chapter 1

BACKGROUND AND MOTIVATIONS

1.1 Introduction to Quantum Computation

Quantum computation is a relatively young field with a history of less than 30 years since it was first mentioned by Richard Feynman[1]. The Deutch's Algorithm[2, 3] was probably the first algorithm to illustrate its unique power of parallelism. Both theoretical and experimental activities surged after the discovery of the Shor algorithm[4], which factorizes big numbers at speeds exponentially faster than the best known classical algorithms. Although it is unclear whether efficient classical imitations of these quantum algorithms are possible, it is believed that quantum mechanic's unique properties of superposition and entanglement should bring additional computational power over classical physics: it is still not known whether this power will be strong enough to conquer the NP-complete problems[5].

In a typical computer, information is represented and processed in binary form because it is the simplest nontrival system. A corresponding two level physical system has to be found as a physical representation. Processing of the information should be fast, efficient and fault-tolerant, as is possible in conventional semiconductor electronics. Other systems such as light pulses and molecules can also be employed at higher expense and complexity, but all of them share the same operational principle based on classical physics. At a time that is more than 100 years after the revolutionary discovery of quantum mechanics, it is hard to believe that people still dwell on classical physics for computation. Maybe there is too much room above the bottom[6] for Moore's Law to be valid for decades before we are forced to look into quantum computation. Fortunately, as quantum mechanics can explain all classical physics, a quantum computer can efficiently solve all problems current computers are good at. But just as the adjustment from classical physics to quantum mechanics can be counter-intuitive, so may be the shift to quantum computation.

Quantum computation is based on the qubit, the quantum counterpart of a classical bit.

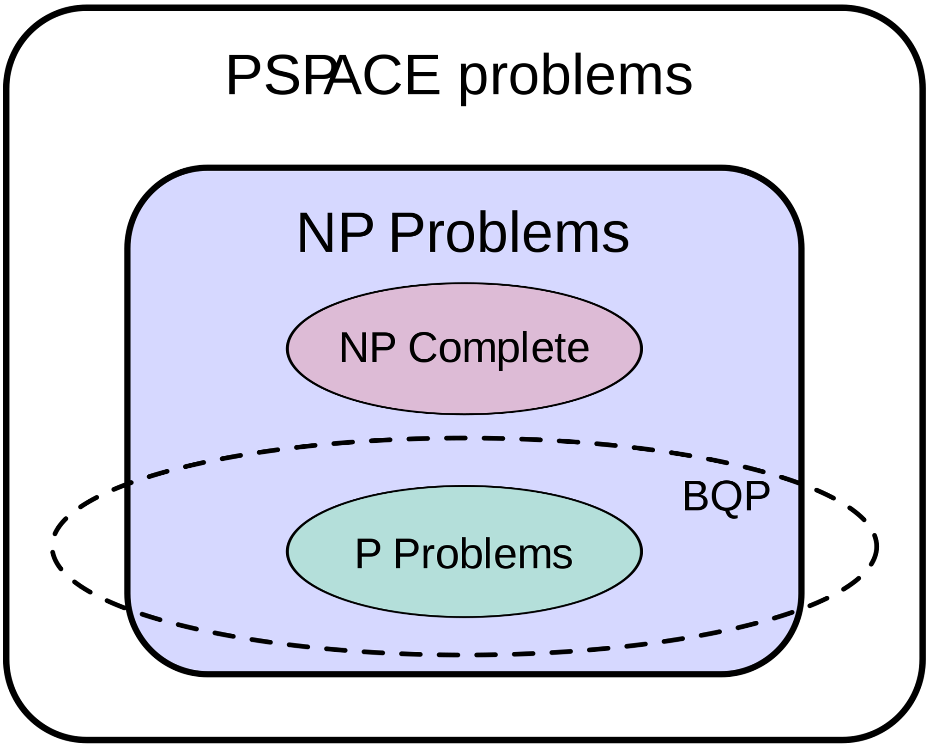

Figure 1.1: The possible realm of quantum computation power. PSPACE: problems can be solved with limited resources. NP: problems with solutions can be efficiently verified. P: problems can be solved by classical computers in polynomial time. BQP: problems can be solved by quantum computer in polynomial time. NP complete: an equivalent problem set believed to have super-polynomial complexity. Note that ”to solve” here has different meanings. For P, NP and PSPACE, it means to get a correct answer with certainty, while for BQP, it means to get a correct answer with high probability [7].

The most significant differences between a qubit and a classical bit are the measurement and superposition. Quantum systems do not have a definite state until the measurement happens, which collapses the quantum system into one of the measurement operator's eigenstates with the eigenvalue as the result. In the simplest example of superposition, both 1 and 0 can be coherently encoded into a single qubit at the same time. Quantum operations handle the qubits in a coherent way so that each component follows its own evolution. This brings in the intrinsic parallelism of quantum computation and there is no counterpart in the classical physics.

More than 15 years have passed since the first efficient quantum algorithm was discovered [4], but except for a handful of new practical algorithms[2, 8], there are few breakthroughs. This may be easy to understand because human beings are classical animals and it is simply anti-intuitive for classical brains to think quantum mechanically. This gap may be much bigger than that between a human brain and a classical Turning machine. The highly developed classical computation technology implies that it may not be necessary to transfer our simple daily calculations that are already very efficiently implemented on a PC to a quantum computer, just as there is no need to use quantum physics to replace all the classical physics in the everyday life. A quantum computer may eventually appear as a special device to crack some of the most difficult problems. On the other hand, as people dive deeper into the quantum world, the classical computers quickly become useless for simulations. Using well controlled quantum system (such as a quantum computer) to simulate other, unknown quantum systems may prove extremely useful[9, 10].

From the practical perspective, building a quantum computer requires a few "simple" steps, known as the Divincenzo criteria[11]: First, a good qubit carrier is needed. Any two level quantum system that can be efficiently controlled, measured and scaled up is a good qubit candidate. They include superconductor Josephson junctions[12], trapped ions/atoms[13, 14, 15], quantum dots[16], nuclear magnetic resonance[17] and photons[18]. Second, a universal gate set is necessary. One of the simplest sets consists a two-qubit CNOT gate and single qubit rotations and it has already been realized in several qubit systems[19, 20, 21, 22]. Lastly, a reliable scheme to scale up and build realistic computing device is necessary. Optimists expect to see practical quantum computer with a decade.

1.2 Quantum Computation Architectures with Trapped Ions

Trapped ion system is believed to be the most promising one among the qubit candidates, because it fulfills all the DiVincenzo implementation requirements and all the fundamental building blocks of a quantum computer have already been realized in this system.

A single atom or an atomic ion is a very simple quantum system. Trapped ions are well isolated from the environment, so they enjoy long coherence times[23] as compared to many other quantum system. Two of the ion's electron states are chosen as the qubit levels. According to the transition's energy range, qubits can be divided into optical, whose energy splitting is at an optical frequency, and hyperfine, whose transition is in the RF range. Ion qubits are either alkline earth metal or similar elements because after single ionization, they have a simple hydrogen-like electron structure with a closed shell plus one free electron. The following table lists the common transitions of several ion species that may be suitable for qubits.

Element	$S_{1/2}$-$P_{1/2,3/2}$ (nm)	$P_{1/2,3/2}$-$D_{3/2,5/2}$ (nm)	$S_{1/2}$-$D_{3/2,5/3}$ (nm)	Other
$^{9}Be^{+}$	313/313			
$^{24/25}Mg^{+}$	279/280			
$^{40/43}Ca^{+}$	393/397	854/850/866	729/732	
$^{88/87}Sr^{+}$	408/422	1033/1004	674/687	
$^{137/138}Ba^{+}$	455/495	614/585.5/650	1762/2052	
Zn^{+}	202.6/206			
$^{110/111/113}Cd^{+}$	214.5/226.5			
Hg^{+}	164/194			
$^{171/173}Yb^{+}$	369.5		435.5	935.2

The basic qubit operations include state initialization and detection, single qubit rotations, and two qubit gates. The initialization of ion qubits is normally done with optical pumping, which can be accomplished with very high fidelity[24]. Here the selectivity afforded by the light's polarization or frequency direct the electron population to one specific level. Detection can be done by selectively shelving one of the qubit states out of the fluorescence cycle and observing the ”quantum jump” [25]. Single qubit rotations can be realized by either optical or RF Rabi flop or the stimulated Raman transition. The two-qubit gates[26, 27, 20] can be implemented with the help of the Coulomb interaction of the ions, through the normal modes of the trap oscillation.

The coherence time of the ion qubit is typically between hundreds of ms and many seconds [23], during which thousands of gate operations can be carried out. Ion qubits already integrate the best flying qubit, photons, into their optical transitions, thus they enjoy a very fast quantum channel for remote communication.

Currently, the setup for even a single ion qubit is much larger than the vacuum tubes used in early computers or the first transistor, and it is hopeless to imagine adding hundreds of such setups up to a working system. There are multiple proposals to realize an ion trap quantum computer. The earliest, by Cirac and Zoller, is based on ions confined in a single linear trap[26]. But practically, as the number of ions increases, motional modes become denser than laser resolution. It is also difficult to keep so many ions in a straight line. A more recent proposal by Kielpihski, Monroe and Wineland [28], is called the ”Quantum CCD”, where multiple ions are trapped in different zones of a multiplexed trap and shuttled around by biasing the DC electrode array. Quantum information is encoded in ions’ internal energy levels which are well isolated from their motion. Qubit operations are done by moving the specific ions to the interaction zone, where lasers can either change ion’s internal states to carry out single qubit rotations or couple ions’ internal states with their oscillation modes for multi-qubit gates. This scheme requires accurate control over large numbers of electrodes. Current state-of-the-art technology can achieve ion shuttling with a success rate of 99.9999%(with surface traps developed by Sandia National Lab). After shuttling, the ions need to be cooled down, and this can be done by shaping the shuttling electric field or by sympathetic cooling with other ion species[29, 30].

We can estimate the potential computational speed of this scheme. Suppose both the single qubit rotations and the two qubit gate can be done in 10^{-6} s; the shuttling speed is $\sim 1\ m/s$. The distance between the interaction zone and storage zone is of order of 1 mm. We also assume that the initialization and the readout are done offline, and that each operation consists of moving two qubit together, performing two single qubit rotations and one two-qubit gate operation. If there are n qubits in the storage zone, to move any two of them together require $O(n)$ shuttlings. So the unit operation time is $O(n) \times 10^{-3}\ s$. Ions can be divided into small clusters to keep the shuttling time for local operations small, but shuttling between clusters may need additional time to cover a longer distance.

Another scheme for scaling up quantum computer is based on ion-photon networks[31, 32, 33, 34, 35, 21]. Instead of shuttling massive particles around at a slow speed, photons, the flying qubits, build the quantum channel for two remote ions. The ion-photon interface is probabilistic, so each operation has to be carried out more than once before it is definitely completed. Compared with the QCCD scheme, this scheme eliminates the need for mechanically moving ions at the price of a (much) smaller than unity success rate. By dividing qubits into small groups connected with photons, a combination of the two schemes can take advantage of former's high fidelity and the latter's near independence of distance. In my thesis, I will mainly discuss our effort to develop novel ion traps for efficient ion-photon interface.

1.3 Ion Photon Entanglement and Ion-Ion Entanglement

Another unique feature of quantum mechanics is entanglement. It is built on the foundation of quantum superposition and shows a profound difference between classical and quantum physics. It appears to violate the local realism which scientists have believed to be essential for a long time [38]. Entangled states are states that can not be decomposed into a product of single qubit states. For two qubits, there are four maximally entangled states (Bell states):

$$|\beta_{00}> = \frac{|00> + |11>}{\sqrt{2}} \tag{1.1}$$

$$|\beta_{01}> = \frac{|01> + |10>}{\sqrt{2}} \tag{1.2}$$

$$|\beta_{10}> = \frac{|00> - |11>}{\sqrt{2}} \tag{1.3}$$

$$|\beta_{11}> = \frac{|01> - |10>}{\sqrt{2}} \tag{1.4}$$

There first three are symmetric and the last is asymmetric under exchange. They form a complete basis set for two qubit states.

Entanglement can arise from a combination of superposition and conservation laws. Physics laws such as momentum conservation, angular momentum conservation, energy conservation and particle number conservation set a restriction on undetermined state parameters, thus resulting in entanglement. The conservation laws arise from the symmetry as multiple qubits locally interacting with each other. Even if they are separated afterwards, the relation still holds. This spatial independence of entanglement can be utilized for tasks such as superdense coding[36] and teleportation[37].

The clearest example of entanglement's non-classical nature is the violation of Bell inequality by entangled systems. The Bell inequality describes the following situation: two physical systems are distributed to two places, A and B, for measurements. At each location, two different measurements (M_{a_1}, M_{a_2} and M_{b_1}, M_{b_2}), both with results of ±1, are carried out randomly. Consider the average of following expression:

$$x = M_{a_1}(M_{b_1} + M_{b_2}) + M_{a_2}(M_{b_1} - M_{b_2}) \tag{1.5}$$

One of the $(M_{b_1} \pm M_{b_2})$ terms will be zero, thus $|x| = 2$. When averaged over a random sample of different kinds of the measurements, $| < M_{a_1}(M_{b_1} + M_{b_2}) + M_{a_2}(M_{b_1} - M_{b_2}) > | \leq 2$. The hidden assumption here is that all the measurements are local, so that one measurement will not affect the other. The measurements are "real", which means the values of M_{a_i}, M_{b_i} are set in prior to the measurements and are not changed by measurements [38]. But quantum mechanics says the opposite, before measurement the result is undecided and if the A and B are entangled, the two states can affect each other. For example, prepare the two qubits in one of the entangled states $|\beta_{00}>$. Choose the measurements to be $\sigma_{Z_1}, \sigma_{X_1}$ and $(-\sigma_{Z_2} - \sigma_{X_2})/\sqrt{2}, (\sigma_{Z_2} - \sigma_{X_2})/\sqrt{2}\}$. Repeating the calculation for quantum states, we have

$$< M_{a_1}(M_{b_1} + M_{b_2}) + Ma_2(M_{b_1} - M_{b_2}) >= 4 \times \frac{1}{\sqrt{2}} = 2\sqrt{2} > 2 \tag{1.6}$$

The entangled state violates the Bell inequality! Therefore quantum mechanics is not local realistic. A violation of the Bell inequality is often used as a proof of entanglement.

The two qubits can be of different species, for instance, one is an atom (or ion) and the other is a photon. The entanglement can be generated via a spontaneous decay from an excited state of the atom or ion that can proceed via multiple channels[39]. If there are two equal probability channels, corresponding to red and blue photons, then the photon energy(color) is entangled with the ion qubit states, so $|\phi>=\frac{1}{\sqrt{2}}(|1,r>+|0,b>)$, where the numbers 1,0 represent the ion qubit state and b and r represent photon color. If we have two identical ions and they are excited at the same time, two identical entangled states are generated. The overall state of four qubits (two ions and two photons) can be expanded and rewritten in the photons' Bell basis:

$$\begin{aligned}
|\Phi> &= \frac{1}{2}(|1_1,r_1>+|0_1,b_1>)(|1_2,r_2>+|0_2,b_2>)\\
&= \frac{1}{2}(|1_1,1_2,r_1,r_2>+|0_1,1_2,b_1,r_2>+|1_1,0_2,r_1,b_2>+|0_1,0_2,b_1,b_2>)\\
&= \frac{1}{2\sqrt{2}}((|1_1 1_2>+|0_1 0_2>)|\beta_{00}>+(|1_1 1_2>-|0_1 0_2>)|\beta_{10}>+\\
&\quad (|0_1 1_2>+|1_1 0_2>)|\beta_{01}>+(|1_1 0_2>-|0_1 1_2>)|\beta_{11}>)
\end{aligned}$$

If we can project the photons into one of the Bell states, the two ions will be entangled to the corresponding Bell state. This mathematical manipulation has significant physical meaning: Ions that never meet each other can be entangled via photons! The photon correlation measurement can be done with a beam splitter and two detectors. The function of a beam splitter can be seen as a rotation in the photon number space[40]:

$$|n>_a|m>_b \rightarrow e^{-i\theta\overline{J}_y}|n>_a|m>_b \tag{1.7}$$

where m,n is the numbers of identical photons entering each port and $\overline{J}_y=-i(a^+b-ab^+)/2$, with a and b the annihilation operators and a^+,b^+ the creation operators for the two modes entering the two ports; θ is $\pi\cdot R$, the reflectivity. For 1 photon, the rotation is:

$$\begin{pmatrix} |0>_a|1>_b \\ |1>_a|0>_b \end{pmatrix} = \begin{pmatrix} \cos R\pi/2 & \sin R\pi/2 \\ -\sin R\pi/2 & \cos R\pi/2 \end{pmatrix} \begin{pmatrix} |0>_a|1>_b \\ |1>_a|0>_b \end{pmatrix} \tag{1.8}$$

For 2 photons, the rotation is:

$$\begin{pmatrix} |0>_a|2>_b \\ |1>_a|1>_b \\ |2>_a|0>_b \end{pmatrix} = \begin{pmatrix} 1/2(1+\cos R\pi) & 1/\sqrt{2}\sin R\pi & 1/2(1-\cos R\pi) \\ -1/\sqrt{2}\sin R\pi & \cos R\pi & 1/\sqrt{2}\sin R\pi \\ 1/2(1-\cos R\pi) & -1/\sqrt{2}\sin R\pi & 1/2(1+\cos R\pi) \end{pmatrix} \begin{pmatrix} |0>_a|2>_b \\ |1>_a|1>_b \\ |2>_a|0>_b \end{pmatrix} \tag{1.9}$$

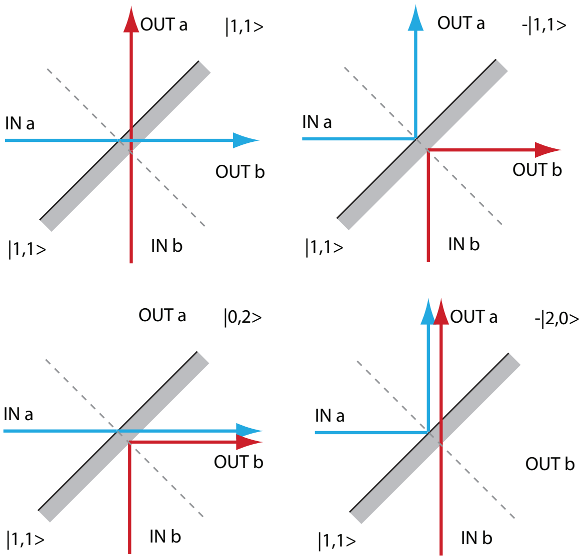

Figure 1.2: Different input and output modes for a beam splitter with two identical photons.

For the simple situation of 50/50 beam splitter (Fig. 1.2) , if there are two identical photons entering into port a and b at the same time, they will exit from the same port. Of the four Bell states, both $|\beta_{00}>$ and $|\beta_{10}>$ have two identical photons entering the two ports, so only one detector will register photons. The situation for $|\beta_{01}>$ and $|\beta_{11}>$ is a little complicated and to see that clearly, the state after the beam splitter can be written as:

$$\begin{aligned}|\beta_{01/11}> \quad &\rightarrow \quad \frac{1}{2\sqrt{2}}((|0>_a+|0>_b)(|1>_a-|1>_b)\pm(|1>_a+|1>_b)(|0>_a-|0>_b))\\ &= \quad \frac{1}{2\sqrt{2}}(|01>_a\pm|10>_a-|01>_b\pm|10>_b\\ &\quad\;\; -|0>_a|1>_b+|0>_b|1>_a\pm(|1>_b|0>_a-|1>_a|0>_b))\end{aligned}$$

The first four terms represent two photons emerging from the same port. These single port events correspond to ion states that can not be distinguished from each other, so the ion pair is in a mixed states that may not be entangled. The last four terms are critical. For β_{01}, they cancel each other, so there are no other events. For β_{11}, there are dual ports events $|0>_a|1>_b-|1>_a|0>_b$, which project the state to the antisymmetric entangled state. Ideally, the entanglement generation probability is 12.5%. But practically there are many factors that significantly reduce the efficiency. The ions can be excited at almost 100% with ultra fast pulses, but when they decay, they may have more paths than two. Photons due to these unwanted decay branches can be filtered out at the price of lower single photon generation efficiency. Collection efficiency of the radiated photons can be really low, about a percent for the current experiment. Coupling the photons into an optical fiber may lose another 80%. Additional optics like beam splitters, filters, lenses and so on may lose even more. Finally, the detectors' quantum efficiency (typically photon multiplier tubes, PMT) is only $\sim 10\% - 20\%$, far from perfect. There are two sets of ion-photon pairs, so every loss small term is squared. This may result in a really inefficient generation of the ion-ion entanglement. The current state-of-the-art experiment can generate one entanglement in about 10 minutes with the experiment running at a rate of tens of kHz[41]. There is plenty of room for improvement, for example, by using high quantum efficiency single-photon detectors. The fluorescence collection can also be greatly improved with better optics and specially developed ion traps. This is one of the motivations of my thesis: develop a trap that can easily implement an efficient fluorescence collection scheme, so that ion-photon entanglement and photon-connected ion network become practical.

1.4 Loophole-free Bell Inequality Violation

The other goal of our future experiments is a loophole-free Bell inequality test. Although a number of recent Bell inequality violation experiments rebut the various hidden variable theories, there are "loopholes" of information exchange and selective sampling[42]. The first of these refers to two measurements that are not far enough apart in space, and may be connected via unknown channels. This can be clearly seen in Fig. 1.3: Suppose A and B possess two entangled qubits. They should independently rotate and measure their own qubits, which means that one's qubit rotation (time t_r) and measurement (time t_m) should occur outside the backward light cone of the other's measurement; that is, the distance between the two qubits must be larger than $c \times (t_r + t_m)$. Also, the measurement must occur after the entanglement is established, so that there is no chance of post-selection.

The second loophole is due to the low detection efficiency, where the result may be a selective (i.e. unfair) sample of the original distribution, and can not represent the physical truth. These loopholes have individually been closed, the latter by long distance entanglement of photons[43] , while the former by high efficiency atomic ion detection [44]. Ion-ion entanglement via photons such as what we aim for, can combine the advantages of both, and close both loopholes.

In the previous ion-ion entanglement experiment [41], The UV transition of Yb^+ are highly attenuated by the optical fiber, therefore it is difficult to set up a separation distance large enough to close the locality loophole. But barium ions' optical transitions fall in the visible and infrared spectrum and such photons can be transmitted for relatively long distance (10^3 m) with tolerable attenuation ($\leq$30 dB/km). Suppose we have two identical ion traps separated from each other by 1 mile, and two ultra-fast lasers synchronized with each other to excite the ions at the same time. The ions are then randomly rotated and detected. The photons travel through equal lengths of single-mode optical fiber to a beam splitter and project the ions into an entangled state by measurement. The coincident measurements results are saved for later data discrimination. The time allowed for the measurements is $\sim 5\times10^{-6}$ s, which is enough for ultrafast excitation ($\sim$ 100s fs)+decay($\sim$ 10 ns)+rotation($\sim$ 1 μs)+shelving for detection($\sim$ 1 μs). The second loop-hole is closed then by detecting the ion state in $\sim$ 3 μs, a hard, but feasible feat.

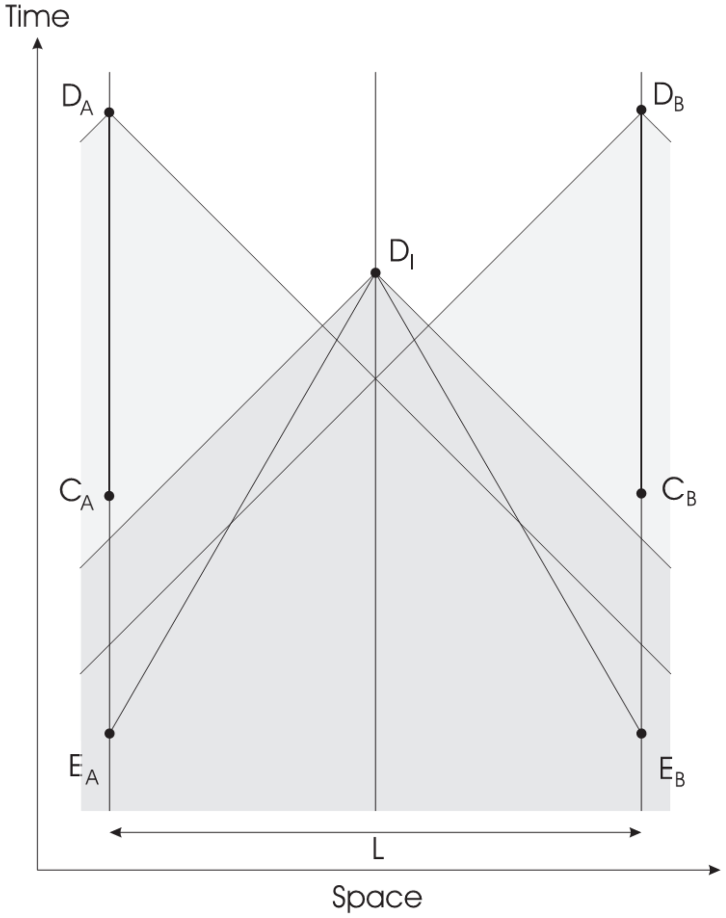

Figure 1.3: Time constraints for a loophole-free Bell experiment with remote entangled ion qubits (the figure is from [45]): Single photons are emitted at E_A and E_B. The projection measurement D_l entangles the remote ions. The choice of measurement at both sides must be done after the entanglement is setup (outside the backward lightcone of D_l). The choice of measurement (C_A and C_B)must be done out of the backward lightcone of the measurement event at the other side (D_B and D_A), so that no information can be transmitted about the measurement base choice and the measurement results

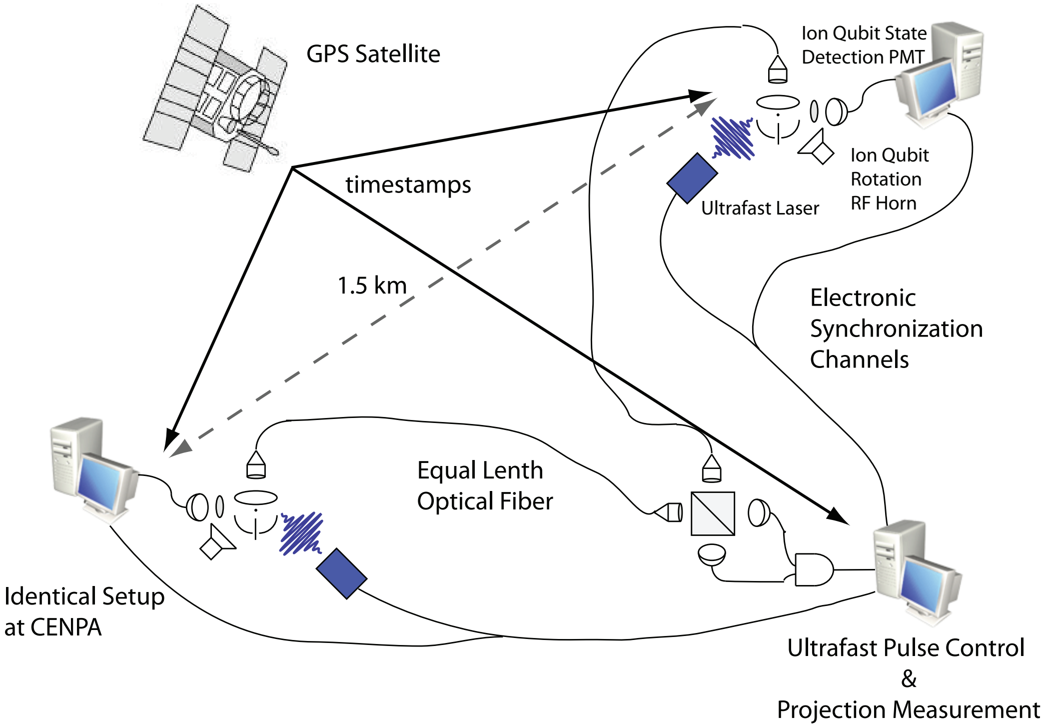

Figure 1.4: Loop hole free Bell inequality violation experiment with two Ba$^+$ qubits. Two identical trap and laser setups at two locations 1.5 km apart. The control computer triggers two synchronized ultrafast pulses to generate ion-photon entanglement at both sites. The photons go through the same length of optical fiber to reach the beam splitter. The control computer records the coincident PMT events and triggers the two qubit measurement computers to carry out the ion qubit rotations and measurements at the same time on each site. Timestamps from a GPS satellite are saved for all the actions for later data discrimination.

Chapter 2

PAUL TRAP FUNDAMENTAL

Electromagnetism is the only fundamental interaction suitable for controlling an atomic scale system, not only because it has sufficient strength and long range, but also because it has a huge spectral diversity so that atom trapping and internal state manipulation can be done without interference.

Trapping potentials for atoms or ions are normally generated by appropriate spatial distributions of electric or magnetic fields. For example, an atom's internal energy levels can be altered by an AC electric field or a magnetic field, so that the spatial distribution of such fields can be mapped into atomic potential energy. The strength of the trapping potentials generated by these methods is not very strong, at most a small fraction of the typical atomic transition energy scale ($\sim$ a few eV), which is too weak for long time trapping.

The other, more direct way is to take advantage of the charge carried by the atom (ion) and exert force on it. Charged particles can feel the Coulumb force and the Lorentz force. Paul traps[46] and Penning traps are based on combinations these two forces. In ion trap quantum computation, we mainly use Paul trap.

Trapping charged particles with electric field in free space is rather tricky because it is impossible to form a static potential well while satisfying the Laplace equation, which requires that the sum of the second order derivatives of the field to be zero at every point. This means that the field cannot increase in every direction; rather it must decrease in some direction, which will be the escape path for the ion. But suppose when the ion is escaping along that direction, before it succeeds, we reverse the field direction. Then the ion will be bounced back and won't escape.

A simple solution of Poisson equation satisfying our requirement can be expressed as:

$$\Phi = 2z^2 - r^2 = 2z^2 - x^2 - y^2 \tag{2.1}$$

It looks like a saddle as shown as in Fig 2.1.

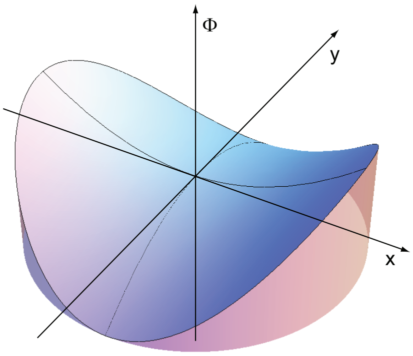

Figure 2.1: A saddle-shaped potential field formed by $\Phi = 2x^2 - y^2$

This kind of saddle field can be generated by hyperbolic electrodes conformal to the shape of Fig. 2.2. But this field only confines in two dimensions. There are multiple ways to form a full spatial confinement: we can rotate the electrodes around one of the two symmetry axes or lengthen them along the z axis and use additional "end cap" electrodes to confine the z direction. We use both schemes to construct ion traps. The motion of ions in a rotating saddle-shaped potential field can be expressed by the following equations:

$$\frac{d^2 r_i}{dt^2} - \frac{c_i Q}{Md^2}(U + V \cos \Omega t) r_i = 0 \tag{2.2}$$

where r_i $(i = x, y, z)$ are the Cartesian coordinates of the ion, Q and M are the electric charge and mass of the ion, U is the static potential, V is the RF voltage amplitude, Ω is the oscillation frequency, and for above field, $c_{x,y} = 1, c_z = -2$.

The equations can be written into the standard form of Mathieu's equation using dimensionless parameters $a_{x,y} = -\frac{4QU}{Md^2\Omega^2}$, $q_{x,y} = \frac{2QV}{Md^2\Omega^2}$, $a_z = \frac{8QU}{Md^2\Omega^2}$, $q_z = -\frac{4QV}{Md^2\Omega^2}$. Then:

$$\frac{d^2 r_i}{dt^2} + (a_i - 2q_i \cos \Omega t) r_i = 0, i = x, y, z \tag{2.3}$$

The coefficient of r_i is a periodic function, so according to Floquet's theorem, the solution can be expressed as:

$$r(t) = e^{\mu(a,q)t} \phi(t, a, q) \tag{2.4}$$

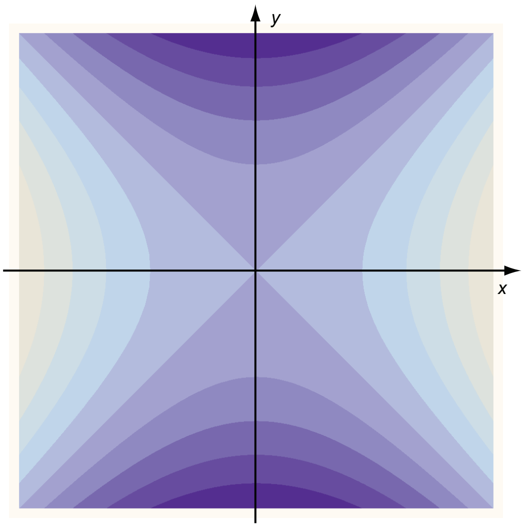

Figure 2.2: Radial contour plot of a saddle-shaped field

A stable solution requires that μ is imaginary. This restricts parameters a and q to special stability zones, as illustrated in Fig. 2.3.

The ion motion in an ideal Paul trap can be divided into two kinds: a slow oscillation with large amplitude called the secular motion and a small oscillation with the driving RF frequency called the micromotion. However, if there is any displacement between the DC minimal and RF pseudo potential minimum, large-amplitude driven motion occurs called the excess micromotion. By creating an additional DC voltage via biasing electrodes, this excess micromotion can be partially or fully compensated[47]. This is an important factor to consider during trap design.

Linear quadrapole traps have simple structure and deep trap potential. They are ideal for trapping single ions or 1 D ion crystals. The basic configuration of such a trap is shown as Fig. 2.6. Four round rods create a two-dimensional RF trap. One pair of the diagonal rods is connected to RF signal, the other pair is grounded. The two needles connected to a positive voltage (for positive charges) act as the end caps to confine the ion in the axial direction. Micromotion compensation can be done by adding DC voltage directly to the four RF rods.

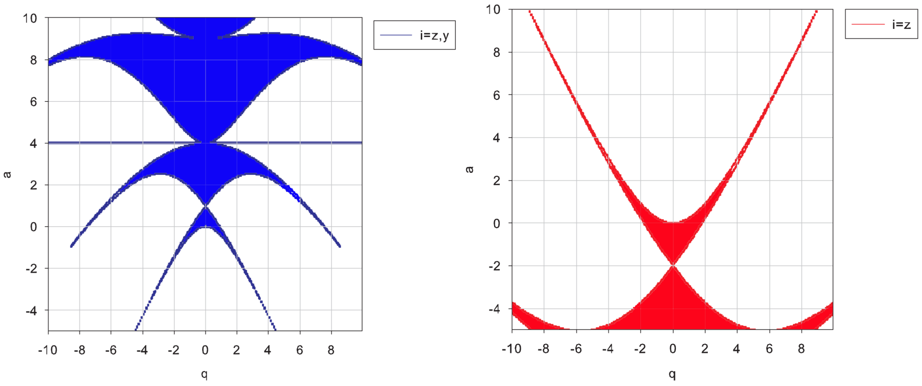

Figure 2.3: The stable zones of radial (left, blue area) and axial (right, red area) Mathieu's equations.

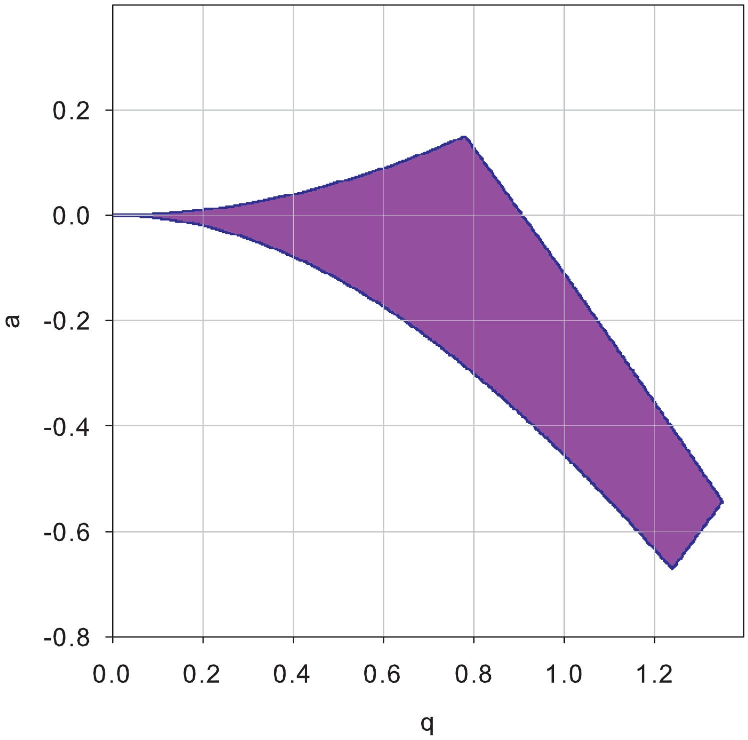

Figure 2.4: The parameters of our ion trap fall into the first overlapped stable zone of radial and axial Mathieu's equations.

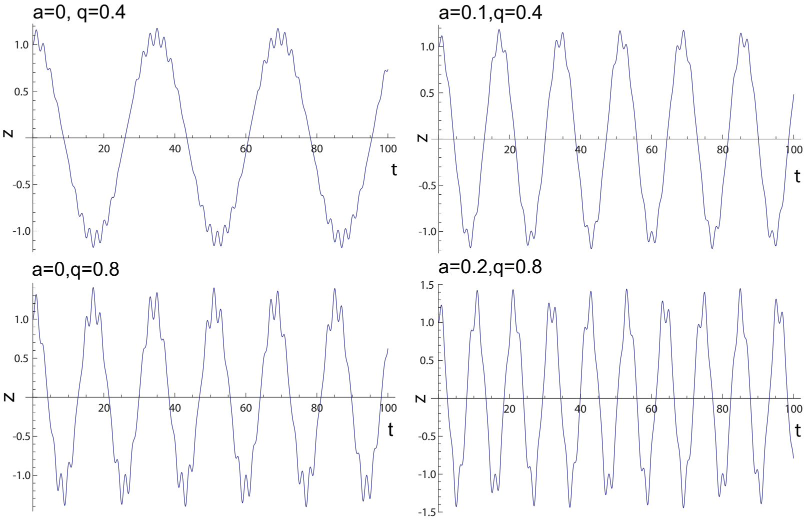

Figure 2.5: One dimensional secular motion corresponding to different a and q in the first stable zone.

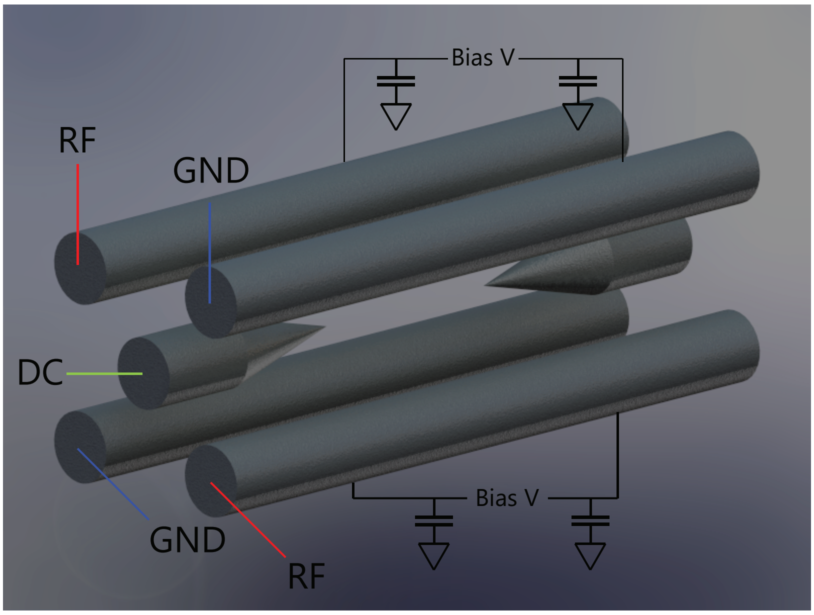

Figure 2.6: A linear quadrapole trap. The trapping field in the radial direction is generated by connecting one diagonal pair of rods to RF and the other pair to ground. The confinement along the axial direction is achieved with two positive-biased end caps. All four rod electrodes can be individually biased with DC voltage for micromotion compensation.

Chapter 3

COOLING AND TRAPPING OF BARIUM IONS

As mentioned in chapter I, Ba^+ has all of its important transitions in visible or infrared range. Coherent light sources at these wavelengths are easy to acquire and the photons are less attenuated in different forms of wave-guides, especially single-mode optical fibers. That second fact is the main reason for choosing barium ions for remote entanglement experiment.

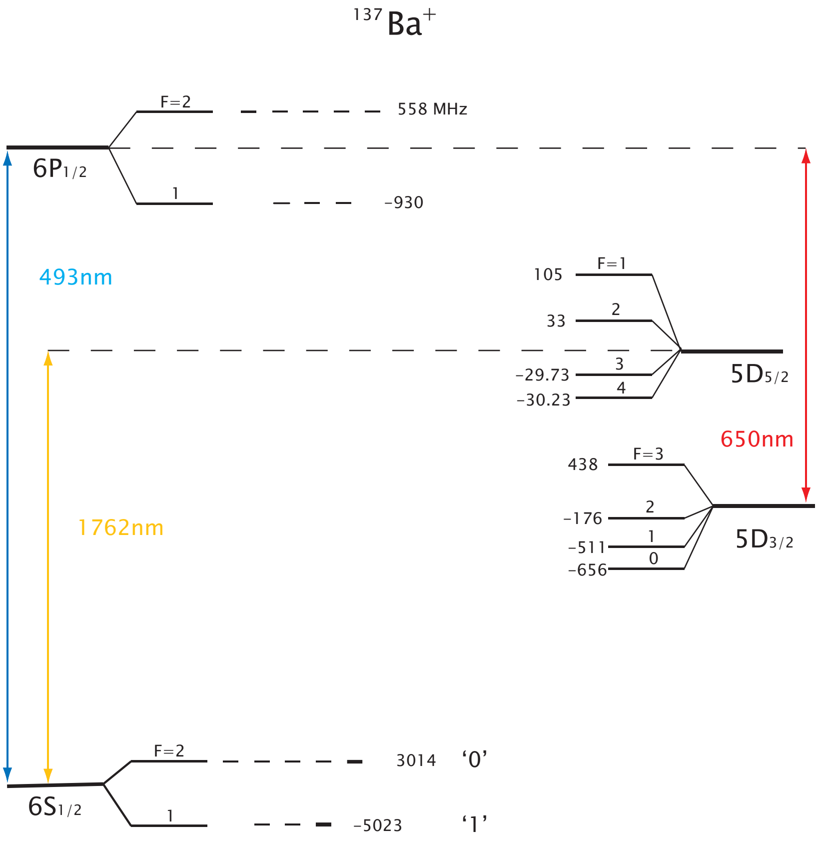

Figure 3.1: $^{137}Ba^+$ energy levels. $^{138}Ba^+$ has similar energy levels without the hyperfine splittings.

The energy level diagram of $^{137}Ba^{+}$ is shown in Fig. 3.1. The even isotope $^{138}Ba^{+}$ has simpler structure due to the absence of nuclear spin, and the qubits may be formed by the Zeeman levels of the $6S_{1/2}$ground state or between the $S_{1/2}$ and the metastable $D_{5/2}$ state. The odd isotope, $^{137}Ba^{+}$, has a much more complicated level structure. We can use the hyperfine splitting of the $6S_{1/2}$ state as the qubit, or the same optical qubit scheme as the even isotope.

We now describe in detail multiple possible qubit schemes based on different barium isotopes. Fig. 3.2 shows one possible $^{137}Ba^{+}$ hyperfine qubit scheme[48]. The ion is cooled with modulated 493 nm and 650 nm lasers to avoid optical pumping into any hyperfine levels. The qubit is chosen to be $|F = 2, m_F = 2>$ and $|F = 1, m_F = 1>$ hyperfine levels of $6S_{1/2}$. The initialization is done with a σ^{+} polarized 493 nm laser beam to optically pump the ion into $|F = 2, m_F = 2>$ state. Qubit rotation is carried out by microwave at 8.037 GHz. A small B-field (a few Gauss) breaks the degeneracy of the hyperfine levels so that a narrow-band 1762 nm laser (bandwidth$\sim 10\ kHz$) can discriminate each Zeeman level. The readout is done by selectively shelving one of the qubit states to $5D_{5/2}$ state. With the same narrow band laser, $6S_{1/2}$ and $5D_{5/2}$ can also form a optical qubit. The qubit rotation is achieved by timed pulses of the 1762 laser, and the readout is done via quantum jumps[25].

Fig.3.3 shows another hyperfine qubit scheme which is useful for ion-photon entanglement. The qubit is chosen as $6S_{1/2}$ $|F = 2, m_F = 0 >\equiv |0>$ and $|F = 1, m_F = 0 >\equiv |1>$. The initialization is done with a π-polarized 493 nm light, and the population accumulates to $|F = 2, m_F = 0>$ state. Both the qubit rotation and the readout are the same as with the previous scheme. For ion-photon entanglement, the qubit state can be coherently driven, to one of the $6P_{1/2}$ hyperfine levels with an ultrafast laser pulse which is much shorter than the excited state lifetime. The ion decays back and generates a single photon with frequency entangled with the final ion's state, so that the combined ion-photon wave function $|\phi>$ can be written as:

$$|\phi >= \cos\theta|0> + \sin\theta|1>$$

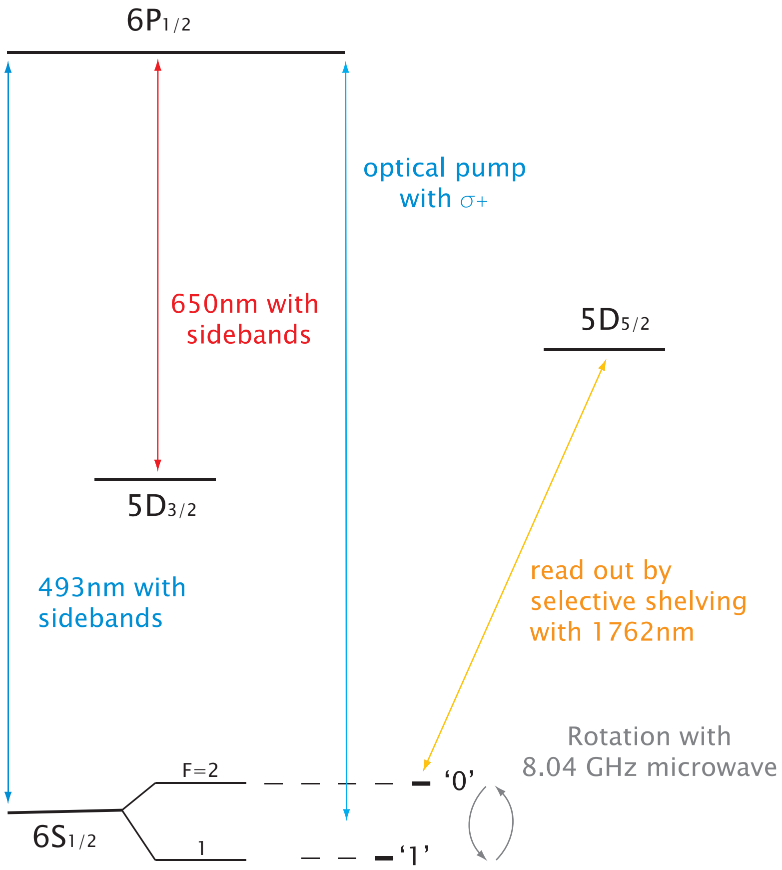

Figure 3.2: The $|F = 2, m = 2>$ and $|F = 1, m = 1>$ of $6S_{1/2}$ hyperfine levels are chosen as the qubit. The qubit is initialized to $|F = 2, m = 2>$ with σ^+ polarized 493 nm light. The qubit rotation is achieved with 8.04 GHz microwave signal. The readout is done by a narrow band 1762 nm laser (linewidth$\sim$ 10 kHz) selectively shelving one of the two qubit states into $5D_{5/2}$ state out of the fluorescence cycle ($6S_{1/2} \leftrightarrow 6P_{1/2} \leftrightarrow 5D_{3/2}$).

$$\Longrightarrow \quad \cos\theta|6P_{1/2}, F=2, m=0> + \sin\theta|6P_{1/2}, F=1, m=0>$$

$$\Longrightarrow \quad \cos\theta|0,\nu> + \sin\theta|0,\nu+8GHz>$$

To ensure that only π polarized photons are collected, a linear polarizer can be used to filter out the $\sigma^{\pm}$ decays. This reduces the entanglement generation efficiency, but increase the entangled state fidelity.

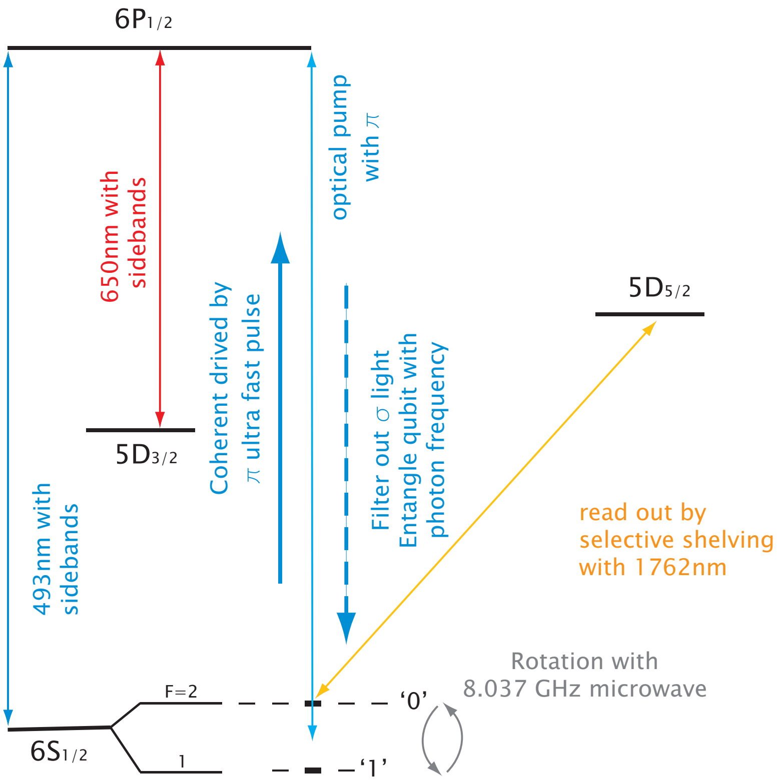

Figure 3.3: The $|F=2, m=0>$ and $|F=1, m=0>$ of $^{137}Ba^{+}$'s $6S_{1/2}$ hyperfine splittings are chosen as the qubit states. The qubit can be initialized to $|F=2, m=0>$ state with π polarized light in resonance with $6S_{1/2}, F=1 \leftrightarrow 6P_{1/2}, F=2$ and $6S_{1/2}, F=2 \leftrightarrow 6P_{1/2}, F=2$ transitions. Both the single qubit rotation and readout are the same as scheme I. To generate a single photon entangled with the ion qubit state, a π polarized ultrafast pulse coherently drives the ion to $6P_{1/2}$ domain. When the ion decays, it decays with same branch ratio to the two m=0 qubit states and generates a single π polarized photon with its frequency entangled with the qubit state. Photons with circular polarizations can be suppressed by polarizers.

A simpler Zeeman qubit scheme can be realized with $^{138}Ba^{+}$ with $m_J = +1/2 > \equiv |1>$

and $|m_j = -1/2 > \equiv |0>$. By applying a medium-size magnetic field (10∼100 Gauss), the ground state levels are split by tens of MHz. Circularly polarized light can optically pump the ion into one Zeeman level and initialize the qubit. A linear 493 nm short pulse excites the ion to $6P_{1/2}$ state (or 455nm to $6P_{3/2}$) and it decays back to ground state entangling the photon polarization ($|H>$ or $|V>$) with the qubit state:

$$\begin{aligned} & |\phi>= \cos\theta|0> + \sin\theta|1> \\ \Longrightarrow \quad & \cos\theta|6P_{1/2,m_j=-1/2}> + \sin\theta|6P_{1/2,m_j=+1/2}> \\ \Longrightarrow \quad & \cos\theta|0, H> + \sin\theta|1, V> \end{aligned}$$

The ion qubit state rotation can be done by timed RF, and readout by state-selective shelving.

3.1 Laser Setup and Frequency Stabilization

Barium ions are cooled by a 493 nm laser and repumped by a 650 nm laser. For the odd isotope, side-bands have to be added to both lasers to prevent optical pumping. The 493 nm light is generated from an frequency doubled external cavity diode laser (ECDL) and the red is directly from an ECDL. Sidebands are added to the cooling lasers individually through an EOM (493 nm) and a direct modulation of the diode current (650 nm).

The red and green lasers are combined with a dichroic mirror and coupled in to a single-mode fiber for mode cleaning and transmission. At the trap's side, the light out of the fiber is collimated and focused with an achromatic lens into the trap. A typical beam waist at the trapping center is $\sim 50\ \mu m$.

To lock the laser frequency, various schemes have been used in our lab at different times and occasions. The 493 nm laser was initially locked to a Te_2 vapor cell, and the 650 nm to an I_2 cell. Due to the operational fragility of these systems, we turned to a lock scheme based on a Highfinesse WS7 wavelength meter. The error signal is calculated from the digitized laser frequency. A PID loop then generates the feedback and turns it into voltage with an 8 channel 12 bit DAC. For an ECDL with typical frequency tuning range of 20 GHz/5V the smallest frequency step directly by the DAC is then less than 5 MHz. Finer step can

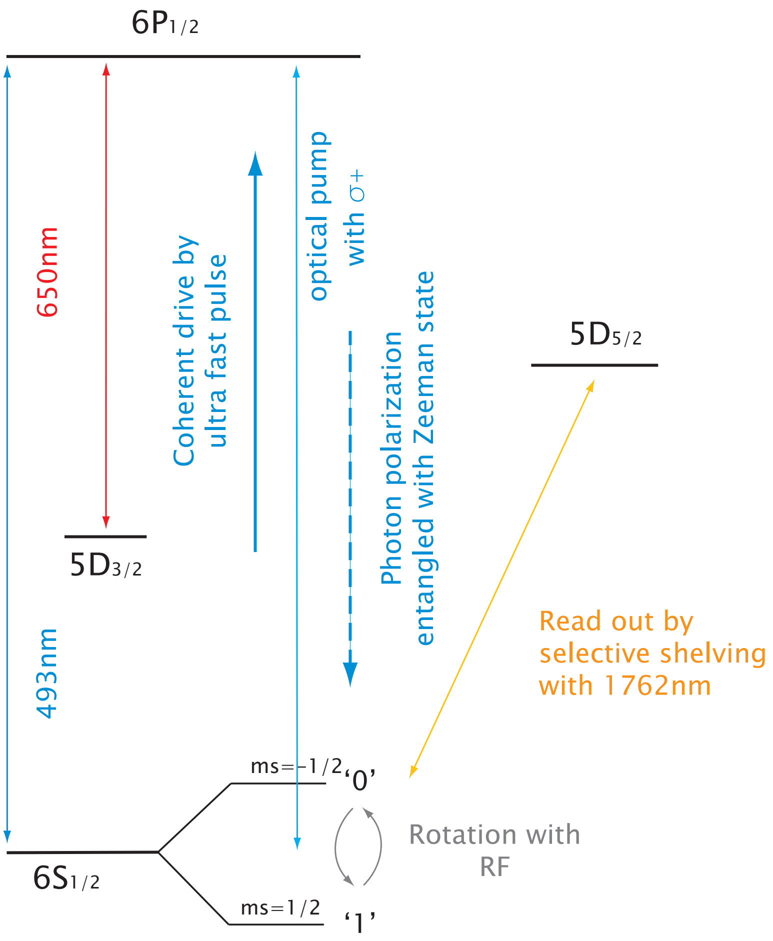

Figure 3.4: The ground state of $^{138}Ba^{+}$ can be split into two Zeeman levels tens of MHz apart with a reasonably strong B field, and they can be used as a qubit. The initialization is done with a circular polarized 493 nm light and the qubit rotation can be done by modulating the B field at the resonance frequency. The detection is the same as $^{137}Ba^{+}$ qubit schemes. Ion-photon entanglement can be generated by applying a linear polarized 493 nm ultrafast pulse to coherently drive the ion from $6S_{1/2}$ domain to $6P_{1/2}$ domain. When it decays, it generates a single photon with its polarization entangled with the ion qubit state.

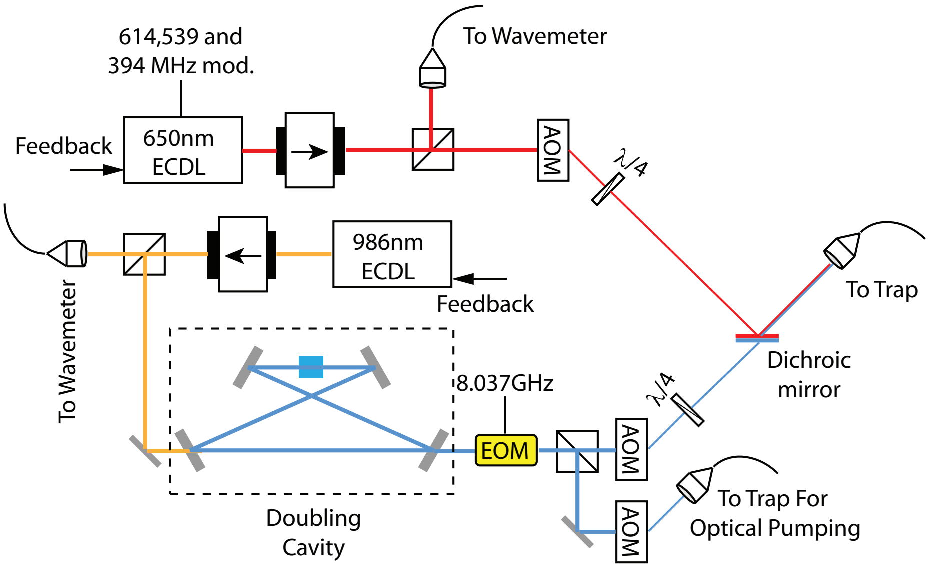

Figure 3.5: The 493 nm cooling laser is from a frequency doubled ECDL. The 8.037 GHz sideband is added to the carrier frequency with an EOM. The 650 nm repumping laser can be directly modulated with a bias-T to get necessary sidebands. Both lasers are combined with a dichroic mirror and coupled into a single-mode fiber.

be achieved with a simple voltage divider. A computer-controlled fiber switch enables the wavelength meter to read and lock of multiple lasers.

This lock scheme has the advantages of being flexible and robust. It can easily implement various locking schemes such as adaptive feedback and auto re-lock. The limitations are also obvious: poor precision and low bandwidth. The bottle-neck of the bandwidth is the wavelength meter's measurement time, which is at least 1 ms. The speed of other steps can be pushed well beyond this limit easily. For example, the DACs require at most 24 bits data which can be sent in 48 clock cycles with a 1 MHz clock. The numerical and logic calculations take no more than a few microseconds for any current PC.

The wavelength meter has a RMS precision of 60 MHz. The reading errors can be divided into two categories, one is generated by interferometer's measurement mechanism. This error show up as shot to shot noise. Except for averaging the wavelength meter's readings at the price of even lower locking speed there is no good way to avoid it.

The other error source is common for any interferometer system: temperature and pres-

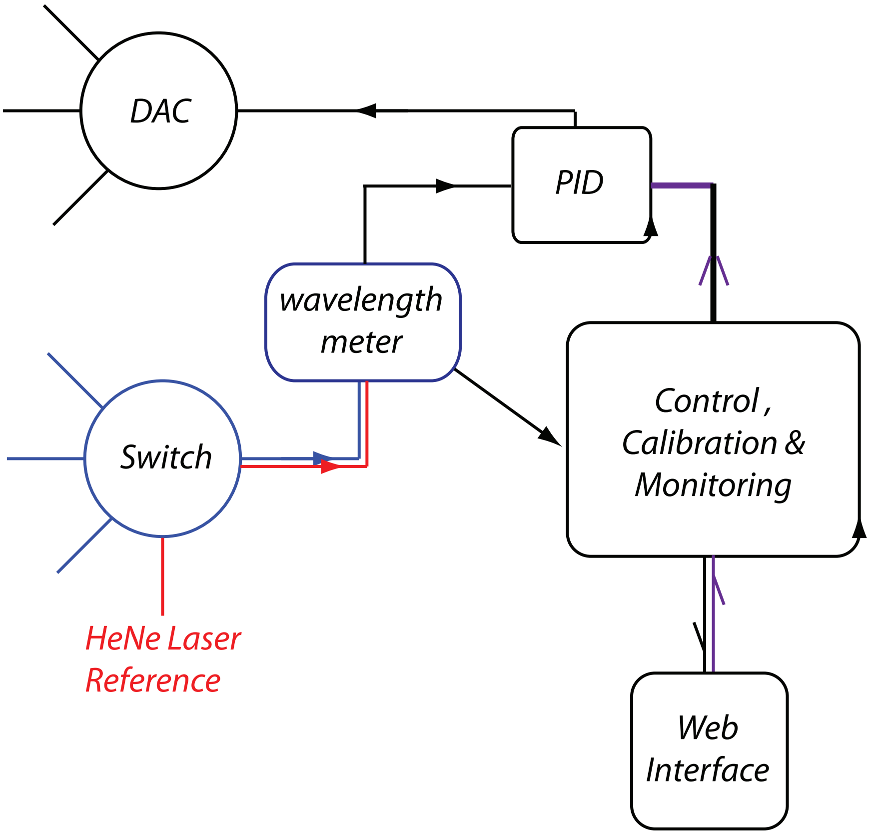

Figure 3.6: Data flow of a wavelength meter based laser frequency lock program: Multiple lasers are connected to the wavelength meter via a fiber switch. The lock program switches and locks the different channels. A frequency stabilized HeNe laser is used to constantly check to correct measurement drifts. Parameters such as exposure time, locking time and PID setup can be set via an internet interface, so that multiple remote users may share the lock. The colorful lines are optical paths and the black lines are digital paths.

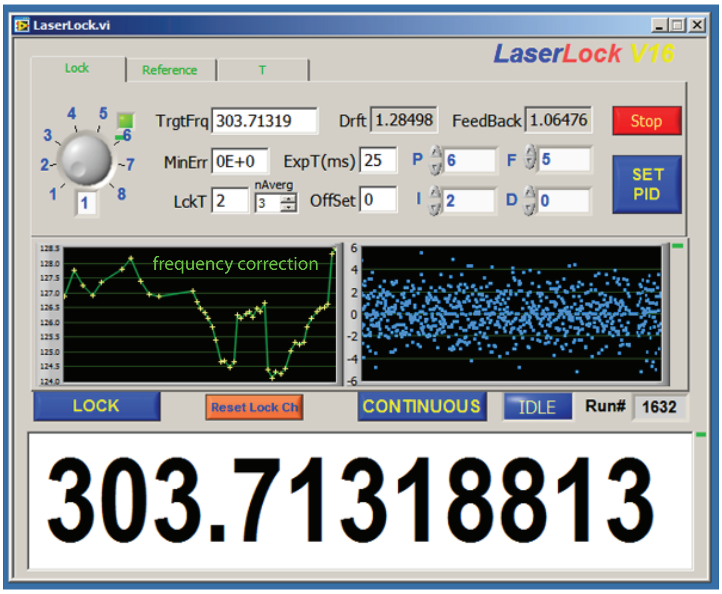

TrgtFrq 303.71319
Drft 1.28498
FeedBack 1.06476
MinErr 0E+0
ExpT(ms) 25
P 6
F 5
LckT 2
nAverg 3
OffSet 0
I 2
D 0
Run# 1632
303.71318813

7 different lasers
are monitored
in turn

Laser Frequency
locked within
+\-5 MHz

Figure 3.7: Interface of the lock program: 7 different lasers are locked or monitored in turn.

sure drifts. Both of them are continuous, slowly changing parameters and they have to be corrected by a frequency standard. We use a stabilized HeNe laser as our reference. It has a short time stability of 2 MHz and long term drift of less than 10 MHz per month. By constantly checking the HeNe laser's frequency, the wavelength meter should be free of slow drift due to the environment. To further reduce the dispersion due to temperature fluctuation, we put the wavelength meter in a insulating box temperature stabilized to $21 \pm 0.1\ ^{\circ}C$. However, we notice that the wavelength meter reading constantly gives jumps by as much as 100 MHz (Fig.3.8). The jumps are discrete, which can hardly be connected to any continuous variables. One thing comes to our attention is that the wavelength meter measures the interferometer's internal temperature and its reading is digitalized and discrete. By plotting the reading error against the temperature reading, we find they are perfectly linear correlated (Fig.3.9)!

One reasonable explanation is that the wavelength meter corrects its frequency reading according to a digital thermal sensor's plausible temperature measurements with some linear formula:

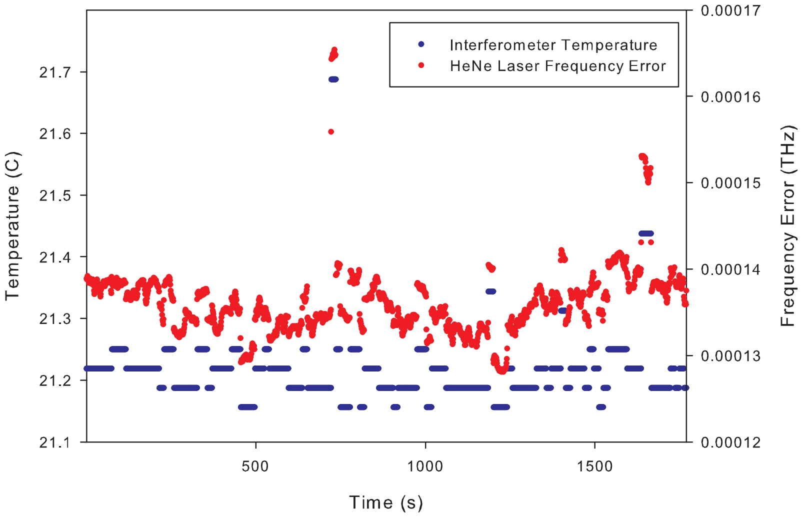

Figure 3.8: Measured HeNe laser frequency and the wavelength meter's internal temperature drift.

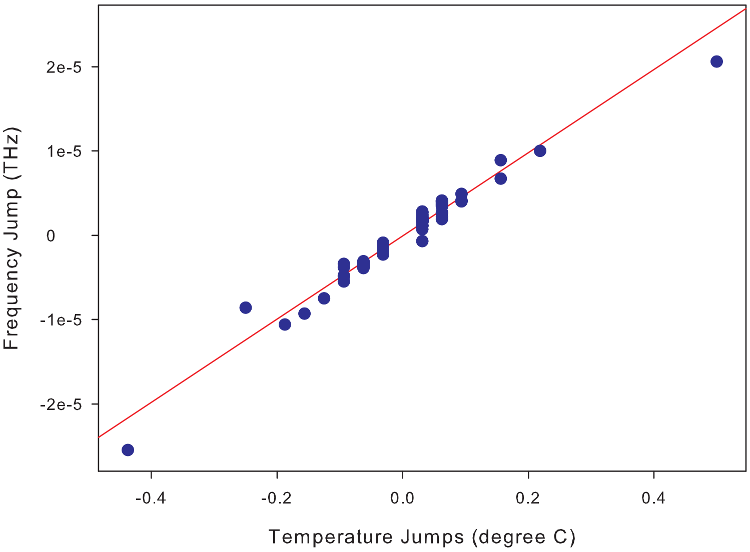

Figure 3.9: Linear correlation between the jumps of frequency reading and temperature reading. They can be fit into a line: $\Delta f = -7.9798 \times 10^{-8} + 4.9346 \times 10^{-5} \Delta T$.

$$f_{display}(t) = f_{internal}(t) + c_{cr}T_m(t), \tag{3.1}$$

where c_{cr} is the correction coefficient, t is time and $T_m(t)$ is the measured temperature.

The sensor frequently gives wrong readings and these errors are propagated by the correction algorithm . For example, an error ΔT in temperature measurement will result in frequency error $c_{cr}\Delta T$. For our locking scheme, suppose the wavelength meter measures the HeNe laser at time t_0. The calibration information can be expressed as:

$$\begin{aligned} f_{HeNe} &= \delta f_{drift}(t_0) + f_{display}(t_0) \\ &= \delta f_{drift}(t_0) + f_{internal}(t_0) + c_{cr}T_m(t_0), \end{aligned}$$

where f_{HeNe} is a constant representing the HeNe laser frequency, and $\delta f_{drift}(t)$ represents the slow drift due to temperature, pressure and all other slowly changing parameters that is corrected by the HeNe laser. It can be treated as a constant for tens of seconds: $\delta f_{drift}(t_0) = \delta f_{drift}(t_1)$. Then the wavelength meter measures another laser at a time t_1:

$$\begin{aligned} f_{realfreq} &= \delta f_{drift}(t_1) + f_{display}(t_1) \\ &= \delta f_{drift}(t_0) + f_{internal}(t_1) + c_{cr}T_m(t_1). \end{aligned}$$

Here, $f_{internal}$ can be treated as a continuous variable after averaging as mentioned before. The only fast changing quantity is $T_m(t_1)$. By reading it in real time, we can "anti correct" it:

$$f_{realfreq} = \delta f_{drift}(t_0) + f_{internal}(t_1) + c_{cr}T_m(t_0) + c_{cr}(T_m(t_1) - T_m(t_0)) \tag{3.2}$$

This "anti correct" trick can get rid of those abnormal jumps, but it can not improve the precision. With all these efforts, the lock can reach a precision of ±10 MHz. This is good enough for ion trapping and non-spectroscopy experiments.

In order to have better short-term frequency stability, we built low thermal expansion Fabry-Perot cavities to lock both lasers. These cavities have many resonance lines of different modes and it is easy to lock the lasers to reference lines within ±20 MHz of the desired frequency. When the cavity are placed in a vacuum chamber and temperature stabilized to 1 mK, the frequencies have a short term stability better than 1 MHz. The long term drift is still corrected by the wavelength meter with HeHe laser or by maximizing ions' fluorescence.

3.2 Trap and Imaging Systems

To achieve a reasonable storage time, the trap chamber has to stay at utra high vacuum (UHV) all the time. The vacuum system usually consists of a 20 l/s ion pump and a Titanium sublimation pump. The ion pump is constantly on to keep the pressure below 10^{-10} torr. An ion gauge is used to monitor the pressure. The Ti-sublimation pump is run occasionally to pump out residue gases.

The trap chamber has multiple view ports for optical access. Fused silica windows are used to allow the transmission of the UV light for photoionization. Electric and RF signals are fed in via UHV electrical feed-throughs.

The trapping RF signal is generated with a HP 8640 function generator and then amplified to up to 10 W. A helical resonator[49] with a typical Q factor of a few hundred is used to impedance-match the signal. These resonators are made of copper to achieve high Q. They get warm at high RF power and the copper easily gets oxidized. We periodically clean the resonators with dilute HCl solution to maintain a reasonably high Q. To avoid the high power RF signal leaking to other electronics connected to the chamber, all the other pins of the feed-through are filtered with low pass π-filter network. The filters are made of small surface mounted components to allow dense arrangement close to the chamber. The attenuation of RF is greater than 30 dB in these filters.

To generate barium ions, a small ceramic oven filled with barium metal is placed in the vacuum chamber. It is heated up by running current through a tungsten wire wrapped around it. Before normal operation, the oven has to be "flashed" with high current to "activate" barium by removing possible oxide. The oven normally runs at a dark-red to orange-hot state with a current between 0.8 and 1.3 A. Its effect on pressure diminishes with time.

Different ionization schemes have been tried. They include: electron gun, UV lamp, and photoionization. The electron gun has low efficiency and complicated setup, and was deserted at the very beginning. The barium deposited on the tungsten trap structure has very low work function so that photo-electrons can be excited by broad band UV light from a cold cathode deuterium lamp. The electrons are accelerated by the RF field and ionize barium atoms. This scheme has a good efficiency and large ionization area. It is especially suitable for initial trapping. The drawback is its high light background levels and charging up of insulators due to the scattered UV light. The latter may even move the trap center out of the laser beam waist.

The finest scheme so far is resonant photoionization[50]. The barium atom can be first excited to the $^3P_1$ state with a 791 nm laser and then ionized by 337.1 nm UV photons from a N_2 laser. The $^1S_0$ to $^3P_1$ transition is narrow, which is ideal for isotope selectivity. We use an ECDL to generate a few mW of 791 nm light. Even with the Doppler broadening, this ionization scheme still has a reasonable isotope selectivity. To maximize this selectivity, the 791 nm beam should be pointed perpendicular to the barium atomic beam to avoid first order Doppler broadening. This is a factor that we should bear in mind in trap building.

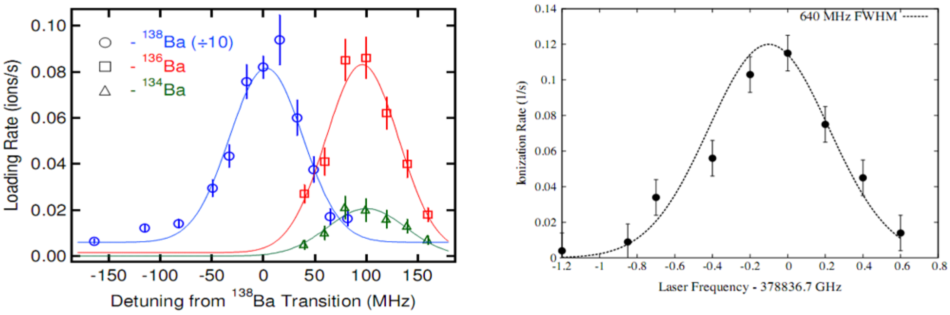

Figure 3.10: 791 nm laser ionization rates on even (left) and odd (right) isotopes (Figures from [50, 51])

The loading rate can be controlled by the pulsing frequency of the N_2 laser. It is set very low ($\sim$ 1 Hz) to ensure loading single ions with high probability.

To assist the alignment of the optics and directly image ions, we use electron multiplying charge coupled device(EMCCD) cameras. A flipper mirror switches the ion fluorescence between the camera and the PMT. The two different cameras we used are iXon^{TM} 885 and Luca^{TM}, both from Andor Inc. The iXon has a back illuminated EMCCD with a quantum efficiency of $\sim$ 90%. It can be cooled down to -90°C and the image noise is relatively low for most of the applications. The Luca has a less efficient 65% EMCCD and it can only be cooled to $-20°C$. The image is thus very noisy due to the longer exposure time and higher working temperature. A careful look at those Luca images tells that the noise is a combination of constant and random bright spots. This high spatial frequency noises can be largely eliminated with a median filter, which replaces each pixel's count with the average of the 9 counts in the 3×3 square patch covering it. The processed image looks much quieter and cleaner, as illustrated in Fig 3.11.

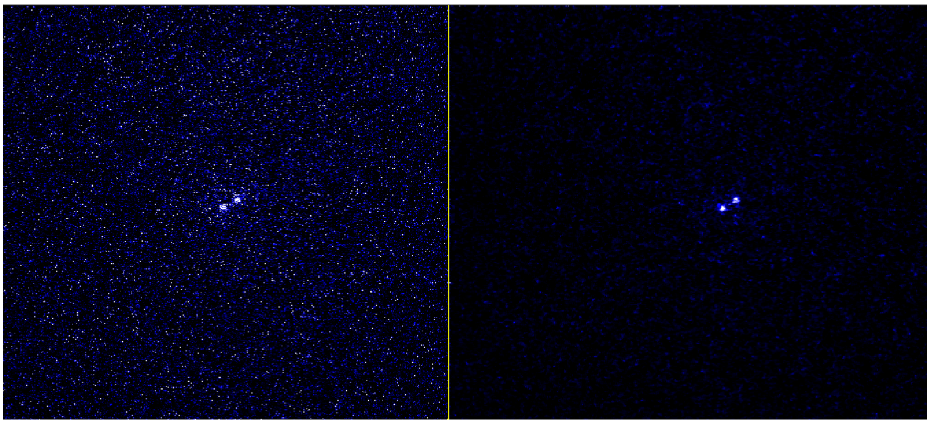

Figure 3.11: A median filter helps reduce the image noise.

We developed a program to control these cameras. It implements the filter and other useful functions such as aperture photon counting. The program's logical structure is shown in Fig. 3.12.

The filter and other data processing are CPU intensive operations. A single thread program structure freezes the interface and other LabView VIs frequently and is especially bad for some time-critical tasks, such as hardware timed PMT counting. To avoid this, we put all the heavy calculations into a stand alone thread, separated from the user interface and other LabView threads. To increase the data throughput, a circular buffer is allocated for the filter operation, so that data processing and visualization can run in parallel. The program's interface is based on LabView (Fig. 3.13) and the working thread is written in C++ for higher efficiency.

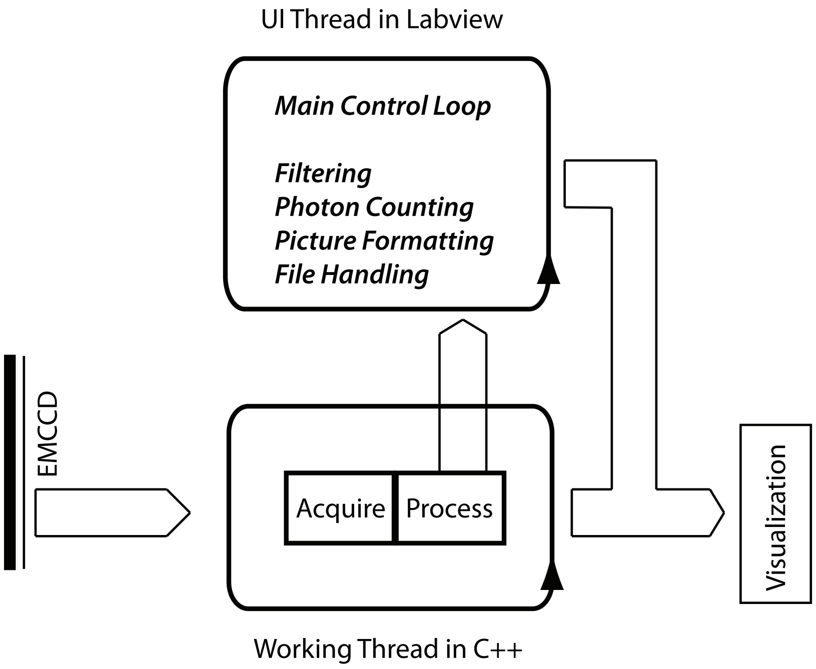

Figure 3.12: Work flow of the EMCCD camera controller program: the data acquiring and processing are done asynchronously in a stand alone working thread. The main control loop reads the processed data and carries out photon counting, visualization and file handling.

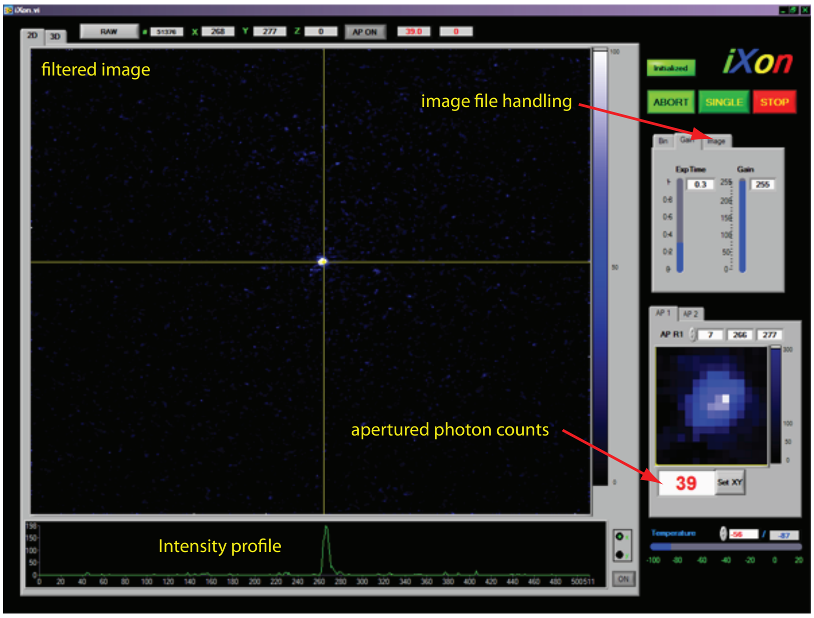

Figure 3.13: The user interface of the camera control program.

Chapter 4

NOVEL TRAP I, A LINEAR TRAP WITH AN INTEGRATED SPHERICAL MIRROR

To increase the florescence collection efficiency from trapped atomic systems, multiple approaches are available. The most common one is using large numerical aperture (NA) micro-objectives[52], which employ either large-diameter customized optics placed outside the vacuum camber or smaller aspherical optical piece inside the chamber[53, 54]. The first choice is notorious for its expense and difficult fabrication. The second one lacks flexibility and may be detrimental to ion trapping. Theoretically both setups may achieve a NA as high as 1, but practically it is very difficult and only a small fraction of the solid angle is used.

Another very promising approach is Cavity QED[55, 56]. Ions' radiation pattern can be compressed along the cavity axis which will greatly increase the effective solid angle. This can be expressed as:

$$\begin{aligned} \Omega &= \frac{2C}{2C+1}, with \\ C &= \frac{g^2}{\kappa\gamma} \end{aligned}$$

where κ is the loss of the cavity, γ is the atomic decay rate, g is the coupling constant between the atom and the cavity field and C is called cooperativity parameter. For cavity assisted photon generation, κ has to be much smaller than g to avoid reabsorbing the photons by the ion, while $g >> \gamma$ to get a large solid angle. g is inversely proportional to the squre root of field volume, therefore efficient photon collection requires a small cavity. This results in a small trap open to dielectric mirrors close-by. Small traps usually mean higher heating rate[57], and the dielectric proximity is not preferable for ions either. Efforts are made in this direction(e.g. [58, 59, 60]) though there is yet no trapped ion CQED system working in strong coupling regime. In my opinion, a reasonable scheme to integrate a cavity with an ion trap has to separate the ion loading zone and the QED zone in order to minimize the

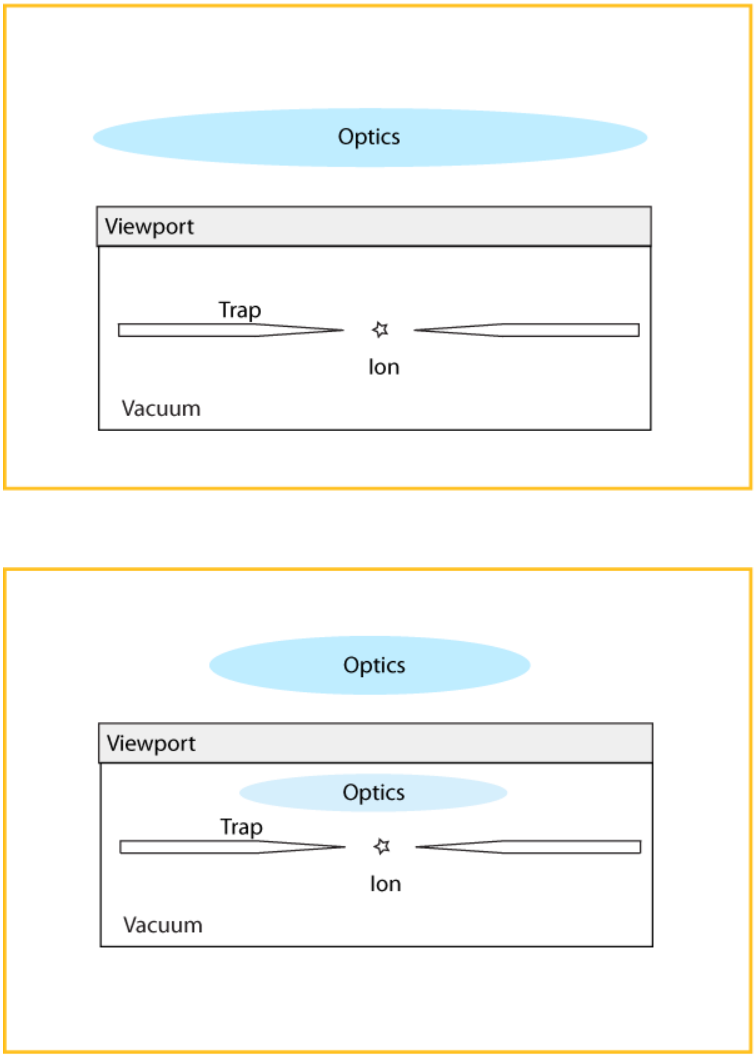

Figure 4.1: Two typical setups for large NA refractive micro-objectives: The first one uses large-diameter complex optics outside the vacuum chamber to achieve larger solid angle. It is very expensive to make such systems. the second one uses an in-chamber optics (normally aspherical) close to the source to achieve a large solid angle. The exposure of trapped ions to nearby dielectric may be detrimental for trapping.

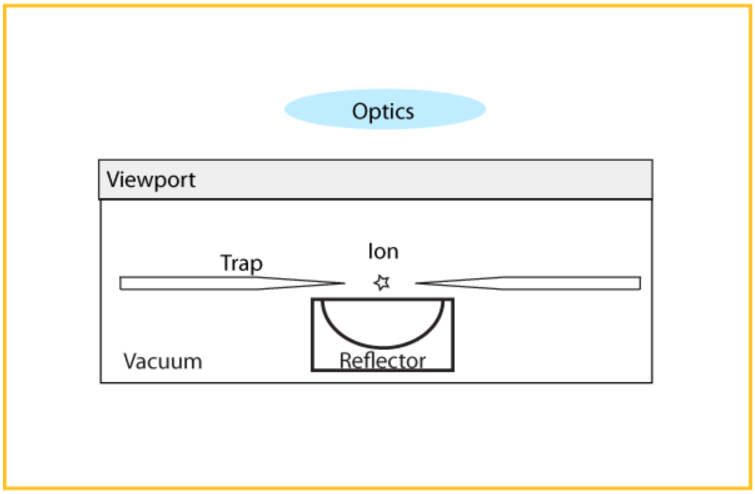

Figure 4.2: A reflective optics setup. The reflector sits in the vacuum, close to the trap. Normally the reflective surface is made of metal, therefore there will be little effect on trapping. For different reflector shapes, as few as one small size customized refractive optics is necessary to correct the image aberration.

possible charging up effect on the cavity mirrors (similar to [61]). Once trapped, ions can be transferred into the cavity with minimal trapping RF signal. One can expect this kind of solution would be based on MEMS technology, which is beyond our ability here so far.

We choose a third approach, that of metallic reflective optics. Using reflectors to increase the fluorescence collection efficiency is not a new idea[62], but it was seldom emphasized in imaging. For remote entanglement experiments based on single trapped ions, much tighter requirements are placed on the spatial mode of the fluorescence. The reflective optics may simplify the optical system and have smaller effect on trapping. A parabola is the ideal reflector for point source imaging as it has no spherical aberrations for point source at the focus [63, 64, 65]. A ”stylus” trap has already been developed for a precision parabola at NIST[66]. But machining a deep parabola is beyond our ability either, therefore we turn to spherical mirrors. The current and following chapter are dedicated to our attempts to integrate reflective spherical optics into an ion trap.

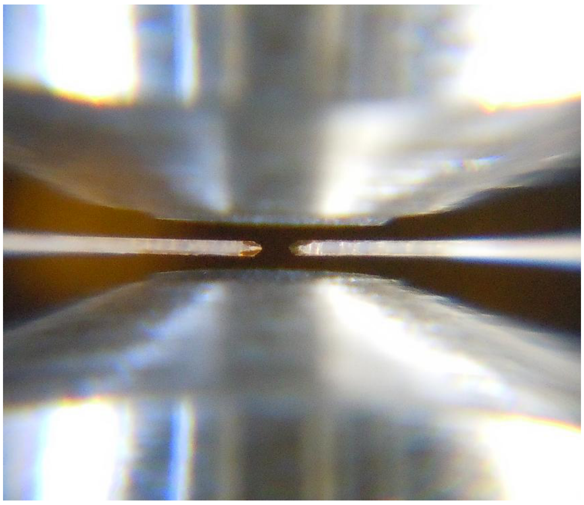

Figure 4.3: An ion trap combined with an optical cavity by Monroe Group at U. Maryland/JQI. The ion trap is a pair of needles; the cavity mirrors are above and below.

4.1 The Construction and Performance of the Trap

To prove this concept, we build a test trap based on a mature linear quadrapole trap scheme[67, 68]. The trap structure is shown in Fig. 4.4. A metallic mirror is placed under the trap to collect ion fluorescence. The 1” diameter mirror is pulled from Edmond Optics catalog (Stock No. NT43-464). The curvature radius is 20 mm, and the mirror is placed 10 mm away from the ion to collimate the fluorescence. To fit the mirror into the trap frame, it is ground into an $18 \times 18\ mm$ square. An aluminum holder supports the mirror from below. The holder is precisely machined with one circular mirror housing in the center, and two knife edges tightly to fit in the trap frame. The mirror’s vertical position is set by the holder, and its tilting angle is set by springs and set screws on the trap frame. Ideally the mirror intercepts 2.72 sr or 21.6% of the solid angle spanned by a point source at its focus.

The mirror surface is made of protected aluminum and it is grounded via a side clamp to avoid the accumulation of residual charge. To evaluate the effect from the induced surface charge distribution to a trapped ion, we study a simple model of a quadrapole trap near an infinite flat ideal conductor. We calculate the deviation of the ion due to the presence

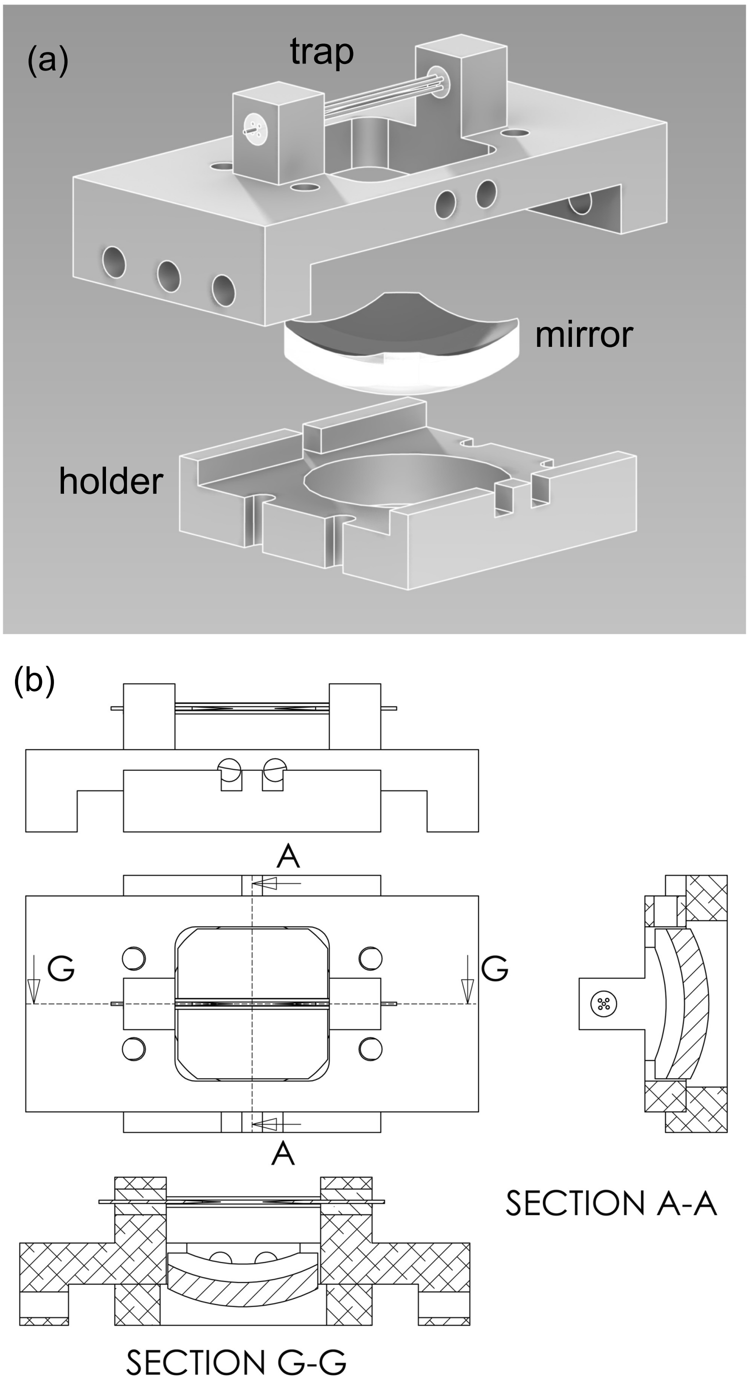

Figure 4.4: Integration of a metallic spherical mirror into a working linear trap. A 25.4 mm mirror is ground into a 18×18 mm square and attached by a precisely machined aluminum holder to a linear quadrapole trap from underneath. The mirror has a curvature radius of 20 mm, the trap center is 10 mm away from the vertex, at the focus of the spherical mirror.

of the conductor surface. As shown in Fig. 4.5, when the conducting surface is more than 4 mm away, the effect is smaller than the optical diffraction limit ($\sim 1\ \mu m$). Though the distance between the trap and the conducting plane is not much smaller than the curvature radius, this simulation is still valid because the shielding due to the four rods reduces the effect. The possible ion position shift can be compensated by applying DC voltage to the rods. This simulation is consistent with our observations: the trap captures ions and keeps them for long time. The existence of the mirror does not bring noticeable difference from a bare linear quadrapole trap. Ions can stay for days, even with no laser cooling.

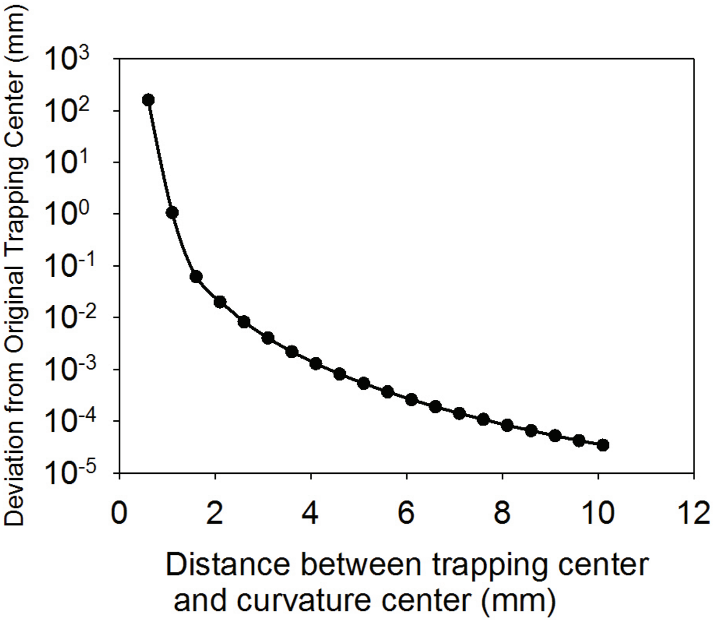

Figure 4.5: The ion's deviation due to the existence of an infinite flat ideal conductor. When the conductor is more than 4 mm away, the difference can not be optically resolved

The alignment of the end cap needles is done with the assistance of a measurement microscope. The scope has a ring light source concentric with its objective. Centering the image of the ring guarantees that the mirrors optical axis coincides with that of the microscope. The needle tips are ~1 mm away from the optical axis so that the focal point is half way between the tips.

Two barium ovens are installed, pointing perpendicular to the trap axis. The ovens are first spot-welded in place, and then small barium chunks are loaded in an inert atmosphere (N_2 gas). To avoid contamination of the mirror, the ovens are shielded with a thin stainless steel plate with small apertures. The trap is baked under vacuum at $195°C$ for two weeks, and it reaches a pressure of 8×10^{-11} torr within a month after the bake out. Fig. 4.6 is a photo of a single ion trapped in the mirror trap. The ion's fluorescence is maximized with a very low amount of cooling laser power so that we can see an ion in the background of the whole trap. The picture is taken with a micro objective at a magnification smaller than 1. Other than being fun, this image aids further alignment with the mirror.

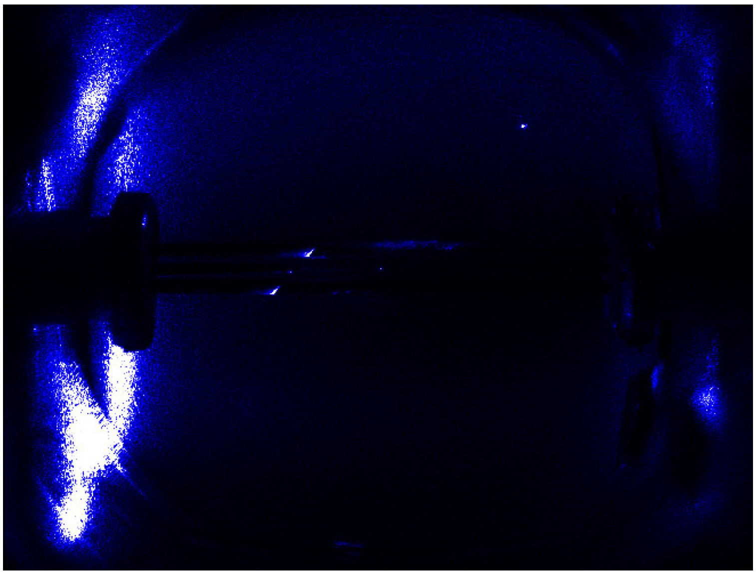

Figure 4.6: A single $^{138}Ba^{+}$ ion in the mirror trap. With a near resonance laser light at very low power, both the trap electrodes and the mirror can be clearly seen in the picture.

4.2 Direct Imaging with the Mirror

Normally the ion fluorescence is collected with a two-stage microscope shown in Fig. 4.7. The first stage is a infinity corrected micro objective with 0.1 NA. The second stage is an 25 mm achromatic doublet. The overall magnification is between 50 and 120.

Though not ideal, the mirror itself is an imaging optics. The ion is close to its focus, so

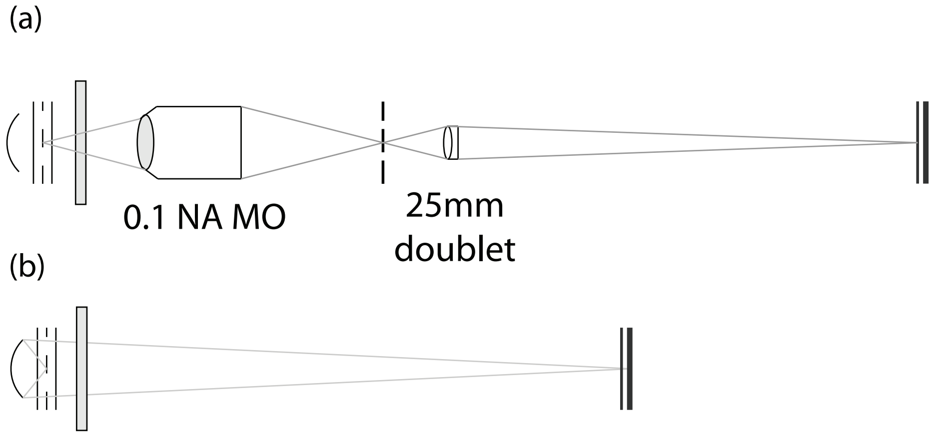

Figure 4.7: Two different optical setups for ion imaging: (a) the normal one use a 0.1 NA micro-objective for the first stage magnification. The second stage is a 25 mm focal length doublet. The magnification of the microscope is between 50 and 100. (b) the mirror can directly image the ion. The magnification of this setup is about 40.

the image should be along the symmetry axis and extended for a long range. It is found about 40 cm above the trap and 5 cm off the main optical axis. The ion image, shown in Fig. 4.8 is quite bright compared with that of a microscope. A summation of the EMCCD's pixel counts shows that the mirror collects more than 7.5 times more photons than that by the 0.1 NA microscope.

Although the background is high, the ion image still has a very high contrast ratio. Beside spherical aberration, serious coma can be seen from the picture and it indicates that the ion is off the main optical axis. The possible cause for this may be the misalignment of the end caps, and the asymmetric contact potential due to the uneven deposition of barium on the tungsten rods and needles. Though the ion image is far from good, we are able to resolve two ions $\sim 10\ \mu m$ away (Fig. 4.9).

The bright image in the picture is actually formed by the paraxial rays reflected by the central portion of the overall mirror surface. Marginal rays form rings with their diameter larger than the censor or are too dispersive to show up. Photons in this mode can hardly be used for any entanglement experiment, even in free space. We have to correct the enormous spherical aberration of the spherical mirror to fully utilize its power.

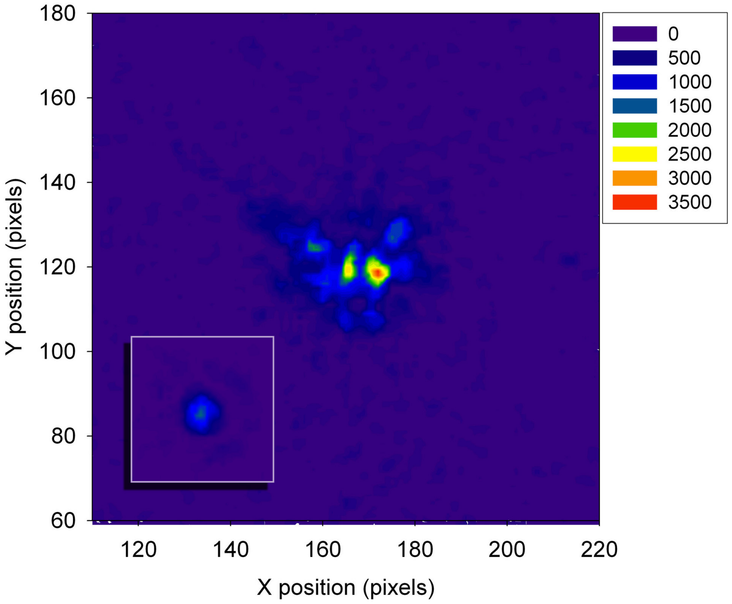

Figure 4.8: A single ion imaged with the mirror and the ordinary micro objective (insert). The image by the micro objective is faint but it reaches the diffraction limit as evidenced by the Airy ring. The image by the mirror is much brighter, but has serious aberrations.

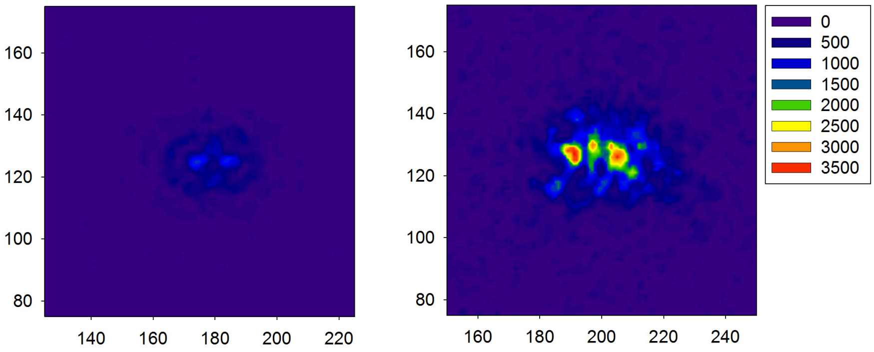

Figure 4.9: The mirror (right) can resolve two ions about 10 μm apart. Left is the image of the same ion pair formed by the diffraction limited micro objective setup.

4.3 Image Correction for the Spherical Mirror

Efficiently coupling the ion fluorescence into a single-mode fiber (e.g. Nufern 460HP with a core size $\sim 3\ \mu m$) requires a diffraction limited imaging of single ions. When the ion is close to the main optical axis, its image aberration is dominated by spherical aberration, which is intrinsically large for a spherical mirror. To correct this aberration with a reasonable number of spherical refractive surfaces is very difficult, normally what people do is use another negative spherical mirror to compensate it (Cassegraiz system), but this is impossible for our trap setup. We learn a lesson from the Schmidt corrector, another widely adopted scheme in reflective telescopes and cameras. It follows a simple principle: an aspherical corrector is added that makes the spherical mirror look like a parabolic mirror to a parallel ray bundle. The original purpose of Schmidt corrector is to increase the view field of the reflective telescope system, and its shape is based on one important assumption that the corrector only perturbs the rays slightly, so each ray maintains its parallel direction while its eigonal is increased by the corresponding corrector thickness. The corrector can be placed anywhere along the optical axis as long as the rays don't intersect with each other. This can be easily satisfied by low focal ratio systems like astronomy telescopes and cameras. But the requirement of our reflective system is a as large as possible focal ratio. The Baker camera is a corrector system with similar purpose, but it requires another reflective element close to the focal point, which is exactly what we try to avoid.

We can follow the corrector's principle that diverges the parallel ray bundle to compensate the mirror's on-axis spherical aberration. Instead of using an approximation, we directly trace each ray and numerically calculate the corrector shape. Still, we need to avoid ray crossing, therefore the corrector has to be as close as possible to the ion, but further than the focal point. Our mirror's curvature center is 20 mm away from the vertex, right outside the top window of the vacuum chamber. So the corrector has to sit right on the top window.

The problem is well within the ray optics regime, and geometrical ray tracing works. Assuming that the ion is on the main optical axis and we only need to consider the meridian rays, the 3D geometry reduces to a 2D one. The problem can be described as following:

the rays start from the ion, gets reflected by the mirror and go through the top window. The corrector bends them in such a way that the rays' outgoing slope is proportional to the distance from the main optical axis, in other words, forming a concentric ray bundle. This condition can be expressed as:

$$\frac{y}{\delta x} = \tan\theta \tag{4.1}$$

where δx is the distance between the reference plane and the focus, y is the distance between the main optical axis and the intersection point of the ray and the reference plane, and θ is a constant. For the special case of collimated rays, $\theta = 0$. Suppose that the ray hits the corrector's aspheric surface at (x, y) of the meridian plane with angle β to the x axis. Then the tangent of the surface collimating the ray at (x, y) can be expressed as:

$$\tan\theta = \frac{\frac{n_1}{n_0} - \cos i}{\sin\beta} \tag{4.2}$$

where n_0 and n_1 are refractive indexes of air and corrector material and i is the ray's incident angle from from corrector to air. The curve can be approximated with a piecewise straight sections. First, we trace a ray bundle $\{r_0, r_1, r_2, ..., r_n\}$ to the vertex of the aspherical surface $(x_0, 0)$. Then calculate the surface tangent for each ray: $\{\theta_0, \theta_1, \theta_1 ... \theta_n\}$, where θ_0 is obviously zero. Segment s_n starts from (x_n, y_n) with slope $\tan\theta_n$ and intersect with r_{n+1} at (x_{n+1}, y_{n+1}). The aspherical surface can be calculated recursively from the central ray to the most marginal ray. The n connected segments approach the exact curve from outside.

By shifting the index, we can have another segment series approaching from inside:

$$s_n : (x_n, y_n) \rightarrow (x_{n+1}, y_{n+1})@\tan\theta_{n+1} \tag{4.3}$$

Averaging the inside and outside shapes gives us a closer approximation than the original two. This can be seen from the following estimation.

The accurate curve can be expressed as

$$\begin{aligned} x_c(y) &= \int k(y)dy \\ k(y) &= \tan\theta(y) \end{aligned}$$

The piecewise curve can be expressed as

$$x_{out} = \sum k'(y_i)(y_{i+1} - y_i)$$

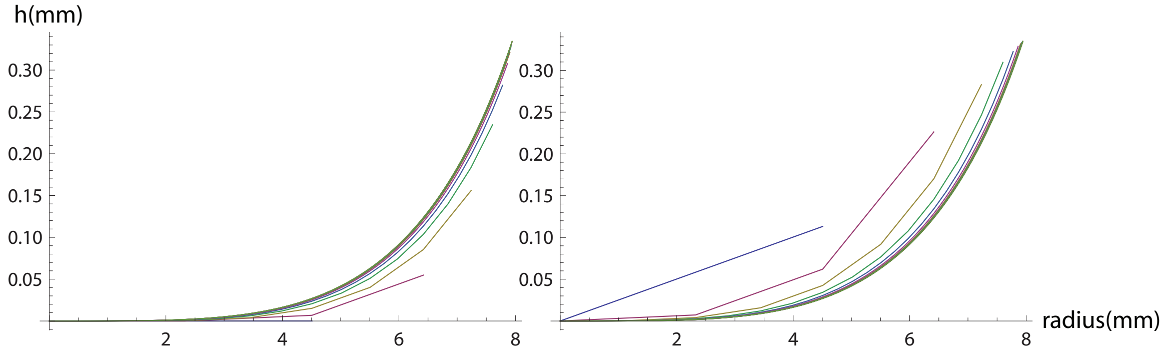

Figure 4.10: The corrector shape can be calculated with ray tracing. When the number of rays increases, the piecewise curves approach the desired shape. With different initial slopes, the piecewise curve approaches the shape from either outside or inside.

$$x_{in} = \sum k''(y_i)(y_i - y_{i-1})$$

The averaged curve is

$$x = \sum k'(y_{\xi(i)})(y_{i+1} - y_{i-1})/2 \tag{4.4}$$

The maximum difference between the piecewise curve and the exact curve is

$$\begin{aligned} \delta x &\leq \sum \left| \int_{y_{i-1}}^{y_{i+1}} k(y)dy - k'(y_{\xi(i)})(y_{i+1} - y_{i-1}) \right| /2 \\ &\leq n\ C(y_{i+1} - y_{i-1})^2/2 \\ &= n\ C(D/n)^2/2 \sim C'/n \end{aligned}$$

where C, C' and D are constants. The maximum deviation, normally at the far end from the main optical axis, is $o(\frac{1}{n})$. By choosing a large enough n, the deviation can be controlled to less than the wavelength.

To evaluate the effectiveness of the corrector, we carry out simulations with OSLO, an optics modeling software. The numerical curve can be fit into a tenth order polynomial. The setup is shown in Fig. 4.12, with an infinity corrected micro objective being used to focus the collimated beam, and Fig. 4.13 shows the points spread function for this setup. Our main concerns are the image quality and the image system's tolerance to defocussing, tilting and the deformation of the mirror shape. The results are compared with a parabolic mirror with the same diameter and NA. After correction, the spherical mirror's on-axis spherical

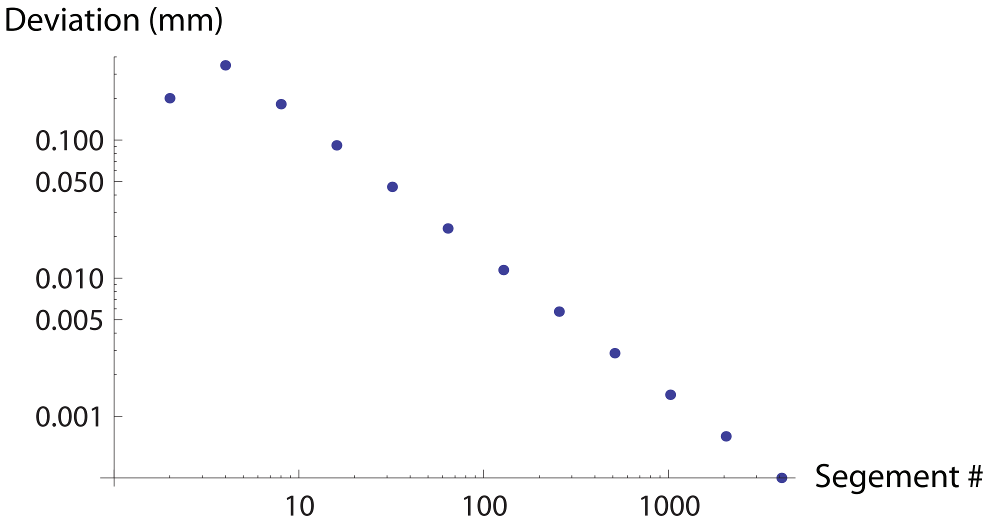

Figure 4.11: As the segment number increases, the two piecewise curves approach each other fast. By tracing more than 1000 rays, the error is smaller than the wavelength.

aberration is removed and the ion image reaches the diffraction limit. Both the parabolic mirror and the corrected spherical mirror are vulnerable to defocusings and tiltings, as can be seen in Fig. 4.14. The corrector doesn't help with this. Another practical factor is the mirror's quality. Our mirror is an inexpensive, imprecise optics piece and its radius has a tolerance of ±2%. We simulate the simplest kind of deformation by assuming the shape is still spherical but of a different radius. The result shows that even a 1% radius difference will make the spot size two order of magnitude higher than the diffraction limit.

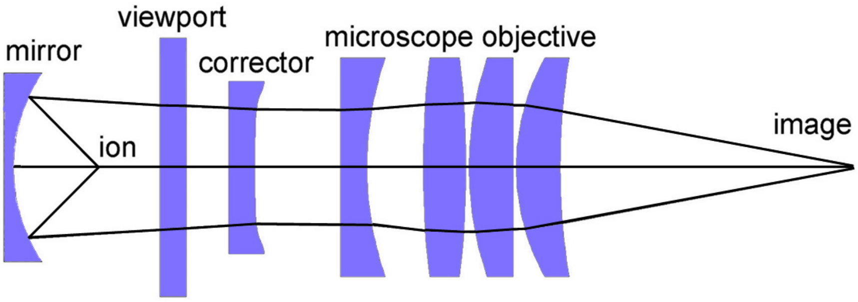

Figure 4.12: Simulation setup to evaluate the corrector's performance

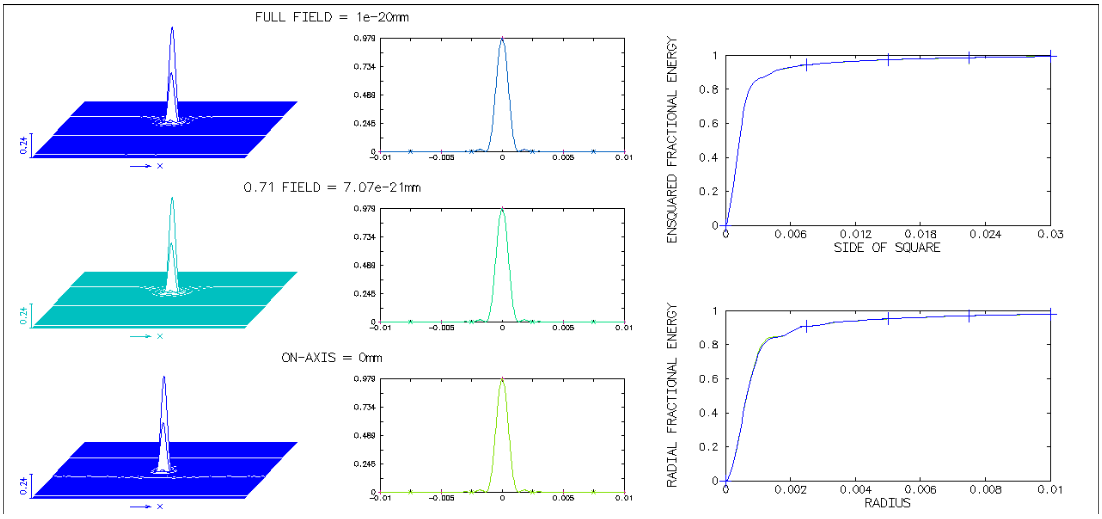

Figure 4.13: The point spread function of the corrected spherical mirror imaging system

We make a few prototype correctors out of clear acrylic plastic to test the compensation. The shapes are numerically calculated and turned into a Solidworks file for a CNC lathe machine. A clear 1" acrylic rod is first machined into the shape at a precision of 1.27 μm and then hand polished to optical grade. The polishing procedure is done in multiple steps: first, we apply a series of optical fiber polishing sand paper with roughness from 10 μm to 1 μm, then finish with a 0.1 μm alumina powder. The finished correctors are shown in Fig. 4.15.

The prototype is placed directly on the vacuum chamber's top window with a little water (n=1.33714) in between. Besides as an index-matching medium between acrylic (n=1.49691) and the fused silica window (n=1.462722)[69], water also serves as a grounding path for the corrector's surface charge, which would otherwise push the trapped ion away from the cooling beam. We use the Luca EMCCD camera to study the ion image and compare it with the same setup but without the corrector. Fig. 4.16 shows that the corrected image is much brighter than the uncorrected one. The corrector partially compensates the spherical aberration and collect more light to the focal point. Without it, the marginal rays miss the camera sensor, thus reduces the brightness of the ion image. Both images have a full width half maximum of order 10 μm, which is much larger than the mode size of a typical

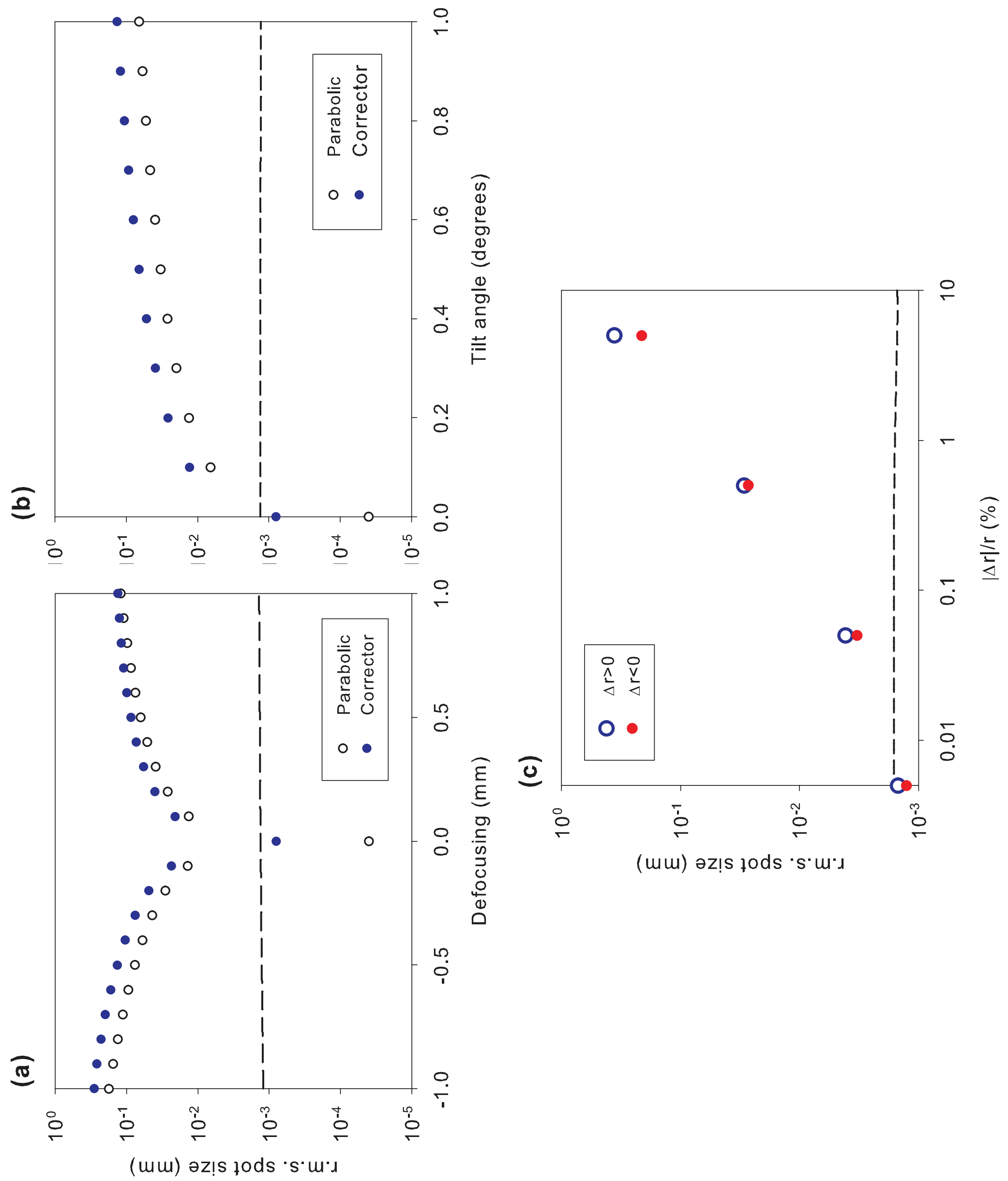

Figure 4.14: Simulations comparing the tolerance of the spherical mirror and an equivalent parabola mirror: (a) tolerance to ion defocusing; (b) tolerance to mirror tilting; (c) tolerance to mirror shape deviation. As any precision optical system, both reflectors suffer from misalignment.

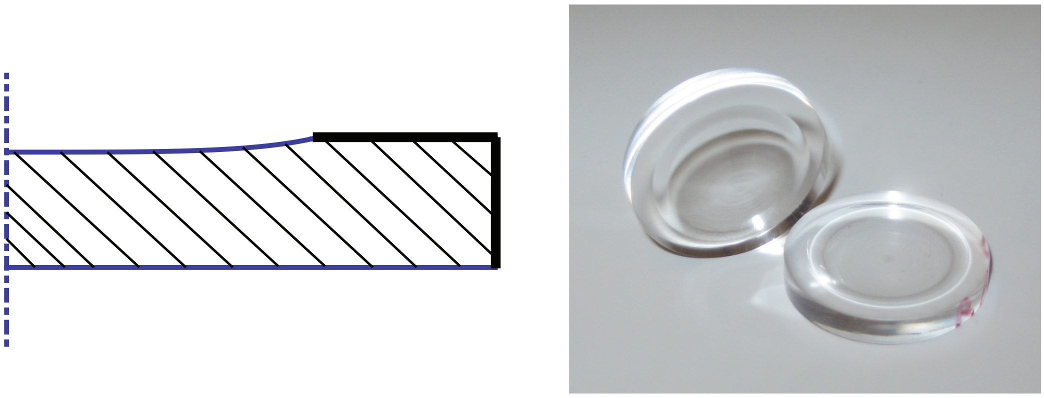

Figure 4.15: The section of a corrector and prototypes made of acrylic.

single-mode fiber. A numerical calculation of the overlap between the images and the fiber mode shows that the coupling efficiency would be 4% without the corrector and 8% with the corrector. Though both are far from ideal, the gain due to the corrector is obvious.

4.4 Single Photon Generation by Continuous Excitation

In chapter 3, a few ion-photon entanglement generation schemes based on $^{138}Ba^{+}$ are listed. All of them require ultrafast laser excitation. The generated photons have the same color as the driving pulses, which may bring large background in absence of effective spacial filtering. The 615 nm or the 650 nm photons can also be collected by turning off the corresponding repumping laser during ultrafast laser pulses. Their lower branching ratio[70] will reduce the photon generation rate, but the excitation pulses can be filtered out by interference filters. Both $5D$ states have more complicate levels, which may further reduce the ion-photon entangled state generation efficiency and increase the qubit state detection difficulty.

Beside pulse excitation, single photons can also be generated by continuous excitations. Because the photons are emitted in a much longer time span, it is more difficult to synchronize multiple sources to produce photons indistinguishable in the arriving time and spatial span[71]. This makes remote ion entanglement generation using CW light impractical. But, as a discrete fluorescence source, it can serve as a calibrator for our optics.

For simplicity, we choose the cooling cycle as the single photon generator, so that no

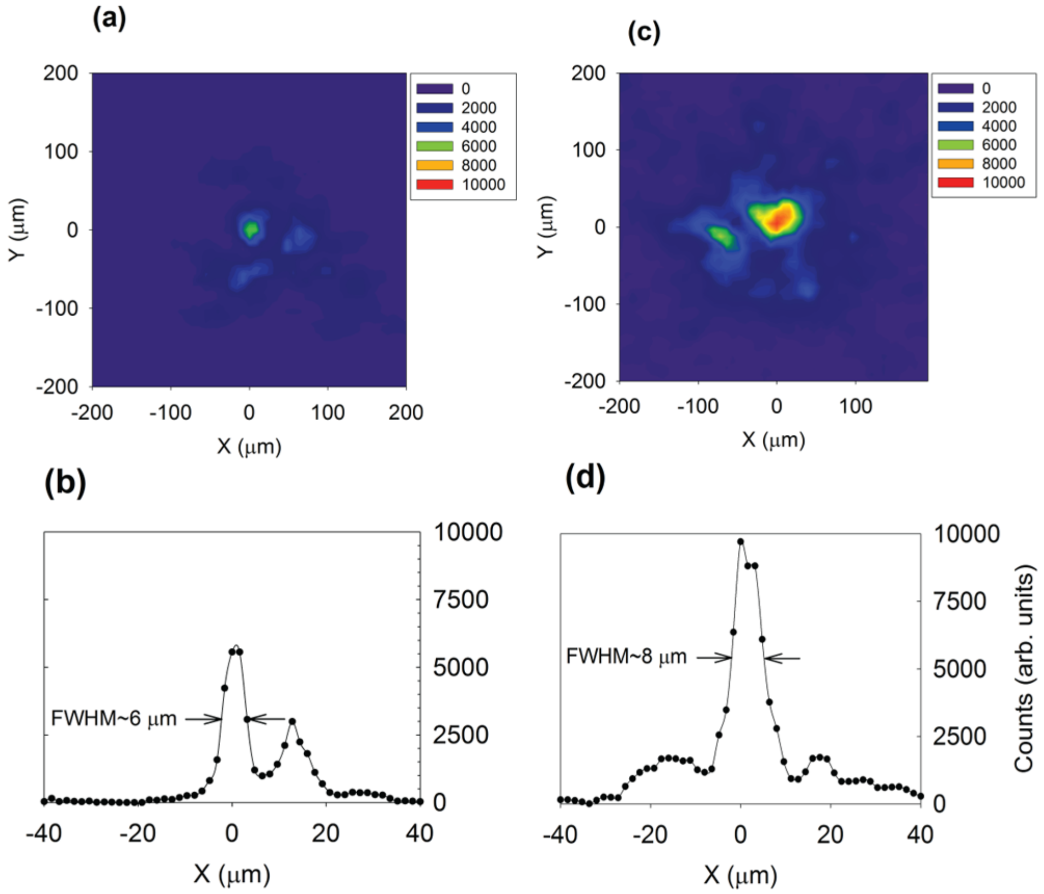

Figure 4.16: Single ion images formed by the spherical mirror without (a) and with (c) the corrector. The corresponding zoom-in intensity profile plots (Y=0) are shown in (b) and (d)

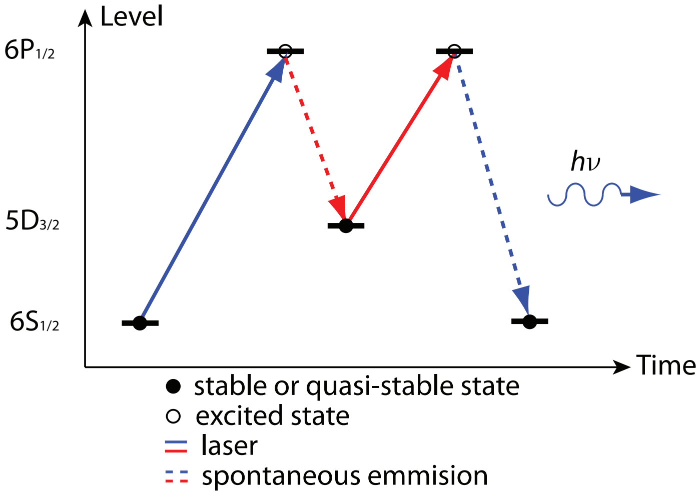

Figure 4.17: Single photon generation by continuously exciting a single trapped $^{138}Ba^+$ ion: the ion is pumped to $5D_{3/2}$ state with 493 nm light and generates a single 493 nm photon when pumped back to $6S_{1/2}$ state with the 650 nm repumping light. An interference filter is placed in front of the detector allowing only the 493 nm single photons to go through.

change is necessary for the existing setup. As shown in Fig. 4.17, the sequence is to first optically pump the ion in the $5D_{3/2}$ metastable state by turning off the red re-pumping laser while leaving the green cooling laser on. Then we turn off the green laser and turn on the red laser. The ion will be pumped back to the ground state while generating a single 493 nm photon. The single photons generated this way have a very different color from the 650 nm laser, so the background will be relatively small even without serious spatial filtering.

The main challenge here is to detect the single photon. In order to reduce the background light, PMT dark count and random noise due to cosmic rays, the detection window is set as short as possible, while keeping it long enough for the $6P_{1/2} - 6S_{1/2}$ decay to happen. Suppose the red laser saturates the $5D_{3/2}$ transition. Then the ion will decay to the ground state within a few $6P_{1/2}$ lifetimes, or tens of nanoseconds. It would be desirable to use a longer time to accommodate for possible laser frequency and power drifts. The shortest electronic pulse that can be generated with our National Instrument PCIe 6530 card is 100 ns (with its default 10 MHz onboard clock), therefor all the control patterns are in the units of 100 ns.

The digital control signal pattern is shown in Fig. 4.18. It contains a 300 ns cooling pulse with both green and red lasers on, 300 ns of green optical pumping, a 500 ns long delay to avoid green laser switching noise due to impedance mismatching, and a 500 ns red repumping with a same length PMT gating window shifted by 100 ns. Another 400 ns delay is inserted to avoid possible overlap that may be generated by electronic jitter and different time delays. The pattern can be repeated 1 million times in less than 3 seconds, which is a very short time for possible cooling laser frequency drift.

To generate the high speed signal and store the 2 million data point (both start and stop PMT counts for each round), hardware timing is implemented. As shown in Fig. 4.19, the digital pattern is first set up and stored in the main memory of the computer. Once committed, it is transfered into the board via a DMA channel and clocked out to the corresponding digital outputs. The counter is set to buffered counting mode, in which it is counting the source all the time, but only registers the number into the on-board buffer when there is a rising edge at its gate input. The data memory block is transfered back to the computer's main memory through DMA channel too (4.19).

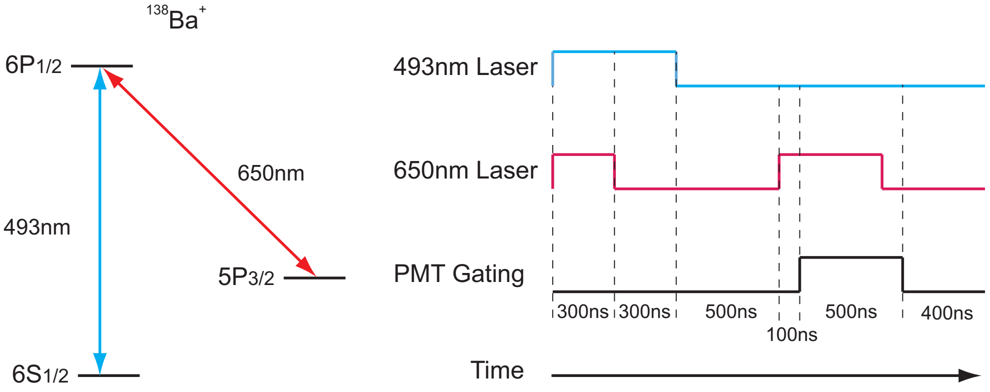

Figure 4.18: The digital pattern to generate and detect single photons: the PMT is gated to avoid 493 nm scattering light during the cooling and optical pumping.

The raw data is an array of 2 million 32bit integers, in which the odd index correspond to the start counts and the even index correspond to end counts. Once acquired, the data

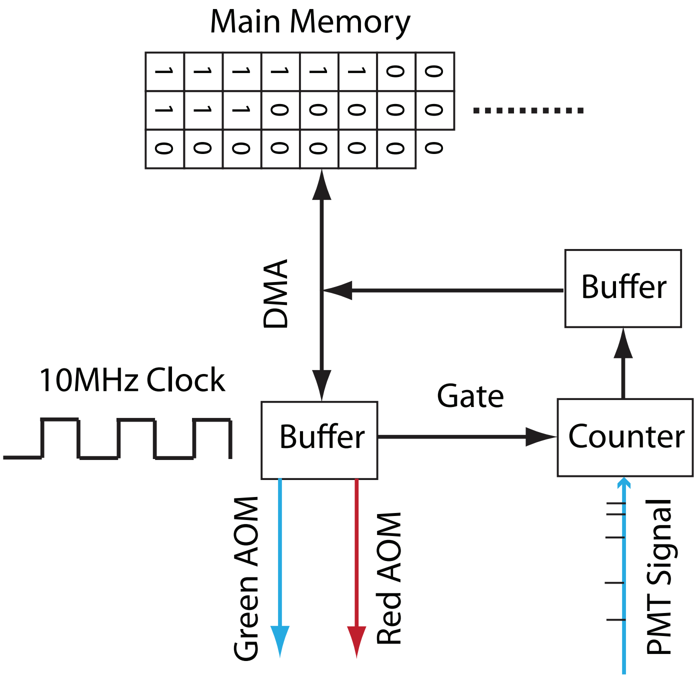

Figure 4.19: Digital pattern generation: 1 million cycles of the digital pattern in Fig. 4.18 is formed in the main memory and transfered to the NI card's on board buffer via a DMA channel. The pattern is clocked out at 10 MHz. The 2 million PMT readings are stored in the buffer and transfered back to the main memory with another DMA channel.

is processed into raw counts with a poll counting listing individual numbers of the photon events from 0 to 9. Each run consists of two individual measurements. The first one runs with the same pattern except for the red re-pumping, thus generating no single photons for background subtraction. The second one is with the red re-pumping turned on. A typical set of data is shown in the table below.

No. of Photons	Background Events	Raw Events	Effective Counts
0	998015	994834	N/A
1	1969	5137	3168
2	16	29	N/A
3	0	0	0
4	0	0	0
5	0	0	0
6	0	0	0
7	0	0	0
8	0	0	0
9	0	0	0

The background is mainly from the PMT dark counts and background light scattering. Because the PMT counting windows is short, the probability of multiple events is very small and we can simply veto them. The difference single events between the two runs are the single photons.

The physical mechanism of the single photon generation guarantees that it is impossible to have multiple 493 nm photons at each excitation. To verify this we still carry out a correlation measurement to prove it[72]. We switch the EMCCD camera for another identical PMT module and perform a $g^{(2)}$ measurement to show the anti-correlation of the two PMT counts at zero time delay. Though the signal is very noisy (Fig. 4.20), we can still see that at time 0 there are fewer photons registered, consistent with the background, which is a proof that we have a single photon source.

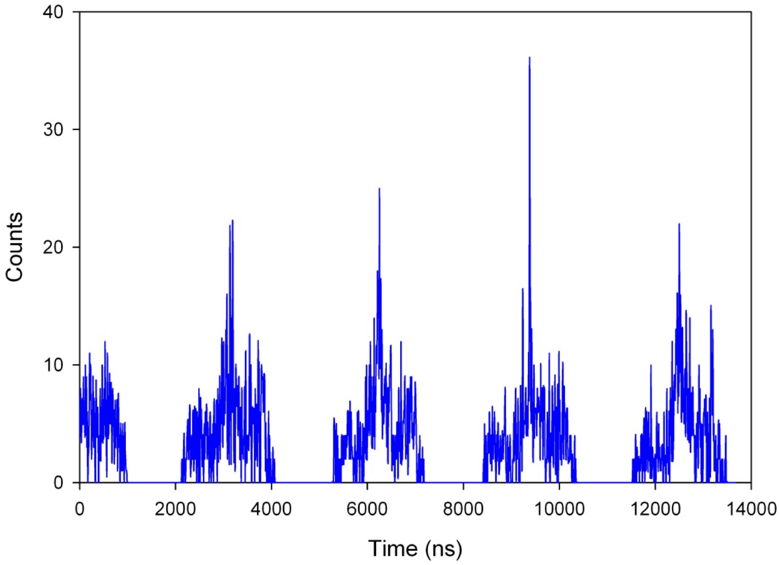

Figure 4.20: Single photon correlation measurement: Since a single photon can not be split, only one PMT register at the same time and the zero time delay the amplitude is lower. The period of the peaks is the time of the excitation cycle.

4.5 Calibration of the Spherical Mirror

To evaluate the performance of the mirror, we carry out two quantitative calibrations[73]. The scheme [74] is straightforward: A constant point source's brightness is measured through different, known NA optics and the source intensity is calibrated by fitting the measurement into the relationship between solid angle and measured intensity. Then an unknown optics NA can be estimated by the light it intercepts. For our microscope setup (Fig. 4.21), it is easy to add a calibrated iris in front of the objective to control the aperture, thus the NA.

The most direct light source is a saturated fluorescence of a single barium ion. When the laser frequency is stabilized, the ion's fluorescence intensity can be treated as constant. Figure 4.22 shows the PMT counts vs solid angle. A detailed description of the losses in the optical path will be discussed later. The fit is:

$$C_{pmt/0.05s} = 0.4787 + 17494.7478\Omega \tag{4.5}$$

where Ω is the solid angle. The corresponding fluorescence intensity is $1.27 \times 10^7/second$.

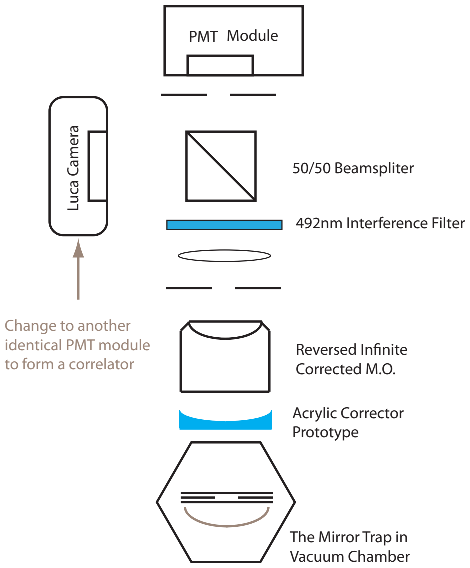

Figure 4.21: Optical setup for single photon source characterization: The ion is imaged with the spherical mirror and then focused by an infinity corrected micro-objective and further magnified with a singlet lens. A 492 nm interference filter only allows 493 nm photons to pass. A non polarized 50/50 beam splitter sends half of the photons to the PMT and half to the EMCCD camera for alignment. The camera is replaced with an identical PMT to run the photon correlation measurement.

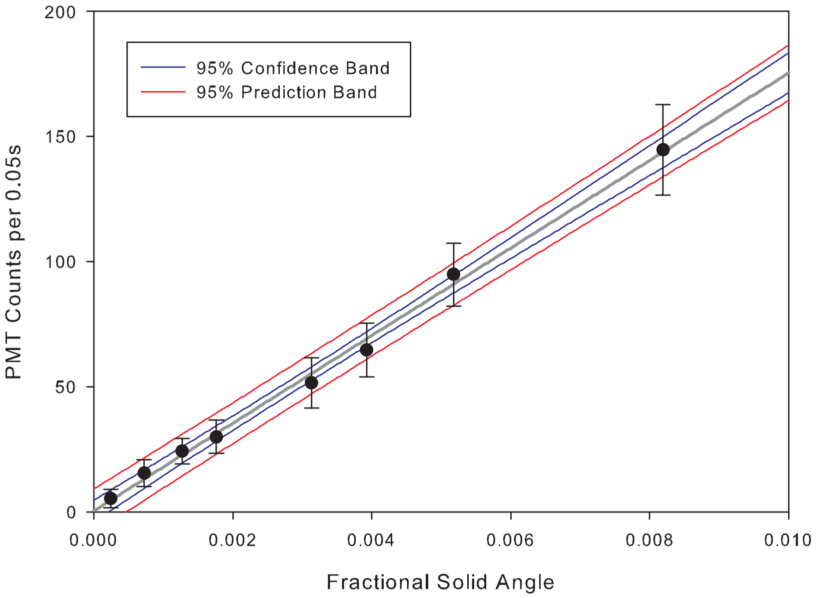

Figure 4.22: For a constant intensity point light source, the PMT count has a linear relation with the solid angle. By fitting the counts of a few setups with known solid angles, the intensity of the source can be calculated.

Using the fluorescence collected by the mirror, we can calculate the solid angle to be 1.24 ± 0.12 sr for the corrected image and 1.03 ± 0.11 sr for the direct image, respectively.

Another light source option is the previously described continuously excited single photon source. Compared with direct fluorescence measurement, the single photon source has little dependence on the laser frequency drift, ion micromotion and other environmental effect. The optical pumping times for both transitions are much longer than their saturated transition period therefore small changes in continuous parameters can hardly affect the single photon generation. This is analogous to the comparison between analog and digital electronic signals, where the former suffers greatly from all kind of continuously changing parameters, while the latter is discrete and clean. But the challenge transfers from the source side to the detection side, because it is more difficult and much noisier to detect single photons.

The PMT counts of single photons can be expressed as:

$$C = C_0 + \eta \Omega I = C_0 + \eta \Omega (I_s + I_{bg}) \tag{4.6}$$

where C_0 is the PMT's dark counts ($\sim$ 60 per 1 million excitations), η is the overall efficiency to detect single photons from the ion, Ω is the fractional solid angle of photon interception, I_s is the intensity of the single photon source in the unit of photons per experimental cycle, and I_{bg} is the background count. By taking two measurements and subtracting the background, both the dark count and the background are canceled. We get the photon count solely from the ion:

$$C_{ion} = \eta \Omega I_s = \eta_t \eta_{pmt} \Omega I_s \tag{4.7}$$

where the overall efficiency η is the product of η_t, the optical system throughput, and η_{pmt}, the quantum efficiency of the PMT ($12.7 \pm 1.0\%$). With five anti-reflection (AR) coated BK7 lenses (approximately 0.6% loss per surface), one AR coated fused silica view port (1.0% loss per surface) and one 492 nm interference filter (53.1% loss), we have $\eta_t = 0.432$ and $\eta = 0.065$. Using these numbers and the measured PMT counts for different NA values, we have $I_s = 0.976(+0.024 - 0.106)$, which is consistent with unity, as expected (Fig. 4.23). The error is dominated by the uncertainty of the PMT quantum efficiency.

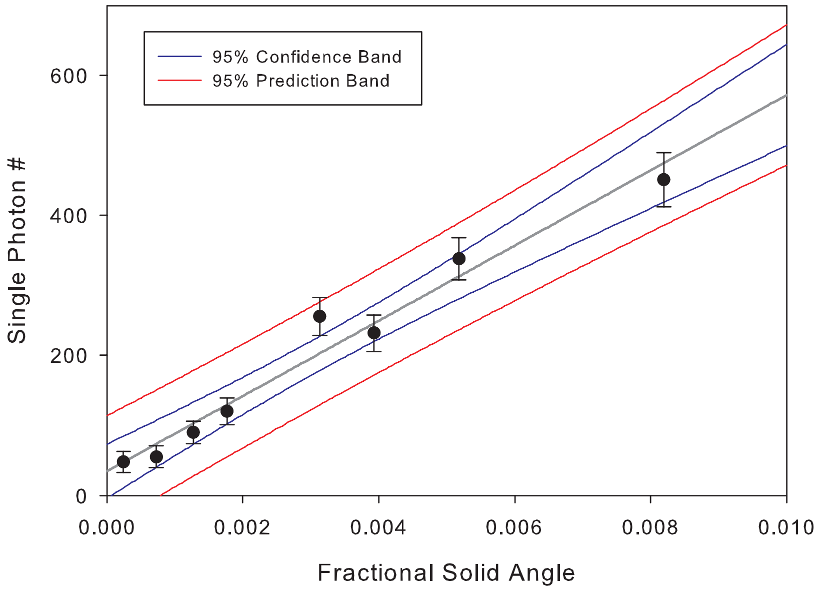

Figure 4.23: The ion is excited to generate single photons. The intensity can be measured with same scheme as for the fluorescence source.

We then repeat the experiment using the mirror with the corrector and get 4350 ± 91

single photons per 10^6 excitation cycles (statistical uncertainty), corresponding to about 0.43% raw photon detection efficiency, or 3.4% throughput to the PMT. Using Equation 2 and taking into account additional losses (aluminum mirror reflectivity loss of 9% and the uncoated corrector throughput loss of about 8.9%) we find an effective solid angle of 1.24 ± 0.13 sr (combining statistical and equipment uncertainty). Without the corrector, the count is 3981 ± 74 photons per 10^6 cycles, and the effective solid angle is 1.02 ± 0.11 sr (note that only the mirror reflectivity loss is included here). Fig. 4.24 shows the relative scale of these numbers. We can clearly see the collection efficiency boost due to the mirror and the corrector.

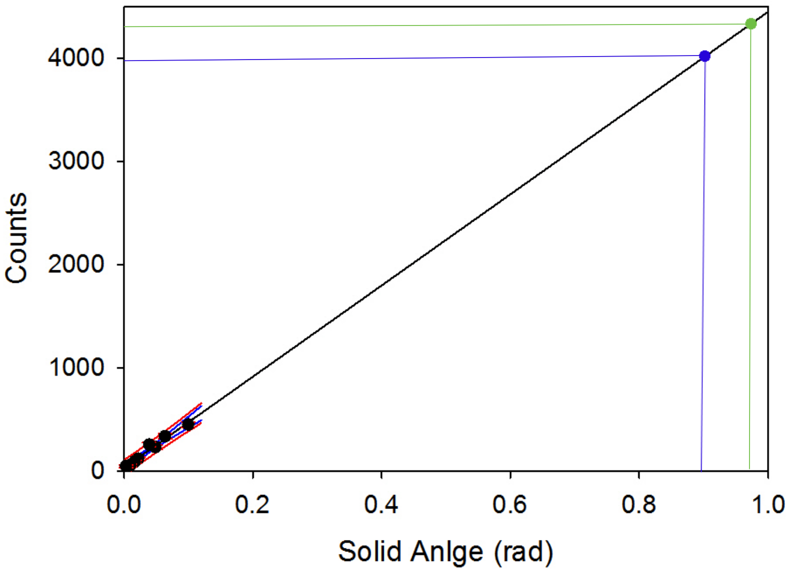

Figure 4.24: Solid angle improvement due to the spherical mirror. The blue dot is the PMT counts with the mirror, and the green dot is the counts with the mirror and corrector. The corrector helps to increase the counts further by reducing the spherical aberration, which otherwise causes the photons to miss the PMT sensor.

The estimation we did in the beginning of this chapter shows that the mirror should have an solid angle of 2.72 sr, more than twice of what we measured. The reason for this can be seen by the analysis the light blockage by the trap rods (see Fig. 4.25). The lower two rods of the linear trap actually block about 1.27 sr between the ion and the mirror;

when the photons are reflected back, the trap blocks another 4.3%. Taking this geometric factor into account, the effective solid angle is 1.39 sr, corresponding to a NA of 0.63, which is consistent with the measurements. Fig. 4.25(b) shows clearly the shadows cast by the trap structure on a defocused ion image.

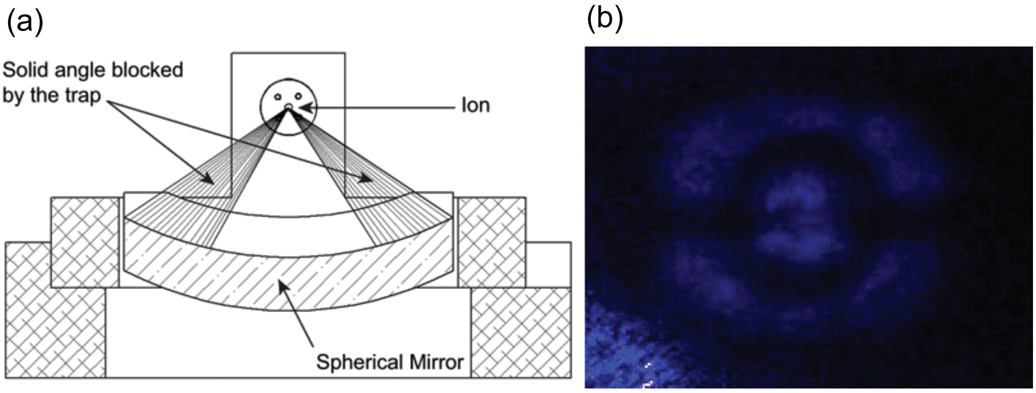

Figure 4.25: The two electrodes at the bottom block almost 50% of the photons (a). This can be seen from the shadow in a defocused ion image in (b).

4.6 Conclusion

In this chapter, we described a metallic spherical mirror integrated into a linear quadrapole trap which collects over 10% of the fluorescence from a trapped ion. We tested the idea of reducing the mirror's spherical aberration by using a customized aspherical corrector. These techniques gave us a record fluorescence collection efficiency in single ion trapping, although we didn't yet reach the ultimate goal of coupling fluorescence into a single-mode fiber. The lessons from the current trap can be summarized in the following aspects. First, a better method for precise optics alignment in vacuum is necessary. We need either a fancier trap or a better alignment mechanism. Second, the linear trap's structure is not suitable for large solid angle fluorescence collection and it has to be modified to avoid significant photon blocking. In the next chapter, we will discuss our effort of developing a new trap to address these issues.

Chapter 5

NOVEL TRAP II, THE "TACK" TRAP

5.1 Paul Trap Mutations

To solve the problems mentioned at the end of the last chapter, we designed and built a trap with a totally different structure. Before we go into the detail of its construction, it would be instructive to have an overview of the Paul trap design logic.

From Chapter II, we know the basic principle of an ion trap. The very heart of a Paul trap is a flopping saddle-shaped electric field. An ideal two-dimensional saddle-shaped field can be formed with 4 hyperbolic electrodes showed in the upper-left corner of Fig. 5.1. Practically, for objects as small as laser-cooled ions, only the field near the trap center is important. So it is not necessary to use exact shape electrodes in most of the situation, and almost arbitrary electrode shapes can be used as long as they are symmetric around the trapping point. To form a 3-D confining field, the 2-d structure can be revolved and extended along its symmetry axis. The most widely used linear quadrapole trap is formed by extension along the axial direction. The 3-D hyperbolic trap can be formed by rotating the electrodes around the symmetry axis through the GND electrodes. If we switch the polarity of the ring and end caps, it still generate a trapping potential. For both situations, the GND electrodes can be omitted since there's always ground at infinity. This generates the ring trap and needle trap with very simple structure. Minimizing the electrode number and size makes for more spatial access for optics such as lenses and cavities. Further rearranging the linear electrodes can ultimately lead to a flat trap[75], which is suitable for mass fabrication favored by current MEMS technologies.

We follow this logic to find a trap structure meeting our purposes. First, we would like a rotationally-symmetric system, because it is easier to implement precise self-alignment for optics in such a structure. Self-alignment means that the optics should be integrated into a trap system so that no mechanical alignment is necessary after the trap is built. Direct use

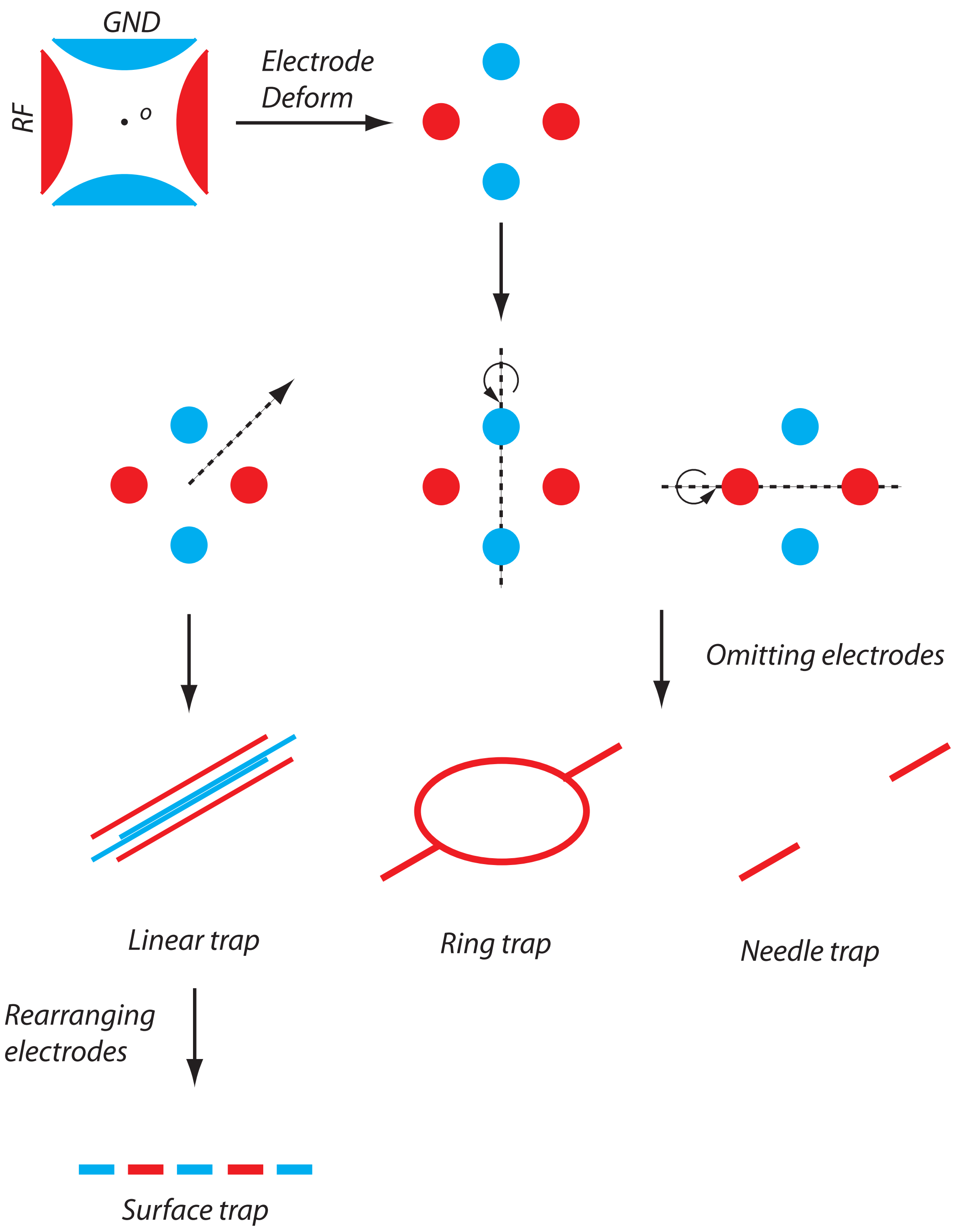

Figure 5.1: Paul trap mutations. The shapes of the electrodes are deformed for easy fabrication and large optical access. A linear trap is formed by extending the electrodes along the central axis. A ring trap is formed by omitting the GND electrodes and revolving along the central line of the RF electrodes. A needle trap is formed by revolving the RF electrodes along their axis. Surface trap can be formed by rearranging the linear trap and flattening the electrodes.

of the optical surface as the trap electrodes is the simplest answer. Second, in order to have a large optical access with no photon blocking, the trap structure has to be open. We start from a ring-needle trap in Fig. 5.8 and deform the ring into a curved surface with a hole in the center. We then remove one of the ground needles and replace it with a ring to have a large optical access. The other needle is left there to define the trapping position. Now a new trap is formed: it uses a rotationally symmetric optical surface as the RF electrode and a needle plus a ring as the ground. It meets all our requirements. With the shiny metal mirror and the needle, it looks like a paper tack, and that is where the name comes from. To study different optical configurations, we also make the central needle movable so that the ion may sit at the desire place. Additional electrodes around the trap can be used to compensate small misalignments and micromotion.

Different optical surfaces can be used for the RF electrode, as long as they are symmetric about the optical axis (Fig. 5.3). Curved surfaces such as sphere, parabola and ellipse have their respective advantages. Spherical mirror is simple and easy for both the macro and micro fabrication; parabolic mirror produces perfect image quality and can achieve a solid angle close to 4π, though it is difficult to make in both the macro- or micro- size. The elliptical mirror combines the merits of both the spherical and the parabolic mirror: it can form ideal image (on its other focus), and it is relatively easy to fabricate on large scale. Fresnel mirrors and round grating can also be use to form a planar structure; more detail will be discussed in chapter 7.

5.2 "Tack" Trap Construction

We now describe the actual design, simulation and assembling of the "tack" trap. To lower the cost and reduce the lead time, we base our design on a standard aluminum-coated spherical mirror by Edmond Optics. It has a curvature radius of 4 mm and a diameter of 6 mm. The reason to choose such a small mirror is that the geometric aberration pattern will shrink proportionally. The mirror can intercept 40% of the light from a evenly radiating point source located on the focus of the mirror (2 mm away from the vertex), corresponding to a NA of 0.977. A hole is drilled at the bottom of the mirror to fit the needle electrode. This is done on a lathe to ensure concentricity. The smallest diamond drill we are able to

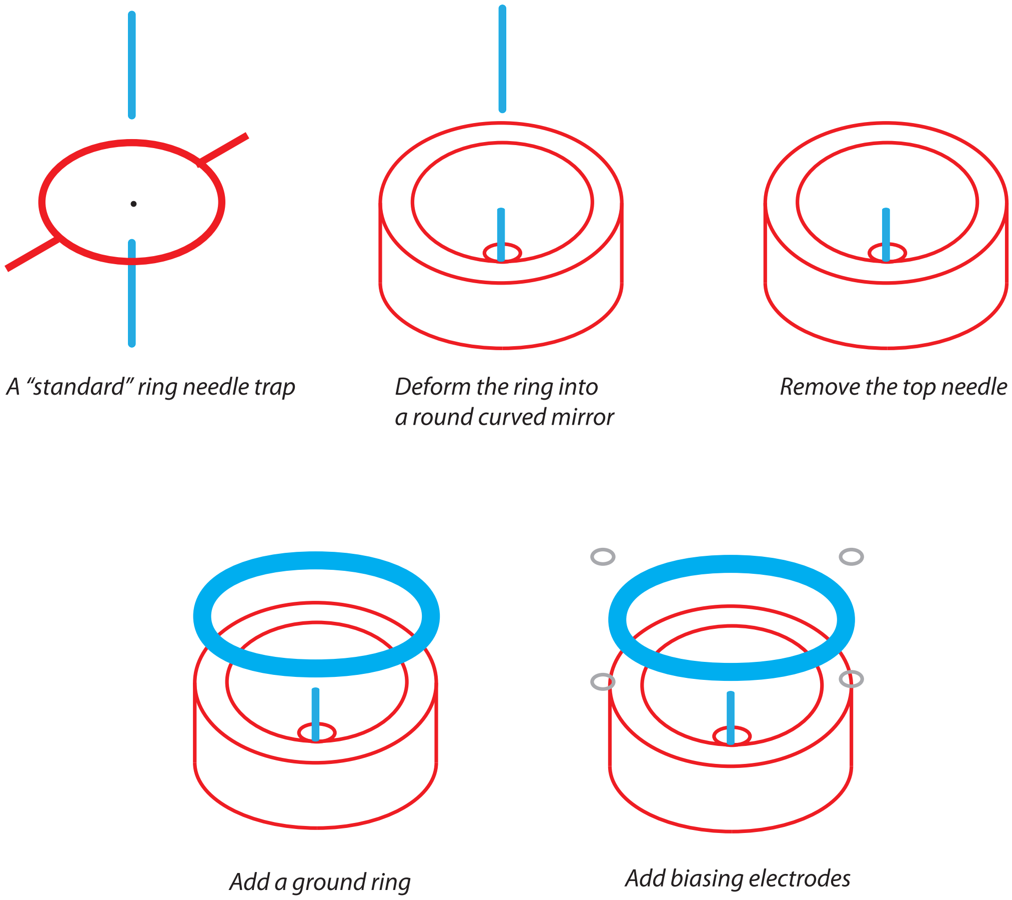

A "standard" ring needle trap

Deform the ring into
a round curved mirror

Remove the top needle

Add a ground ring

Add biasing electrodes

Figure 5.2: Design flow of the "tack" trap: start from a ring-needle trap; deform the ring into a rotational optical surface; replace one of the GND electrodes with a GND ring; add bias electrodes for micro motion compensation.

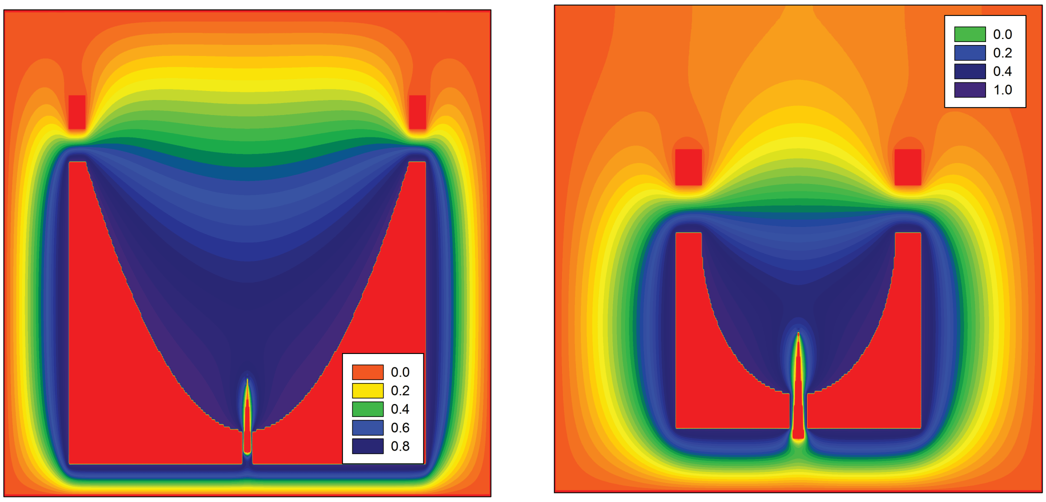

Figure 5.3: Static electric field in an parabolic (a) and elliptical (b) ”tack” trap. The saddle point always exists if a rotationally symmetric surface is used.

find is 0.75 mm corresponding to 2.5% of the surface. This is the only loss due to the trap structure. Fig. 5.4 shows four of such mirrors sitting on a U.S. penny to give a concept of their small size.

The next important component is the needle electrode. We choose a Ø 0.02” tungsten rod and sharpened it by electrolytic etching. The tungsten rod is connected to a positive voltage and dipped into a 2 mol/l KOH solution. Another electrode is emerged in the solution and connected to the negative terminal. The current is maintained around 5∼20 mA for a reasonable etching speed and voltage. To etch out the tapered shape, the needle is slowly pulled out of the solution by a stepper motor-driven micrometer. The etching procedure can be programmed in advance and carried out by computer to form different sharpness and shapes. For our purpose, the requirements are that the needle should be as symmetric as possible; the tapered side should be steep enough so that the needle itself will not block the photons from the ion, but the tip should be dull enough so that the ion would not be too close to it (Fig. 5.5). Note that electrolytic etching can easily make very fine tips of the order of hundreds of nm, which would be too sharp for our application because it would

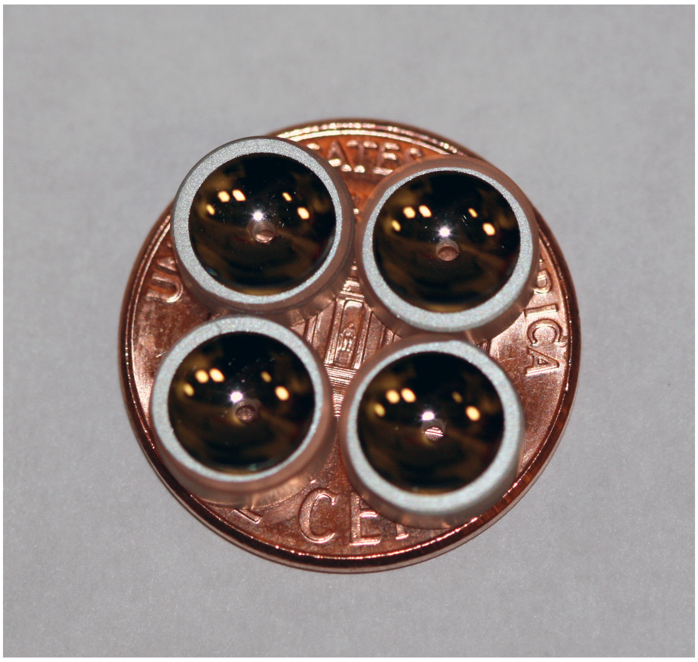

Figure 5.4: 4 small drilled mirrors on a U.S. penny.

generate a very strong field which traps the ion very close to the tip and increases the laser scattering as shown in Fig. 5.5.

A few things can be done to make the etching as symmetric as possible. We use a cylindrically symmetric negative electrode and put the rod being etched right in the center so that the electric field is more or less symmetric. The bubbles are easily formed on the rod surface that can change the local conductivity. This breaks the etching balance and makes the surface rough and the tip to point to one direction. Therefore we put a metal mesh between the positive and the negative electrodes to protect the needle and agitate the solution constantly so that the concentration of the electrolyte is kept uniform. A smooth rounded tip can be made by etching twice, where the first etching generates the sharp taper, and the second a round needle tip.

To house the mirror and the needle to a Kimball Physics MCF450-SO2008 vacuum chamber, a precision aluminum structure is made, shown in Fig. 5.6. The round mirror pocket and the needle mounting hole are carefully machined to be concentric and tightly

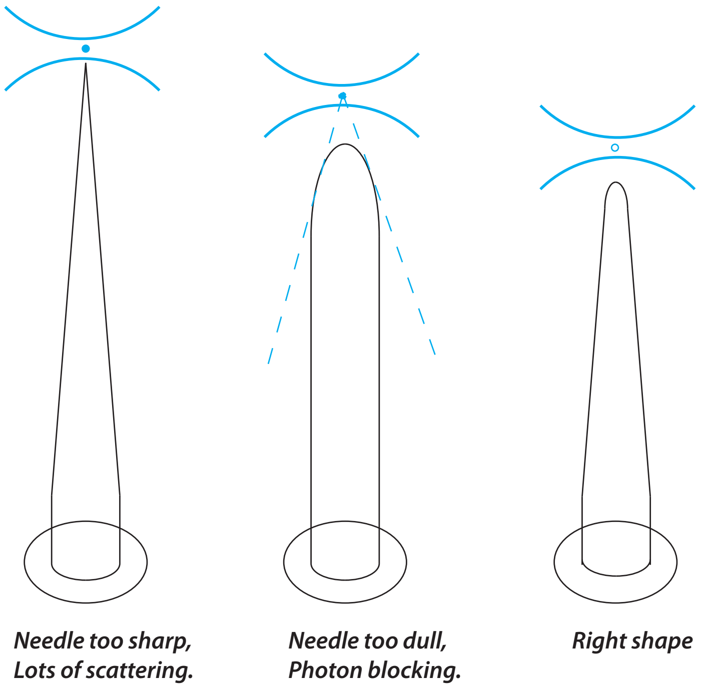

Figure 5.5: Different needle shapes. Left: the needle is very sharp and generates a very strong field. The ion is pulled too close to the needle and the tip scatters a lot of the cooling laser light. Middle: The needle is too dull and it blocks the fluorescence from the ion. Right: the correct shape of the needle combines the round tip and steep slope to avoid both the strong scattering and the photon blocking.

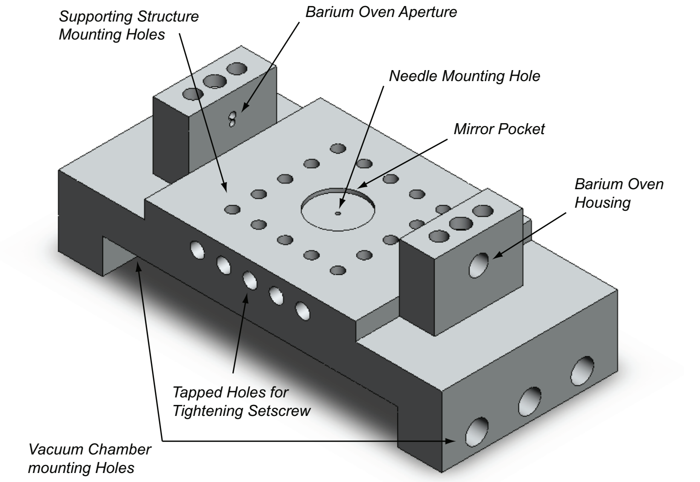

Figure 5.6: The mirror holder is precisely machined from an aluminum block. A pocket is bored for the mirror to keep it concentric with the needle hole.

fit one specific mirror to ensure the alignment. The hole for the needle has a diameter of 0.021", slightly bigger than the tungsten rod. The two ear-like structures on either side of the frame support the multiple electrode layers, and the barium ovens: The apertures are made to collimate barium atomic beam. Mounting holes are drilled around the mirror to hold the supporting rods.

To keep the needle aligned and straight, a needle guide (Fig. 5.7) is machined to match the frame from its bottom. The diameter of the long guiding hole has to be enlarged (Ø0.052") for easy machining. A ceramic tube with the same outside diameter as the guiding hole and inside diameter as that of the tungsten rod is placed between the needle and the guide to allow the needle to move smoothly along the ceramic tube. The guide is screwed to the bottom of the trap frame along two dowel pins to ensure the precision.

Fig. 5.8 shows the detailed structure of the trap. Four Ø0.06" alumina rods are fixed by $\#3-56$ screws to the four mounting holes. They are the guiding beams for the electrodes. The mirror is placed in the pocket. A 0.75" × 0.75" × 0.0125" stainless steel plate with a Ø0.25" round hole in the center is pushed against the mirror. The mirror's metal surface is electronically connected with the RF signal through this plate. Four alumina spacers with

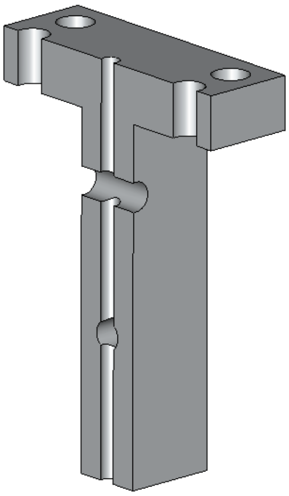

Figure 5.7: The cross section of the needle guide. It keeps the needle vertical and moving smoothly.

four stainless steel ring electrodes sit above the RF plate along the guide beams. The four ring electrodes will be separately connected to DC voltages to compensate ion micromotion and to correct ion misplacement. The needle guide with the alumina tube is screwed from the bottom. Another hollow stainless steel plate is laid on top of the spacers and used as the ground electrode. Finally, a 0.03" thick stainless plate clamps down the whole structure. The top clamp presses both the ground plate and the RF plate tightly so that they deform slightly from a perfect circle, which removes the degeneracy of the trapping potential in the horizontal plane.

The trap structure is mounted into the vacuum chamber with two groove grabbers. There are eight side viewports on the chamber. The two along the long axis of the trap structure are used for electrical feed-through, and the other six are the view ports for optical access. The oven is then placed on one side of the trap. The barium beam is collimated by the small aperture to avoid coating nearby electrodes, especially the mirror. The fully assembled trap is shown in Fig. 5.9.

The needle is attached to a UHV-compatible linear actuator with a moving range of 1". Fig. 5.10 shows an overview of the vacuum system. To make the system compact, the main

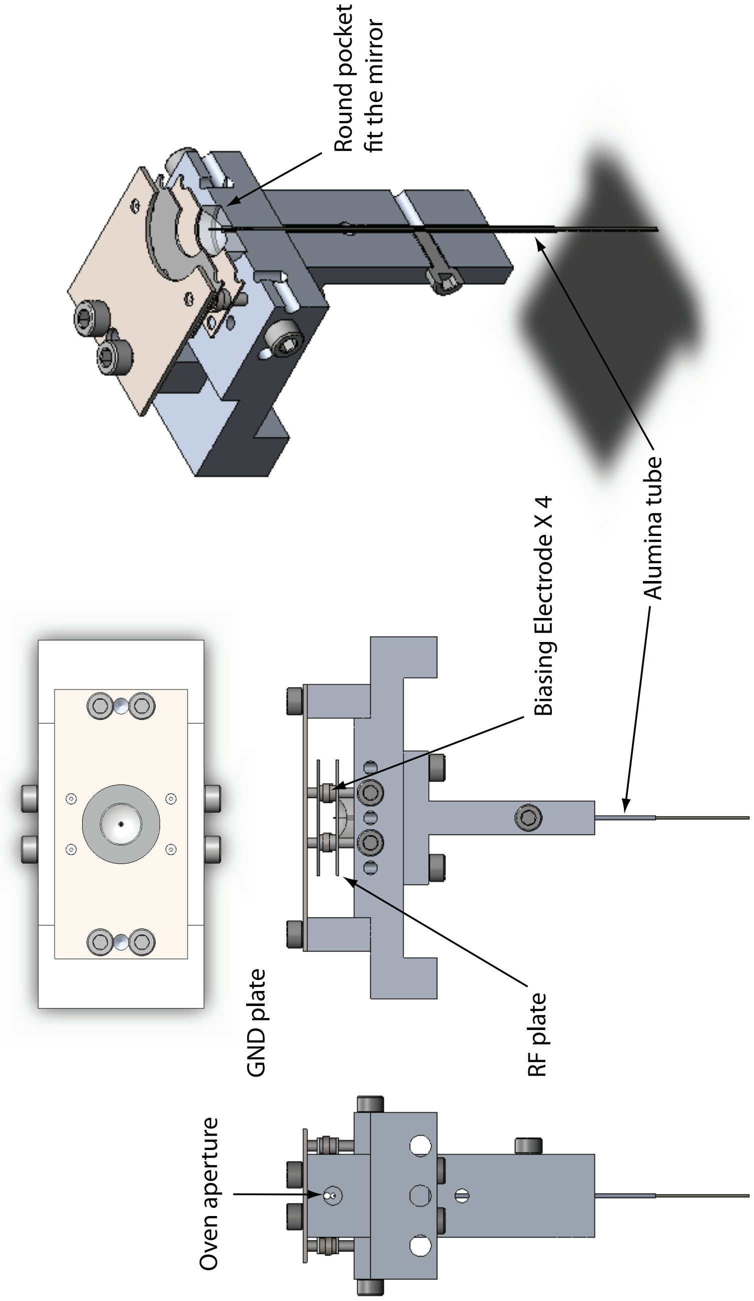

Figure 5.8: Construction of the ”tack” trap. The mirror is pressed by a stainless steel plate into the pocket on the aluminum frame. The RF signal is connected to the mirror surface via the plate. Four electrodes are around the mirror. Above them is the ground plate. Ions will be trapped between these two plates, near the needle tip.

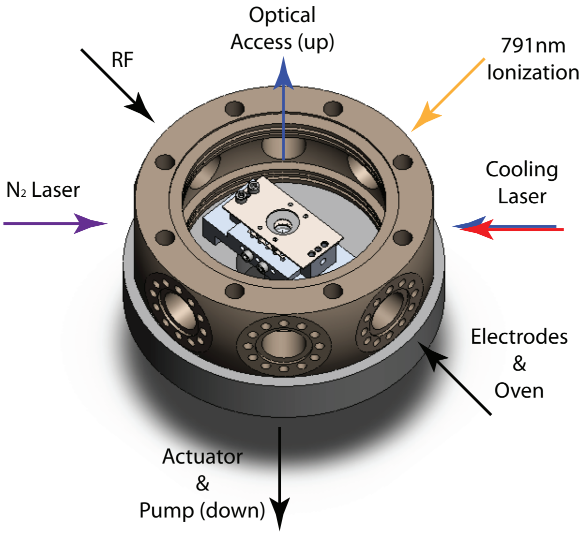

Figure 5.9: Port assignment of the trap chamber: The narrow band 791 nm ionization laser is perpendicular to the barium oven axis. The cooling lasers are tilted by 4° off the plane to cool the ion motion along the optical axis.

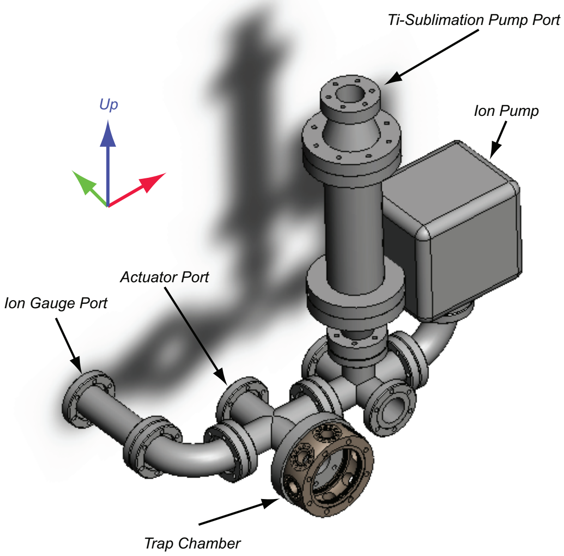

Figure 5.10: The overview of the "tack" trap vacuum system.

chamber is mounted vertically. It sits on a 4 way-cross between the pumps and an ion gauge, which gives us a more accurate pressure reading and better pumping. The most challenging part of vacuum system assembly is to attach the trap chamber to the system. The actuator with the needle mounted on the top is already in place and the chamber weighing more than 7 lb has to be installed with the needle going through the thin alumina tube. Multiple needles have been bent or destroyed before eventual success.

Barium is highly active in air, so we have to load it in an inert gas. The oven is modularized and attached to the chamber via a groove grabber. The new trap's structure allows a much smaller room for oven installation and we have to load the oven before it is fixed to the chamber. The alignment is also very critical, a few degrees of misalignment would result in failure to load ions (This did happened at the first attempt, and we had to open the vacuum and reinstalled the oven.). This sophisticated operation requires a longer time, and the original N_2 protection scheme we used to employ doesn't work well. Noticing that pure barium doesn't interact with CO_2, we usese it instead. The trap only needs to sit in a tank instead of a sealed chamber because the CO_2 is so heavy that it can displace the air and retain in the tank . This gives us huge convenience for hand operation. A CO_2 bath can be easily generated by putting dry ice on the tank floor. In less than a minute, it displaces the air completely. CO_2 gives us enough time (more than half an hour, limited only by the amount of dry ice) to load the oven module, install it in the trap chamber and carefully align it.

After oven installation, the vacuum system is sealed and pumped down with a turbomolecular pump, during which we run the oven at ∼2 A for about 30 minutes to bake out the possible barium oxide and other dirt. The whole trap is then heated up to $\sim 195°C$ and baked out for two weeks, during which a 225 l/s ion pump lowers the pressure from 10^{-5} torr to 10^{-7} torr. During the bake out, the turbo pump is frequently turned on to pump gases such as H_2 out of the system. The pressure saturates at around 1×10^{-7} torr at $195°C$. Considering the complex structure and the distance between the gauge and the pump, this pressure is reasonable. After the bake out, the Ti-sublimation pump is run for a few times to get rid of the water on its own filaments. We run the oven hot again before we close the valve to the big ion pump and separate the vacuum system from external pump.

The small, 20 l/s ion pump is then turned on to further pump down the closed system. In the following weeks, the Ti-sublimation pump is frequently run, and the system pressure goes down to about 10^{-10} torr.

5.3 Electrostatic Field Simulations

To predict the ions position in the trap, we use FreeFem++ software package to simulate the static electric field created by the trap. The program is a 2-d differential equation solver, so we start with the Poisson equation in cylindrical coordinates and reduce it into a 2-d problem. The variational form of the Poisson equation is:

$$\int_{\partial S} \frac{\partial v}{\partial x}\frac{\partial u}{\partial x} + \frac{\partial v}{\partial y}\frac{\partial u}{\partial y} - \frac{v}{x}\frac{\partial u}{\partial x} dxdy = 0 \tag{5.1}$$

where $u(x, y)$ is the potential field to solve and $v(x, y)$ is an arbitrary function differentiable to second order. The boundary conditions are set according to the electrodes' connection. The top, bottom and left boundaries of the calculation zone are set to ground and the right boundary is free. An example of the resulting field is shown in Fig. 5.11:

The result, after symmetrization about the right boundary, can be numerically fit into a quadratic function.

$$u(r, y) = 0.12r^2 - 0.22y^2 + 7.9\times10^{-16}ry - 3.9\times10^{-17}r + 5.4\times10^{-3}y + 1.4\times10^{-4}(V/mm) \tag{5.2}$$

Except for the first two terms, others are much smaller, and are ignored in the following calculations. The field shows a weak trap along the radial direction and a stronger, asymmetric trap along the axial direction as shown in Fig. 5.12. The trapping depth of the ponderomotive pseudopotential can be evaluated as:

$$U = \frac{QV^2}{4Md^2\Omega^2}, \tag{5.3}$$

where Q and M are the charge and mass of the particle, V is the RF field's voltage amplitude on the mirror, Ω is the RF frequency and d is a geometric parameter, here corresponding to the reciprocal of the square root of the quadratic coefficients. A 20 MHz, 400 V RF signal on the electrode corresponds to a trapping depth of 0.2 eV, which is about an order of magnitude higher than the thermal energy at room temperature ($\sim 0.01\ eV$). In the

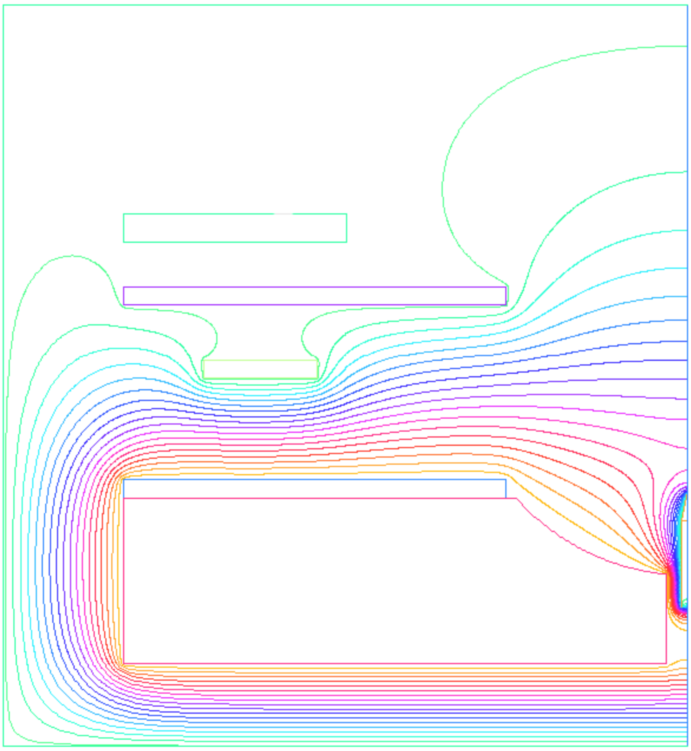

Figure 5.11: Field contour of the "tack" trap.

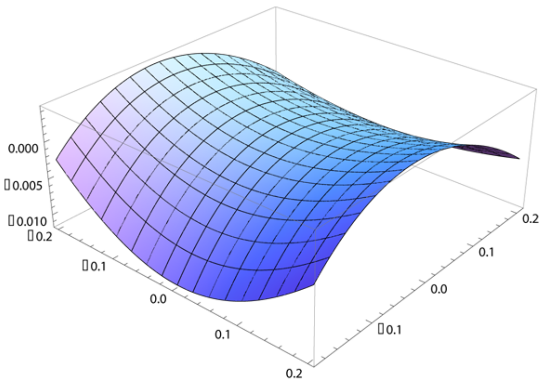

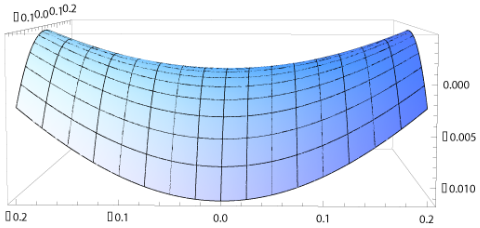

Field along the radial direction

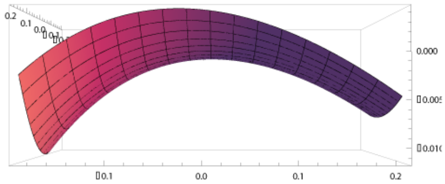

Field along the axial direction

Figure 5.12: Numerical fit of the ”tack” trap’s saddle-shaped field: the field along the radial direction is symmetric and weaker than that along the axial direction. The field along axial direction is asymmetric. It is steeper on the side near the needle.

experiment, when connected to a helical resonator, the RF resonates at 23 MHz with a Q factor of a few hundred. The maximum input RF power is ~6 to 8 W, which corresponds to about 400 V on the trap.

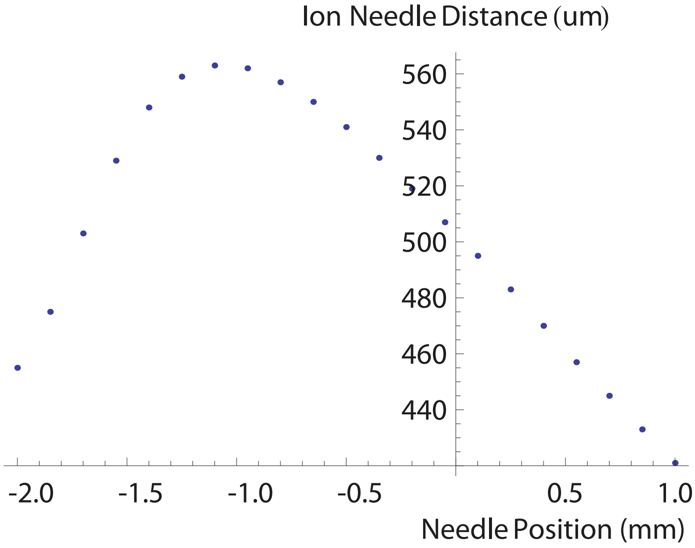

Figure 5.13: Simulated ion-needle distance at different needle positions

A very important structure of this new trap is its movable needle. We hope that the ion will follow the needle tip position to sit at desire place for imaging. To estimate the distance between the ion and tip, we calculated the trapping positions for different needle positions. Fig. 5.13 shows that in a large range, the ion is about half mm away from the needle tip.

5.4 Trap Performance

After two weeks of trying, it traps at last. The ions are found 0.5461 mm away from the needle tip. The measured secular frequency is 0.37 MHz in the radial direction and 0.6 MHz along the axial direction with ~ 3 W of RF at 23 MHz. Large ion crystals (Fig. 5.15) can be loaded with high barium oven temperature. The radial direction is almost degenerate, so when the crystal is rotationally symmetric, the ions tend to rotate. When the degeneracy is broken, the ion images are sharp. Single ions can be loaded with lower oven current

(∼1.32 A) and ionization UV laser repetition rate (∼0.5 Hz). When moving the actuator, the trapped ion(s) can follow the needle. The distance between the tip and the ion is almost a constant, as can be seen in Fig. 5.14.

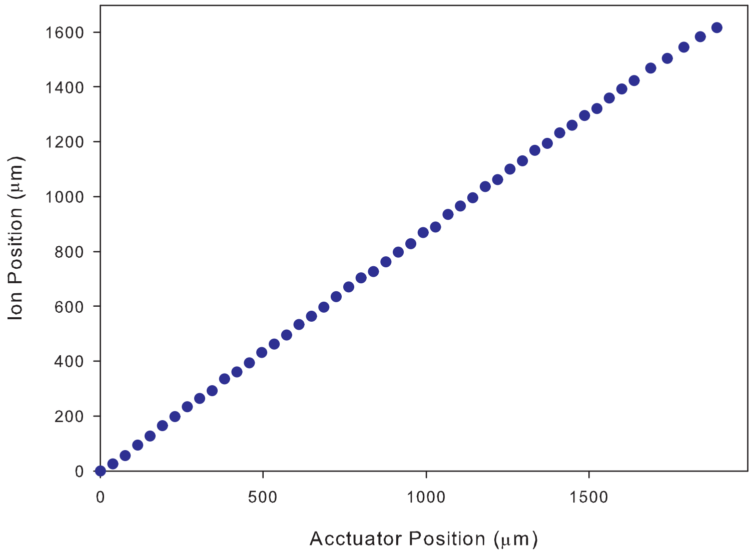

Figure 5.14: Measured trapping positions at different needle positions.

5.5 *Correction Optics Design*

The ”tack” trap’s small mirror gives us a chance to see both the image and the spherical aberration on the camera. The paraxial portion of the mirror forms a decent image which can resolve ions ∼ 10 *μm* apart (Figs. 5.15 and 5.16). But beyond that, the spherical aberration is huge, which is seen as large rings in Fig. 5.16. By adding up photon counts on each pixel of the camera, the intensity distribution can be estimated. The full aberated image has a count of ∼ 30000, while the central bright spot has a count of only about 4000.

To fully utilize the mirror surface and generate diffraction-limited image, we need an aspherical element. The ”tack” trap’s smaller configuration requires different correcting scheme than in the first trap. Its 4 mm focal length leaves no room for a Schmidt-like correction plate as we did before. If the ion is located at the focal point of the mirror, the

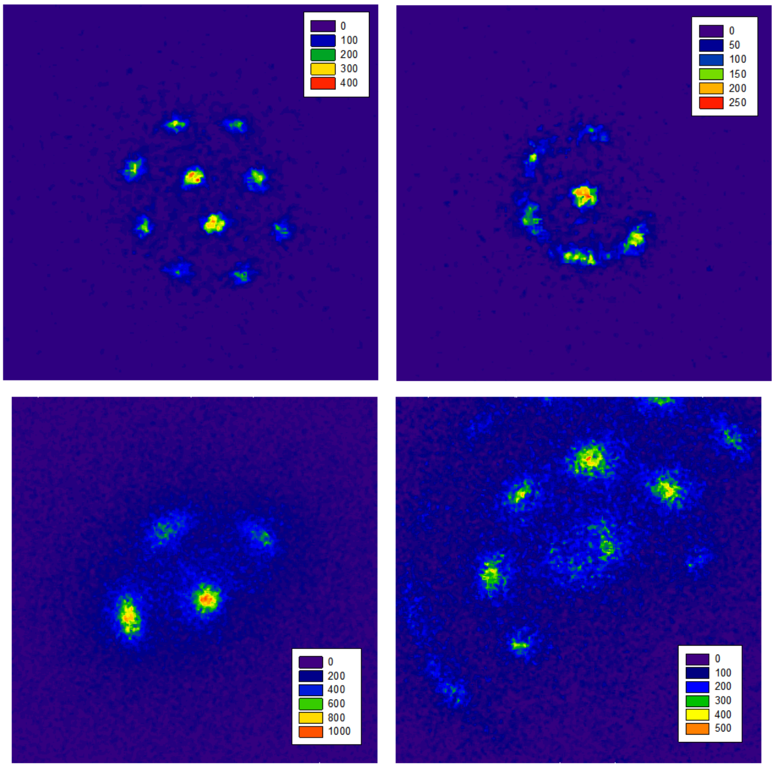

Figure 5.15: Images of ion crystals: Top ones are taken with the microscope and bottom ones are taken with the mirror.

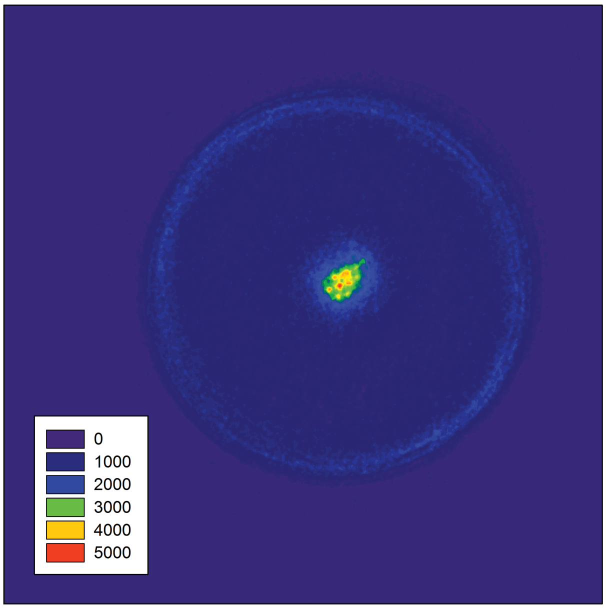

Figure 5.16: A picture showing large spherical aberration formed by the ”tack” trap mirror: The central bright spots are resolved individual ion images formed by the paraxial portion of the mirror and they only contain about one-seventh of the overall counts. The bright region within the ring is formed by the mirror’s marginal portion.

rays intersect with each other before any possible correction. One way to avoid this is to put the ion further away from the focal point, so that an intermediate image is formed first, and then an aspherical piece is used to collimate the ion's image (Fig. 5.17).

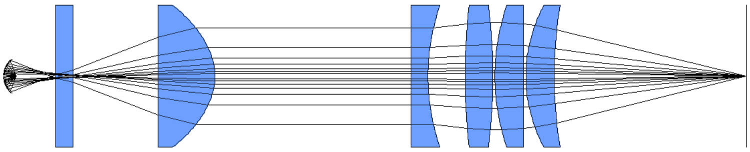

Figure 5.17: Corrector setup for the "tack" trap. The mirror of the "tack" trap is too small to apply any collimation corrector. Instead, the ion will be place at a position further than the focal point and is imaged first by the spherical mirror. The light from the ion image is then collimated with an aspherical piece, which also compensates the huge spherical aberration.

Normal aspherical lens shapes are calculated for a point source with no spherical aberration, while for the ion image by the spherical mirror with such a high NA, the aberration is huge, and it must be compensated with customized optics. We can use the same segment-fitting method as before to calculate the shape. Practically, we used the Eigonal method [76] to derived the shape. We only need a small modification to realize this on the base of the former program. When tracing each rays recursively, we use a variable to store the optical path during the current propagation and add to the former value. Then each run of the ray tracing will give us all the former information plus the optical path. By ordering the optical paths of different rays to be equal to the one along the main optical axis, the coordinates of those points on the corrector surface can be solved. Once a large number of points are calculated and joined, they form a smooth line with deviation less than the optical wavelength. Fig. 5.18 shows the simulated performance of the corrector and its dependence on various misalignments.

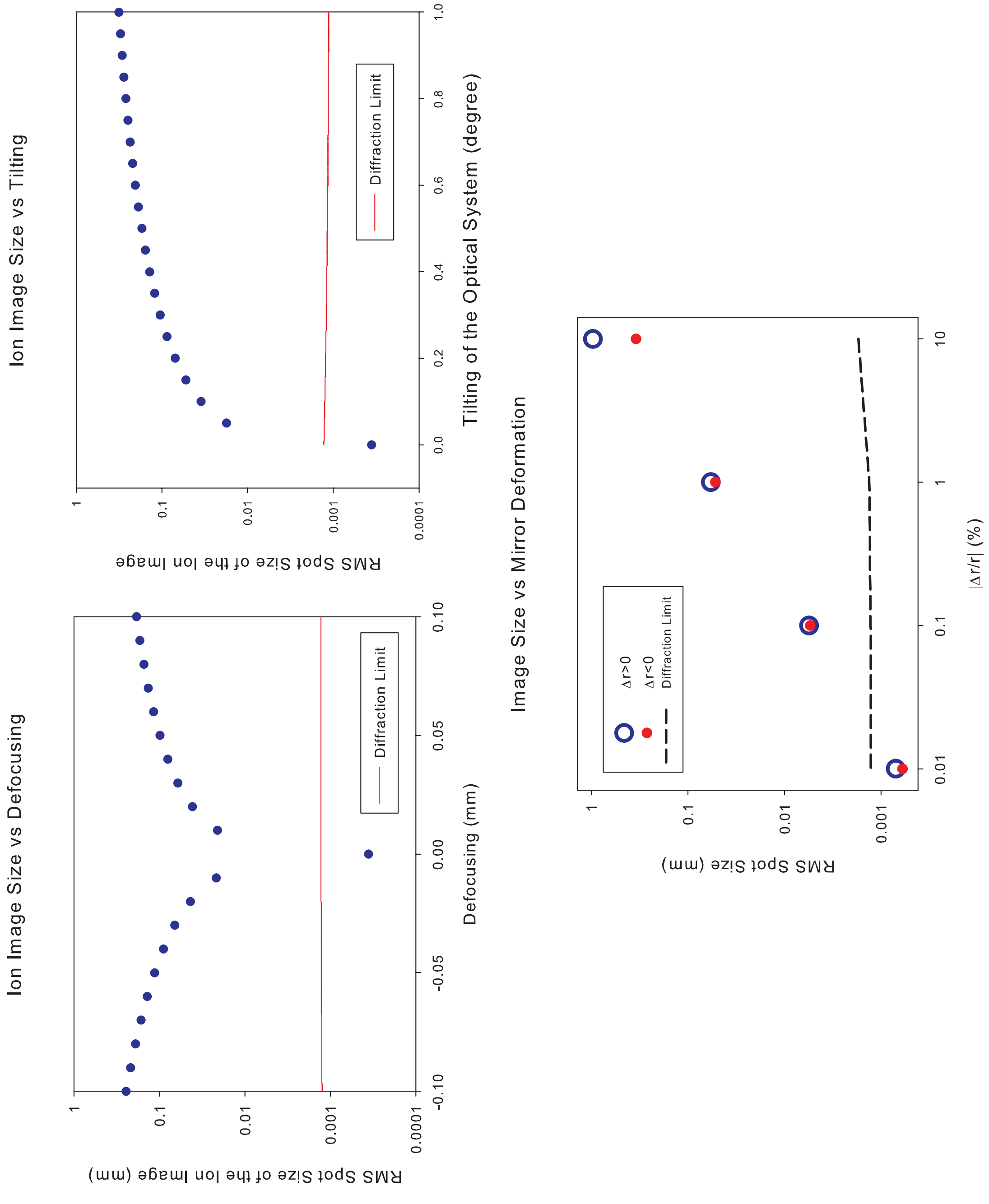

Figure 5.18: The ”tack” trap’s optical tolerance to defocusing, tilting and mirror deformation.

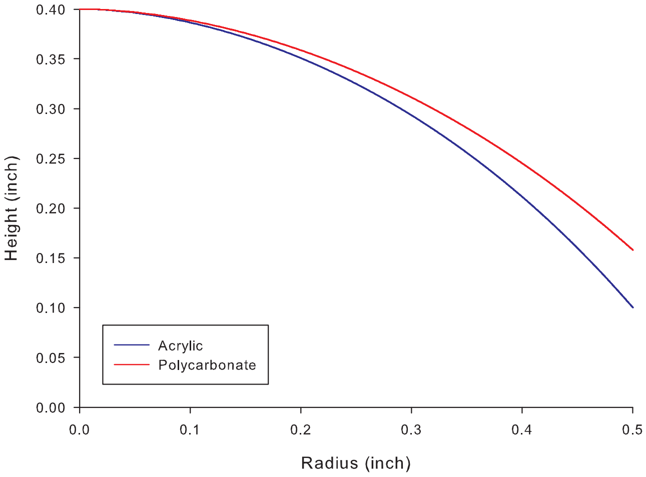

Figure 5.19: The lens shape calculations are carried out for two different materials, acrylic and polycarbonate.

5.6 Preliminary Results

To test the aspherical lens, we make a few prototypes out of the two materials: acrylic and polycarbonate. Acrylic is soft and has a higher water absorption rate. It is very easy to polish and scratch. Polycarbonate is ideal for plastic optics but the polishing is challenging. Since the two materials have different retraction indexes, two corrector shapes are derived, shown in Fig. 5.19. With our prior experience, the polishing procedure is improved by omitting the sandpaper pre-polishing to avoid scratching the surface of the flat side. Instead, we mix the 0.1 μm alumina powder with water and paste it on a fine fabric cloth stretched on a flat glass. The alumina powder in the cloth evenly contacts the flat surface and there is no sharp point to scratch it. The convex surfaces are polished on a lathe. The central part of the curved surfaces can not be polished well, but this is not a serious problem for us because there are almost no light rays through there. The finished correctors are shown in Fig. 5.20.

Fig. 5.21 shows the ion(s) image acquired with the optical setup in Fig. 5.17. The EMCCD camera is placed at the focal point of the micro-objective. Compared with the

Figure 5.20: Polished aspherical acrylic (vertical) and polycarbonate (horizontal) lenses.

images directly formed by the mirror (Fig. 5.16), the big ring disappeared and most of the light is concentrated in a very small area. The spot size is of order of 100 μm, much bigger than the diffraction limit. Considering that there are more than 4 different degrees of freedom(the ion's position, the corrector's position and tilting angles, and the distant between the micro objective and the camera) that haven't been optimized, this image is consistent with our simulation (Fig. 5.18), where very small deviations ($\sim$0.1 mm) will result in image spot size above 0.1 mm. One noticeable improvement from our last trap is that the coma of the image is not significant, which indicates the self aligning design is beneficial.

As our next step, we will add another magnification stage to get better image resolution. This will enable us to fine tune the optical setup to have a smaller spot size. Hopefully we can get close to the diffraction limit and couple a reasonable fraction of light into a single-mode optical fiber.

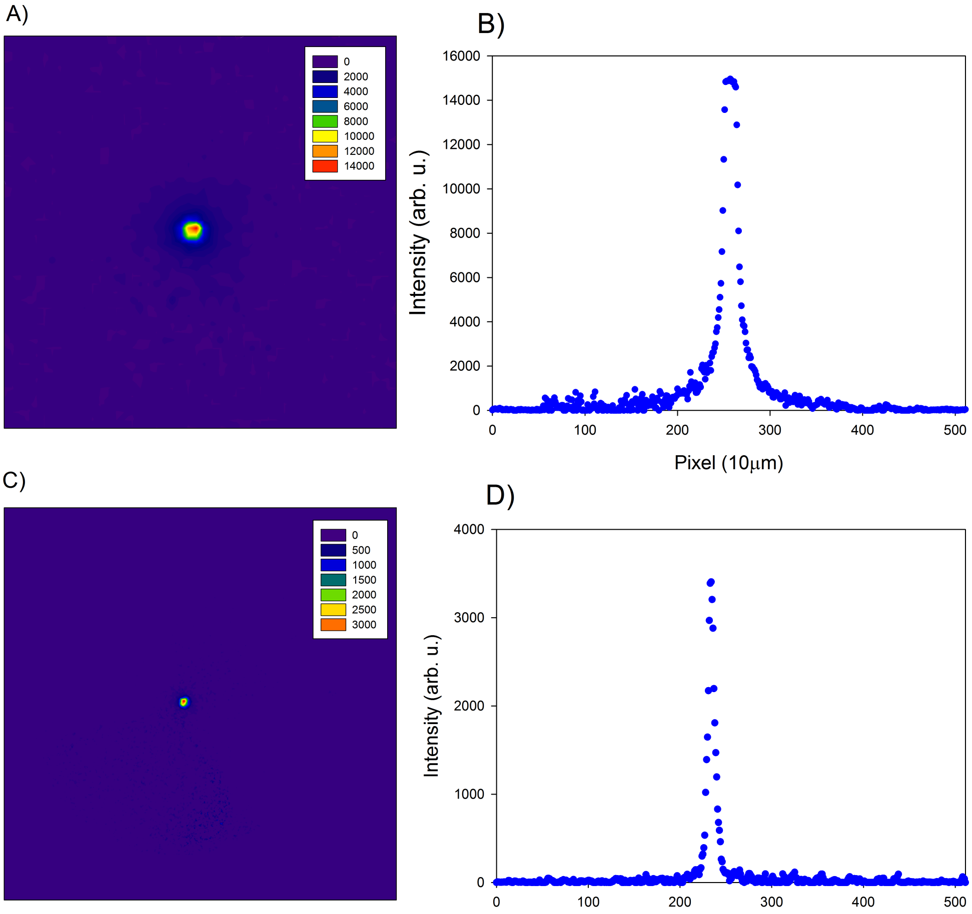

Figure 5.21: Contours and spot profiles of ion images formed with corrector. A and B: a bright ion crystal; C and D: a small number (possibly single) of ions. There is no obvious coma in both images. The large ring due to enormous spherical aberration is almost completely eliminated by the corrector.

Chapter 6

SCALING UP AND DOWN

In this chapter, we study the possibility of scaling down the size of the "tack" trap for scaling up the number of traps on a chip. From optics perspective, smaller devices are preferred because all the aberrations due to geometric factors are scaled down with the size, and the images approach the diffraction limit eventually. But if the trap is too small, the Johnson noise from the trapping electrodes will heat up the ions [57]. A reasonable size for micro trap is of the order of 10 to 100 μm. Current MEMS technology works very well at this scale, therefore such optical structures may be added on a micro-fabricated trap. I will first discuss a brute-force approach to minimizing the tack structure, and then a possibility to flatten it.

6.1 Fabrication of "Tack" Trap Components

One of the reason that we choose a spherical mirror instead of a parabolic mirror is its scalability. There are multiple ways to fabricate micron-scale spherical mirrors, whereas few technology exists for parabolas.

Spherical surfaces can be fabricated by anisotropic etching with KOH [77, 78]. Fig. 6.1 shows the outline of the procedure. The silicon layer is masked by a round SiO_2 mask of diameter D and etched by KOH. The etching stops at the four $< 111 >$ planes leaving a pyramid pit with depth of $D/\sqrt{2}$. Then the oxide is removed and the bare silicon continues to be etched by KOH. The pit will finally be etched out leaving a smooth curved surface of roughness 10 to 30 nm (or less than $\lambda/10$ for 493 nm light). The method has excellent surface quality and a maximum NA of about 0.2, which is a bit small.

Deep spherical surface can also be fabricated by isotropic etching. The process is illustrated in Fig. 6.2. The silicon substrate is first masked with a round SiO_2 hole and etched in $HNO_3 + HCl$ solution with agitation. The shape can be controlled by the etching time

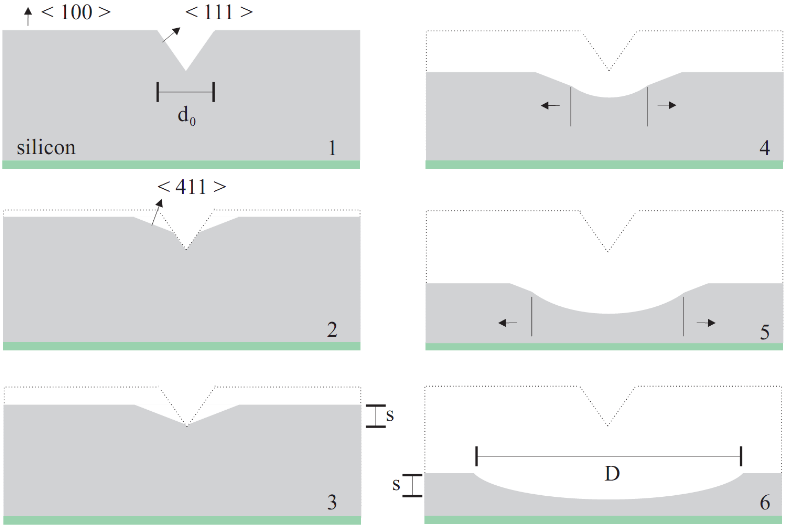

Figure 6.1: Curved mirror fabrication by KOH etching (The figure is from 6.2). First, a notch is etched with a round mask on the silicon substrate(not shown here), then the mask is removed and the silicon is further etched until the notch disappears and the surface becomes smooth.

and the concentration of the acid. The surface smoothness can be as good as 6 nm, and the NA may approach 1.

My personal favorite is the templated self-assembly electroplating method[79]. The difficulty of mirror fabrication is etching a curved surface out of a plane, because most etching methods are only good at precise 2D structure etching. The extra dimension means either the shape approximation or the need for extra masks and etching steps. Fig. 6.3 shows the concept of the templated self-assembly electroplating method. A silicone substrate is masked and a pocket is etched. The sidewalls of the pocket are coated with a thin layer of metal for electric connection. A spherical bead is added; it falls into the pocket due to the gravitational force. The base and bead are electroplated in an electrolyte bath. A spherical mirror forms in the space between the pocket and the mold. This method avoids concave etching by using a convex template. The latter is much easier to fabricate and polish. For example, small glass beads can be produced controllably by melting an optical fiber tip by high power laser. The shape and roughness of the electroplated surface totally depend on

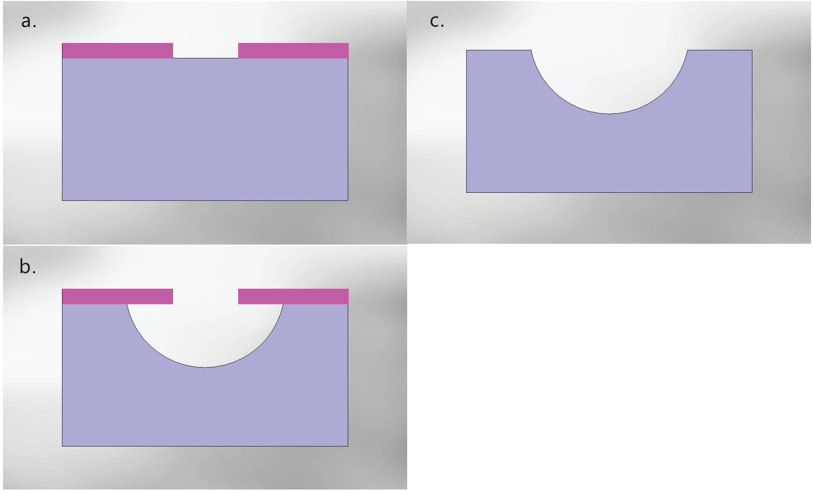

Figure 6.2: Curved mirror fabrication by $HNO_3 + HCl$ etching. First, the silicon substrate is masked with a round hole (a). Then the substrate is etched with $HNO_3 + HCL$ solution with agitation (b). The enchant attacks the substrate in all direction, leaving an almost spherical shape. Finally, the mask is removed when the etching is done.

that of the mold. If we use elliptical beads instead of the spherical ones, the solid angle can be easily made larger than 2π sr and the aberration on the other focal point can be completely eliminated with no additional optics. Sadly, parabolic molds seem unrealistic.

Micro-fabricating the needle is a different challenge. It can be fabricated, for example, with the method developed in [80] and illustrated in Fig. 6.4. With DRIE (Deep Reactive Ion Etching) process, high-aspect ratio pillars can be formed. To avoid a negative profile on a high-aspect ratio pillar, finer protection pillars are patterned around the main pillar to collimate the ion beam. An additional RIE (Reactive Ion Etching) process follows to sharpen the central pillar into a needle while the protecting thin pillars are etched away.

6.2 An Vision for a Micro-fabricated "Tack" Trap

Here I combine the technologies mentioned in previous section to form a micro fabricated trap design. The micro trap includes the following components: a spherical mirror with curvature radius of 200 μm and aperture radius of 150 μm; a needle through the mirror vertex reaching at half the mirror radius; four electrodes 100 μm above the mirror. It

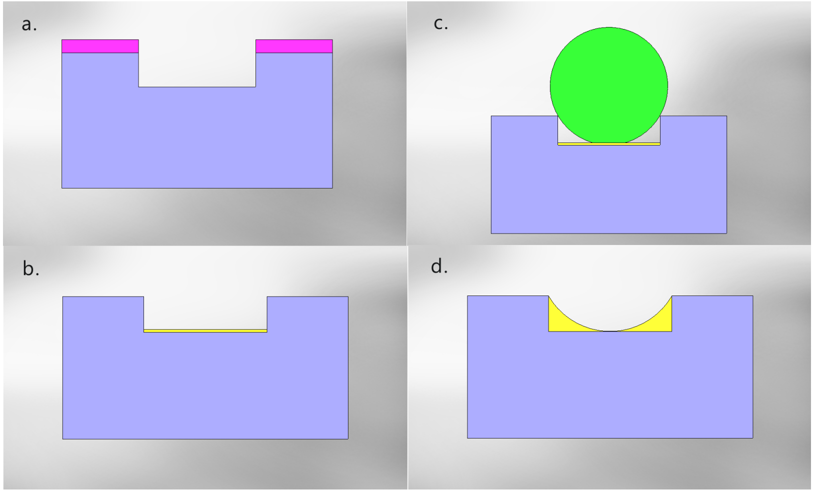

Figure 6.3: Micro spherical mirror fabrication by molding and electroplating. The silicon substrate is masked and dry etched to form a deep pocket with same diameter as the spherical mold (a). The mask is removed and the bottom of the pocket is coated with metal as electric path for plating (b). The spherical mold falls into the hole accomplishing the self-assembly (c). Metal accumulates between the ball and the substrate during the electroplating. The shape and smoothness of the metal surface is totally defined by that of the mold. After electroplating, the mold is removed (d).

is difficult to combine a sharp needle together with a smooth surface, therefore we would fabricate the needles and the mirrors separately, and assemble them afterwards. The binding procedure will not be prohibitively difficult because the sizes of the needles and the mirrors are around order of 0.1 mm, big enough for macro precision alignment equipment.

First we fabricate the needle plate with high aspect ratio etching. It starts with a 500 μm thick p-type conducting silicon. A 20 μm thick polyamide is deposited and patterned as the insulator between the metallic electrodes and the p-doped silicon substrate. A thin layer of metal is deposited and patterned. Another layer of polyamide is deposited to cover the metal traces. The needle will sit on a metal pad after etching. We then pattern the other side of the silicon with 12 μm thick positive photoresist, and follow with a two-hour DRIE process to form a pillar group leaving a thin layer of silicon. The needle is then formed by the RIE process and the thin silicon layer is etched off. The height of the needle should be less than 500 μm.

Then we use the self-assembly template electroplating method to fabricate the mirror. The procedure (Fig. 6.5) starts with a silicon substrate of 350 μm thickness. A thin layer (1 to 2 μm) of silicon oxide is deposited and patterned for RIE. The pattern includes a pocket structure (a 400×400 μm square), an aperture for needle (Ø40 μm) and access paths for electroplating. The RIE procedure will etch to the depth of 200 μm. We keep the oxide layer and evaporate on a thin layer (0.5 μm) of metal (Au or Pt). Then the metal layer is patterned to form 4 biasing electrodes. We immerse the finished structure into Au^+ ion electrolyte with optical-grade polished beads of 400 μm diameter. The beads will fall into the guides and form a template for electroplating. By finely controlling the electroplating current and time, a layer of 200 μm of metal is deposited in the gap between the bead and substrate. The whole process is finished with beads removed from the guide structure.

Once both pieces are ready, we can bind them together to form a mirror trap (Fig. 6.6). This mirror trap will offer us a fractional solid angle of ~ 0.4 (i.e.$\sim 1.6\pi$ sr). To reduce the Johnson noise, the trap should possibly be operated in low temperature. A 10 MHz to 20 MHz RF signal with amplitude of about 20 V (or higher, only limited by the breakdown voltage between the mirror surface and the needle) added between the mirror and the needle will generate a trapping field with similar depth ($\sim$0.1 eV) as the macro trap we have built

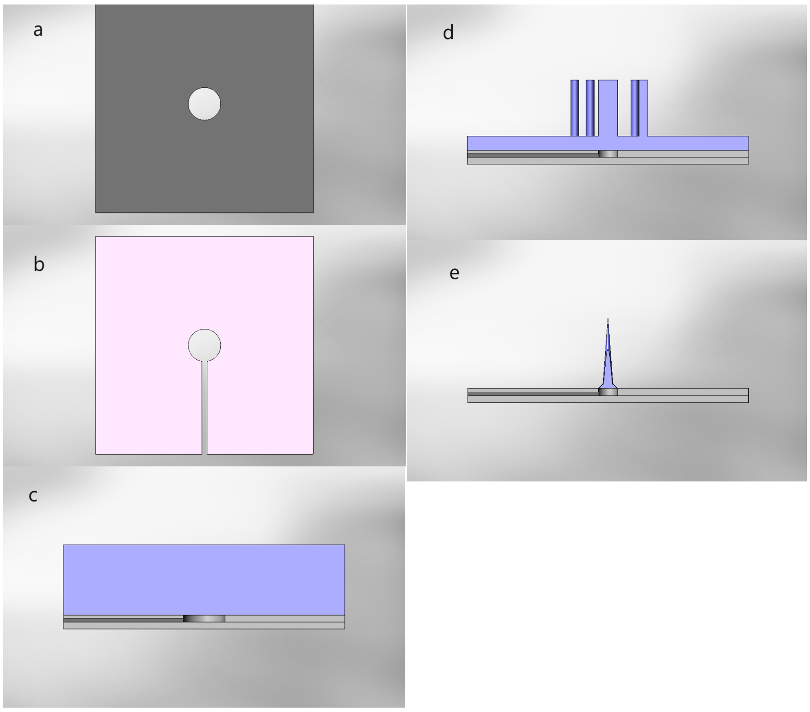

Figure 6.4: High aspect ratio needle etching. (a,b): patterns to form a metal electrode sandwiched by polyside. (c): cross section before DRIE procedure: a 500 μm doped silicon is combined with the electric plates; (d): cross section after DRIE: a thick beam is protected by several thin beams around; (e): further RIE to form the needle: the thin beams are etched away while the thick beam is etched into a tapered shape.

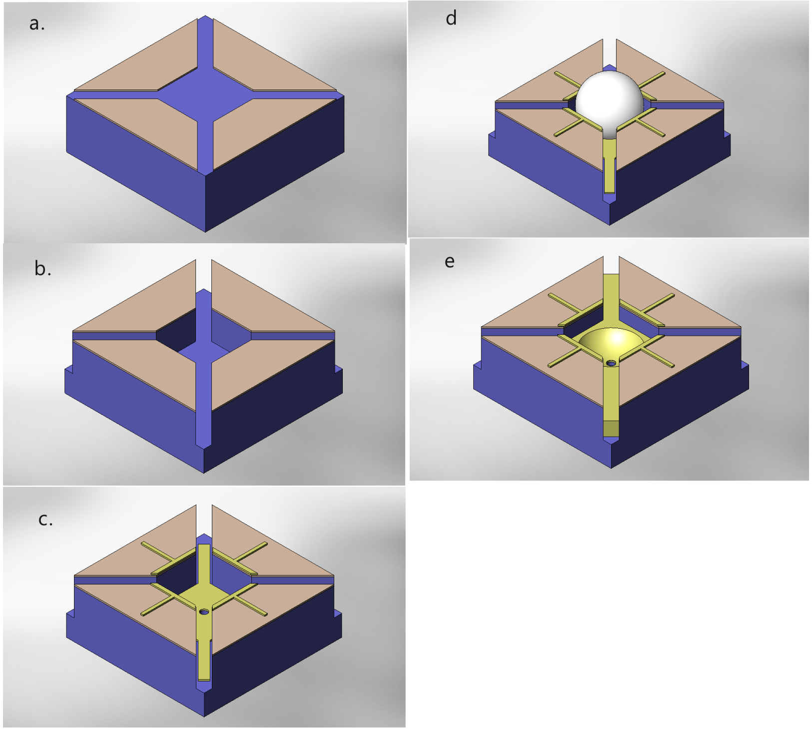

Figure 6.5: Fabrication of the micro ”tack” trap’s mirror electrode. (a): The oxide layer is deposited as both the RIE mask and the insulator layer. (b): RIE etches the silicon to form the mold guide, the needle aperture and optical access. (c): The electrodes are deposited and patterned. (d): The mode is added and the mirror surface is electroplated. (e): The mirror is finished with removing the mode.

and tested. The 4 electrodes on the isolation layer can be grounded to deepen the trapping potential and to shield the ion from the environment . The ion's position can be fine tuned by biasing the 4 electrodes' DC voltages.

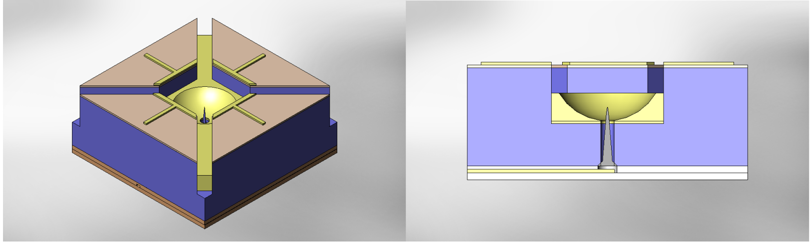

Figure 6.6: Final assembly of the micro fabricated mirror trap.

6.3 A Planar Design

If the mirror/needle structure can be flattened into a 2D surface, the fabrication procedure can be further simplified, and it would be easier to integrate the surface trap with the standard surface linear trap so that ions can be moved in and out of the mirror region if necessary. Conceptually this is not difficult, for it is similar to a Fresnel lens except for that it is mirror. Suppose the focal point is a distance d above the plane. Then a series of concentric rings focusing the collimated beam to the focal point is fabricated, as shown in Fig. 6.7(a). The shape of each ring is a small segment of parabola which can be expressed as:

$$x^2 = 4p(y + \frac{r^2}{4p}) \tag{6.1}$$

where $p = \frac{1}{2}(d + \sqrt{d^2 + 4r^2})$, d is the focal length and r is the distance from the mirror center to the inner edge of the ring. Each ring has to be etched (or deposited) with multiple steps to form small ($\ll \lambda$), discrete steps. Finally, the surface is coated with Au or Al to be reflective and conductive. Following the trap mutation logic in chapter 5, we can fit the trap electrodes on the same plane. The three electrodes from center to rim are ground, RF and ground (Fig. 6.7(b,c)). This can be done with lithography quite easily. A trap of this kind can give us nearly 2π sr solid angle.

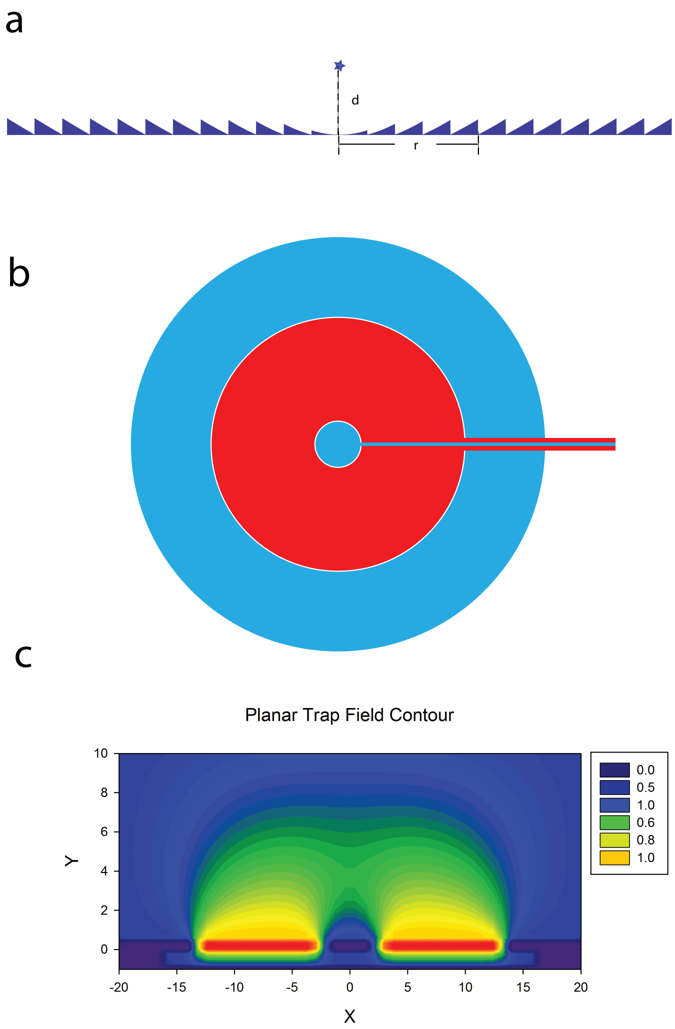

Figure 6.7: A planar trap with a Fresnel mirror (a). The electrode pattern for a circular planar trap (b), and its field contour (c). The red represents RF and the blue represent ground. Ions can be transfered through the linear planar trap to the center.

Conclusion

Fluorescence detection is a major channel to probe atomic systems. However, the efficiency of this process has not been quite so important until the advent of trapped ion and atom quantum computing, especially for probabilistic entanglement scheme for single trapped ions. The latter is a beautiful tool to transfer quantum information between massive particles and flying photons. Long distance entanglement of massive particles has never been so "easy". We built two different traps to address this issue. The feasibility of our approach has been well proven by both traps. With the first trap's experience, practical factors were considered in the development of our second trap. Once the single-mode fiber coupling is achieved, we will be poised to do the first loophole-free Bell inequality violation experiment.

Looking ahead, trapping ions strongly coupled with a high finesse optical cavity may be the ultimate solution for ion-photon interface. I believe it depends on a successful combination of traps and optics, in the same spirit in our "tack" trap design. It won't be too long before micro traps are integrated with light sources and detectors, which would eventually realize the practical quantum computation.

BIBLIOGRAPHY

[1] Richard P. Feynman. Simulating Physics with Computers. *International Journal of Theoretical Physics*, 21:467–488, 1982.

[2] David. Deutsch and Richard. Jozsa. Rapid solutions of problems by quantum computation. *Proceedings of the Royal Society of London A*, 439:553, 1992.

[3] R. Cleve, A. Ekert, C. Macchiavello, and M. Mosca. Quantum Algorithms Revisited. *Proceedings of the Royal Society of London A*, 454:339, 1998.

[4] P W. Shor. Algorithms for quantum computation: Discrete logarithm and factoring. *Proc. 35nd Annual Symposium on Foundations of Computer Science*, 1994.

[5] Ethan. Bernstein and Umesh. Vazirani. Quantum complexity theory. *SIAM Journal on Computing*, 26:1411, 1997.

[6] Richard P. Feynman. An Invitation to Enter a New Field of Physics. *Annual Meeting of the APS*, 1959.

[7] Michael A. Nielson and Isaac L. Chuang. *Quantum Computation and Quantum information.* Cambridge University Press, 2000.

[8] L K. Grover. A fast quantum mechanical algorithm for database search. *Proceedings, 28th Annual ACM Symposium on the Theory of Computing*, page 212, 1996.

[9] Seth. Lloyd. Universal Quantum Simulators. *Science, New Series*, 273:1073, 1996.

[10] Iulia. Buluta and Franco. Nori. Quantum Simulators. *Science*, 326:108, 2009.

[11] D P. DiVincenzo. Dogma and Heresy in Quantum Computing. *Quant. Inf. Proc.*, 1:1–6, 2001.

[12] J M. Martinis, S. Nam, J. Aumentado, and C. Urbina. Rabi oscillations in a large Josephson-junction qubit. *Phys. Rev. Lett.*, 89:117901, 2002.

[13] A. Steane. The ion trap quantum information processor. *Appl. Phys. B*, 64:623, 1997.

[14] D J. Wineland, C. Monroe, W M. Itano, D. Leibfried, B E. King, and D M. Meekhof. Experimental Issues in Coherent Quantum-State Manipulation of Trapped Atomic Ions. *Journal of Research of the National Institute of Standards and Technology*, 103:259, 1998.

[15] R. Blatt and D J. Wineland. Entangled States of Trapped Atomic Ions. *Nature*, 453:1008–1014, 2008.

[16] D. Loss and D. DiVincenzo. Quantum Computation with Quantum Dots. *Phys. Rev. A*, 57:120, 1998.

[17] Lieven M K. Vandersypen, Matthias. Steffen, Gregory. Breyta, Costantino S. Yannoni, Mark H. Sherwood, and Isaac L. Chuang. Experimental realization of Shor's quantum factoring algorithm using nuclear magnetic resonance. *Nature*, 414:883, 2001.

[18] Jeremy L. O'Brien. Optical Quantum Computing. *Science*, 318:1567, 2007.

[19] D. Leibfried, B. DeMarco, V. Meyer, D. Lucas, M. Barrett, J. Britton, W M. Itano, B. Jelenkovicacute, C. Langer, T. Rosenband, and D J. Wineland. Experimental demonstration of a robust, high-fidelity geometric two ion-qubit phase gate. *Nature*, 422:412, 2001.

[20] J J. Garcia-Ripoll, P. Zoller, and J I. Cirac. Speed Optimized Two-Qubit Gates with Laser Coherent Control Techniques for Ion Trap Quantum Computing. *Phys. Rev. Lett*, 91:157901–1, 2003.

[21] P. Maunz, S. Olmschenk, D. Hayes, D N. Matsukevich, L M. Duan, and C. Monroe. Heralded Quantum Gate Between Remote Quantum Memories. *Phys. Rev. Lett.*, 102:250502, 2009.

[22] L. Isenhower, E. Urban, X L. Zhang, A T. Gill, T. Henage, T A. Johnson, T G. Walker, and M.Saffman. Demonstration of a Neutral Atom Controlled-NOT Quantum Gate. *Phys. Rev. Lett.*, 104:010503, 2010.

[23] Peter T H. Fisk. Trapped-ion and trapped-atom microwave frequency standards. *Rep. Prog. Phys.*, 60:761, 1997.

[24] B B. Blinov, D. Leibfried, C. Monroe, and D J. Wineland. Quantum computing with trapped ion hyperfine qubits. *Quant. Inf. Proc.*, 3:45, 2004.

[25] R. Blatt and P. Zoller. Quantum Jump in Atomic Systems. *Eur. J. Phys.*, 9:250, 1988.

[26] J I. Cirac and P. Zoller. Quantum Computation with Cold Trapped Ions. *Phys. Rev. Lett.*, 74:4091–4094, 1995.

[27] Klaus. Molmer and Anders. Sorensen. Multiparticle Entanglement of Hot Trapped Ions. *Phys. Rev. Lett*, 82:1835, 1999.

[28] D. Kielpinski, C. Monroe, and D J. Wineland. Architecture for a large-scale ion-trap quantum computer. *Nature*, 417:709–711, 2002.

[29] D. Hucul, M. Yeo, S. Olmschenk, C. Monroe, W K. Hensinger, and J. Rabchuk. On the transport of atomic ions in linear and multidimensional ion trap arrays. *Quantum Information and Computation*, 8:0501, 2008.

[30] B B. Blinov, L. Deslauriers, P. Lee, M J. Madsen, R. Miller, and C. Monroe. Sympathetic Cooling of Trapped Cd^+ isotopes. *Phys. Rev. A*, 65:040304, 2001.

[31] J I. Cirac, P. Zoller, H J. Kimble, and H. Mabuchi. Quantum State Transfer and Entanglement Distribution among Distant Nodes in a Quantum Network. *Phys. Rev. Lett.*, 78:3221, 1997.

[32] Daniel. Gottesman and Isaac L. Chuang. Demonstrating the viability of universal quantum computation using teleportation and single-qubit operation. *Nature*, 402:392, 1999.

[33] L M. Duan, B B. Blinov, D L. Moehring, and C. Monroe. Scalable Trapped Ion Quantum Computation with a Probabilistic Ion-Photon Mapping. *Quantum Inf. Comput*, 4:165, 2004.

[34] L M. Duan, M J. Madsen, D L. Moehring, P. Maunz, R N. Kohn, and C. Monroe. Probabilistic quantum gates between remote atoms through interference of optical frequency qubits. *Phys. Rev. A*, 73:062324, 2006.

[35] D L. Moehring, M J. Madsen, K C. Younge, Jr. R N. Kohn, P. Maunz, L M. Duan, C. Monroe, and B B. Blinov. Quantum Networking with Photons and Trapped Atoms. *J. Opt. Soc. Am. B*, 24:300, 2007.

[36] Charles H. Bennett and Stephen J. Wiesner. Communication via one- and two-particle operators on Einstein-Podolsky-Rosen states. *Phys. Rev. Lett*, 69:2881, 1992.

[37] Charles H. Bennett, Gilles. Brassard, Claude. Crepeau, Richard. Jozsa, and Asher. Peres. Teleporting an unknown quantum state via dual classical and Einstein-Podolsky-Rosen channels. *Phys. Rev. Lett*, 70:1895, 1993.

[38] A. Einstein, B. Podolsky, and N. Rosen. Can Quantum-Mechanical Description of Physical Reality Be Considered Complete? *Physical Review*, 47:777, 1935.

[39] B B. Blinov, D L. Moehring, L M. Duan, and C. Monroe. Observation of entanglement between a single trapped atom and a single photon. *Nature*, 428:153, 2004.

[40] Bernard. Yurke, Samuel L. McCall, and John. R. Klauder. SU(2) and SU(1,1) interferometers. *Phys. Rev. A*, 33:4033, 1986.

[41] D L. Moehring, P. Maunz, S. Olmschenk, K C. Younge, D N. Matsukevich, L M. Duan, and C. Monroe. Entanglement of single-atom quantum bits at a distance. *Nature*, 449:68, 2007.

[42] Alain. Aspect. Bell's Inequality Test: More Ideal than Ever. *Nature*, 398:189, 1999.

[43] Gregor. Weihs, Thomas. Jennewein, Christoph. Simon, Harald. Weinfurter, and Aton. Zeilinger. Violation of Bell's Inequality under Strict Einstein Locality Conditions. *Phys. Rev. Lett.*, 81:5039, 1998.

[44] M A. Rowe, D. Kielpinski, V. Meyer, C A. Sackett, W M. Itano, C. Monroe, and D J. Wineland. Experimental violation of a Bell's inequality with efficient detection. *Nature*, 409:791, 2001.

[45] Christoph. Simon and William T M. Irvine. Robust long-distance entanglement and a loophole-free Bell test with ions and photons. *Phys. Rev. Lett.*, 91:110405, 2003.

[46] W. Paul and H. Steinwedel. Ein neues Massenspektrometer ohne Magnetfeld. *RZeitschrift fr Naturforschung A*, 8:448, 1953.

[47] D J. Berkeland, J D. Miller, J C. Bergquist, W M. Itano, and D J. Wineland. Minimization of ion micromotion in a Paul trap. *Journal of Applied Physics*, 83:5025, 1998.

[48] M R. Dietrich, A. Avril, R. Bowler, N. Kurz, J S. Salacka, G. Shu, and B B. Blinov. Barium Ions for Quantum Computation. *AIP Conf. Proc.*, 1114:25, 2008.

[49] W W. Macalpine and R O. Schildknecht. Coaxial Resonators with Helical Inner Conductor. *Proc of The IRE*, page 959, 1959.

[50] A V. Steele, L R. Churchill, P F. Griffin, and M S. Chapman. Photoionization and photoelectric loading of barium ion traps. *Phys. Rev. A*, 75:053404, 2007.

[51] Matthew. Dietrich. *Barium Ions for Quantum Computation.* PhD thesis, University of Washington, 2009.

[52] Karl D. Nelson, Xiao Li, and David S. Weiss. Imaging single atoms in a three-dimensional array. *Nature Physics*, 3:556–560, 2007.

[53] Y R P. Sortais, H. Marion, C. Tuchendler, A M. Lance, M. Lamare, P. Fournet, C. Armellin, R. Mercier, G. Messin, A. Browaeys, and P. Grangier. Diffraction-limited optics for single-atom manipulation. *Phys. Rev. A*, 75:013406, 2007.

[54] Waseem S. Bakr, Jonathon I. Gillen, Amy. Peng, Simon. Flling, and Markus. Greiner. A quantum gas microscope for detecting single atoms in a Hubbard-regime optical lattice. *Nature*, 462:74–77, 2009.

[55] M. Keller, B. Lange, K. Hayasaka, W. Lange, and H. Walther. Deterministic Coupling of Single Ions to an Optical Cavity. *Appl. Phys. B*, 76:125–128, 2003.

[56] M. Keller, B. Lange, K. Hayasaka, W. Lange, and H. Walther. Continuous generation of single photons with controlled waveform in an ion-trap cavity system. *Nature*, 431:7012, 2004.

[57] L. Deslauriers, S. Olmschenk, D. Stick, W K. Hensigner, J. Sterk, and C. Monroe. Scaling and Suppression of Anomalous Heating in Ion Traps. *Phys. Rev. Lett.*, 97:103007, 2006.

[58] M. Trupke, E E. Hinds, S. Eriksson, E A. Curtis, Z. Moktadir, E. Kukharenka, and M. Kraft. Microfabricated High nesse Optical Cavity with Open Access and Small Volume. *Appl. Phys. Lett*, 87:211106, 2005.

[59] Tatjana. Wilk, Simon C. Webster, Axel. Kuhn, and Gerhard. Rempe. Single-Atom Single-Photon Quantum Interface. *Science*, 317:488, 2007.

[60] H G. Barros, A. Stute, T E. Northup, C. Russo, P O. Schmidt, and R. Blatt. Deterministic single-photon source from a single ion. *New Journal of Phys*, 11:103004, 2009.

[61] G R. Guthohrlein, M. Keller, K. Hayasaka, W. Lange, and H. Walther. A single ion as a nanoscopic probe of an optical field. *Nature*, 414:49, 2001.

[62] K. Bergmann, R. Engelhardt, U. Hefter, and J. Witt. A detector for state resolved molecular beam experiments using optical fibres. *J. Phys. E: Sci. Instrum.*, 12:508, 1979.

[63] N. Lindlein, R. Maiwald, H. Konermann, M. Sondermann, U. Peschel, and G. Leuchs. A New 4π Geometry Optimized for Focusing on an Atom with a Dipole-Like Radiation Pattern. *Laser Physics*, 17:927–934, 2007.

[64] M. Sondermann, R. Maiwald, H. Konermann, N. Lindlein, U. Peschel, and G. Leuchs. Design of a mode converter for efficient light-atom coupling in free space. *Appl. Phys. B*, 89:489, 2007.

[65] Meng Khoon. Tey, Zilong. Chen, Syed Abdullah. Aljunid, Brenda. Chng, Florian. Huber, Gleb. Maslennikov, and Christian. Kurtsiefer. Strong interaction between light and a single trapped atom without the need for a cavity. *Nature Physics*, 4:924, 2008.

[66] Robert. Maiwald, Dietrich. Leibfried, Joe. Britton, James C. Bergquist, Gerd. Leuchs, and David J. Wineland. Stylus ion trap for enhanced access and sensing. *Nature Physics*, 5:551, 2009.

[67] B B. Blinov, R N. Kohn Jr., M J. Madsen, P. Maunz, D L. Moehring, and C. Monroe. Broadband laser cooling of trapped atomswith ultrafast pulses. *J. Opt. Soc. Am. B*, 23:1170, 2006.

[68] G. Shu, M R. Dietrich, N. Kurz, and B B. Blinov. Trapped ion imaging with a high numerical aperture spherical mirror. *J. Phys. B*, 42:154005, 2009.

[69] Refractive index database. *http://refractiveindex.info/*.

[70] N. Kurz, M R. Dietrich, G. Shu, R. Bowler, J. Salacka, V. Mirgon, and B B. Blinov. Measurement of the branching ratio in the $6P_{3/2}$ decay of Ba II with a single trapped ion. *Phys. Rev. A*, 77:060501(R), 2008.

[71] M. Almendros, J. Huwer, N. Piro, F. Rohde, C. Schuck, M. Hennrich, F. Dubin, and J. Eschner. Bandwidth-Tunable Single-Photon Source in an Ion-Trap Quantum Network. *Phys. Rev. Lett.*, 103:213601, 2009.

[72] N. Kurz. High Efficiency Single Photon generation from Trapped Barium Ions. In *Frontiers in Optics 2009/Laser Science XXV*, 2009.

[73] G. Shu, N. Kurz, M R. Dietrich, and B B. Blinov. Efficient fluorescence collection from trapped ions with an integrated spherical mirror. *Phys. Rev. A*, 81:042321, 2010.

[74] Rachel. Noek, Caleb. Knoernschild, Justin. Migacz, Taehyun. Kim, Peter. Maunz, True. Merrill, Harley. Hayden, C S. Pai, and Jungsang. Kim. Multi-scale Optics for Enhanced Light Collection from a Point Source. *arXiv:1006.2188v1*, 2010.

[75] C E. Pearson, D R. Leibrandt, W S. Bakr, W J. Mallard, K R. Brown, and I L. Chuang. Experimental Investigation of Planar Ion Traps. *Phys. Rev. A*, 73:032307, 2006.

[76] M. Born and E. Wolf. *Principles of Optics*. Cambridge University Press, 1997.

[77] D W. de Lima Monteiro, O. Akhzar-Mehr, P M. Sarro, and G. Vdovin. Single-mask microfabrication of aspherical optics using KOH anisotropic etchng of Si. *Optics Express*, 11:2244, 2003.

[78] G V. Vdovin, O. Akhzar-Mehr, P M. Sarro, D W. DeLimaMonteiro, and M. Lokteva. Arrays of spherical micromirrors and molded microlenses fabricated with bulk Si micromachining. *Proc. of SPIE*, 4945:11, 2003.

[79] S. Coyle, G V. Prakash, J J. Baumberg, M. Abdelsalem, and P N. Bartlett. Spherical micromirrors from templated self-assembly: Polarization rotation on the micron scale. *Applied Physics Letters*, 83:767, 2003.

[80] Y. Hanein, C G J. Schabmueller, G. Holman, P. Lucke, D D. Denton, and K F. Bohringer. High-aspect ratio submicrometer needles for intracellular applications. *J. Micromech. Microeng.*, 13:S91–S95, 2003.